Oxidation Communications 42, No 2, 121–131 (2019)

Heterogeneous catalytic systems

OBTAINING NANOSTRUCTURED CATALYST SYSTEMS AND STUDY OF CATALYTIC EFFICIENCY

A. GEORGIEVA*, K. PANAYOTOVA, ZH. IVANOV

Department of Chemical Engineering, 'Prof. Dr. Asen Zlatarov' University,
1 Prof. Yakimov Street, 8010 Burgas, Bulgaria
E-mail: *adrianaslavova@yahoo.com*; *krasi_panayotova@btu.bg*;
zh_ivanov@btu.bg

ABSTRACT

The combination of microemulsion approach to the synthesis of nanostructures with standard impregnation is a suitable alternative method for preparation of nanocatalysts. Nickel nanoparticles are quite significant for the catalysts and the conductivity of magnetic materials. Due to the large area and high activity of the $NiCO_3$ nanosized particles obtained, they can successfully be used to produce selective adsorbents and catalysts for various industrial processes. The aim of the present paper is obtaining of nanostructured catalyst systems. The catalytic activity of the composition $NiO/\gamma\text{-}Al_2O_3$ has been studied by oxidative dehydration of ethane to ethene.

Keywords: nanoparticles, nickel carbonate, W/O microemulsion system, nanocatalyst, oxidative dehydration.

AIMS AND BACKGROUND

Nanotechnology is another scientific and technological revolution the results of which can be seen in all fields of material production, technology and life. The structures in the nanometer range obey the laws of quantum physics which fundamentally changes their mechanical, optical and electrical properties. Thus, the nanoparticles became extremely important for microelectronics, medicine, ceramics, etc. (Fig. 1).

Due to their thermodynamic stability and comparatively non-complicated structure, the reverse microemulsion systems are increasingly used for industrial and domestic purposes. They can be used as model systems and they are very significant for the so called 'micellar catalysis'[1–9].

---

[*] For correspondence.

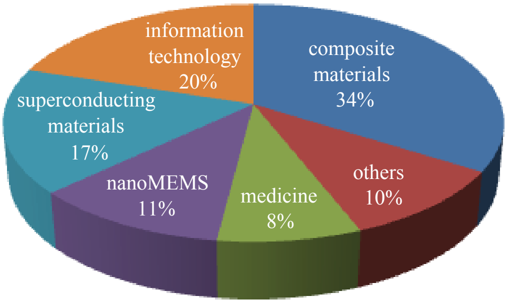

Fig. 1. Application aspects of nanosized particles and nanostructured materials

The review of the literature revealed that with the development of nanotechnology, the combining of the microemulsion method with standard impregnation is a suitable alternative method for preparation of nanocatalysts. On the other hand, it is well known for a number of processes that activity of the catalysts deposited onto inorganic substrate is by several orders higher than that of the analogous complex catalyst[10–16].

Nickel nanostructures are of great importance for the catalysts and the conductivity of the magnetic materials[17–21]. Due to the large area and high activity of the $NiCO_3$ nanosized particles obtained, they can successfully be used to produce selective adsorbents and catalysts for various industrial processes.

The present work addresses the micro-emulsion method for formation of nanoparticles. The microemulsions are thermodynamically stable and optically transparent systems, most often composed of three basic components: two immiscible liquids (commonly water and oil) and surfactant. These thermodynamically stable dispersions allow performing chemical reactions leading to syntheses of various inorganic and organic nanoparticles.

With regard to this, the aim of the present paper is obtaining of nanostructured catalyst systems and studies on the catalytic activity in a process of oxidative dehydration of ethane to obtain the end product – ethene.

EXPERIMENTAL

The experiments included the following main stages:

– Synthesis of nanosized $NiCO_3$ particles in reverse microemulsion system;

– Separation of the nanostructure from the liquid phase;

– Identification of the nanoparticles;

– Deposition of the nanoparticles onto substrates and thermal treatment to obtain partially nanostructured catalyst systems.

MICROEMULSIONS, REACTOR AND MODUS OPERANDI

The method for preparation of carbonate microstructures is based on the use of a single microemulsion system, namely the colloid dispersed system of W/O type: aqueous solution/*n*-hexane/Aerosol-OT ($NiSO_4.7H_2O/n\text{-}C_6H_{14}/C_{20}H_{37}NaO_7S$). The corresponding alkali suspension is inorganic phase while the organic phase is *n*-hexane, with the inorganic microdrops being dispersed in the organic substance. The substances composing the three-component reverse microemulsion system are comparatively low by price, easily available and easily separable. The microemulsion samples were prepared by mixing with n-hexane and 0.01 M solution of Aerosol-OT in a glass reactor followed by addition of the particular inorganic solution. The working volume of the W/O microemulsion prepared was 50 ml with the ratio organic to inorganic substances varying for the individual experiments. For all the experiments carried out, the reverse micelle solutions were obtained at ration of aqueous solution to surfactant (R = [aqueous solution]/[AOT]) = 20. The microemulsion system was stirred by magnetic stirrer for 60 min (t_1) at constant rotation speed of $n = 800\ \text{min}^{-1}$ and the experiments temperature was kept at $T = 25°\text{C}$. The scheme of the installation for preparation of carbonate nanostructures has been described earlier[22].

Since the W/O emulsion formed contained only one of the components (the inorganic solution), the second component was introduced into the reactor as gas (CO_2). The gas bubbled at constant flow rate in the device for 60 min (t_2). In this case, the nanostructures were obtained by carbonisation of the alkali suspension which resulted in chemical interaction between the gas and the inorganic solution. Thus, a chemical reaction occurred at pH = 10, the products of which are slightly soluble substances ($NiCO_3$). A diagram of the experimental method is illustrated in Fig. 2.

After each experiment for preparation of carbonate nanostructures, both the microemulsion phases were separated and they were analysed to prove the presence of the corresponding carbonate. The distribution of metal ions in the two phases was determined complexometrically. The shape, structure and size of the nanoparticles were determined on a transmission electron microscope.

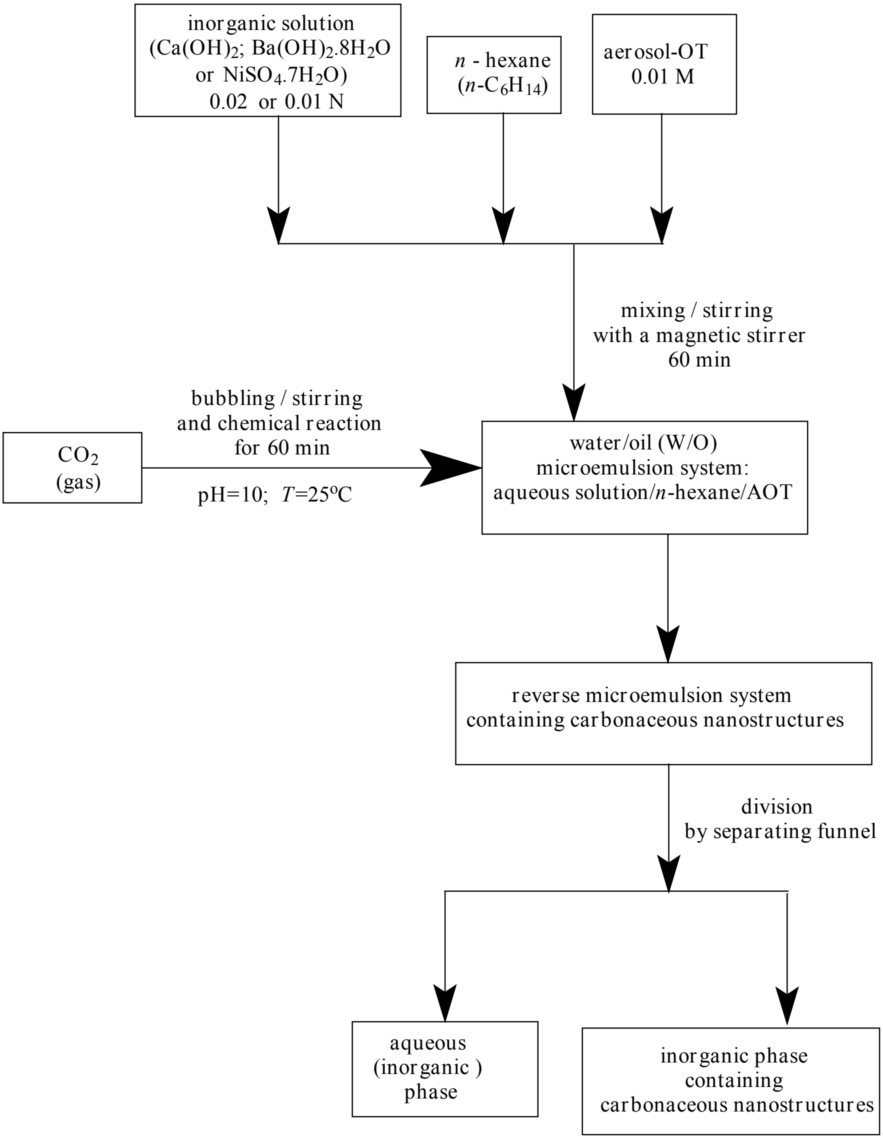

Fig. 2. Diagram of the technology for synthesis of carbonate nanostructures in reverse (W/O) microemulsion system

APPLYING THE $NiCO_3$ ULTRAFINE PARTICLES SYNTHESISED FOR PREPARATION OF PARTIALLY NANOSTRUCTURED CATALYST SYSTEMS

The next stage of the experimental work was the deposition, i.e. impregnation of the ultrafine particles obtained in a traditional porous substrate. The deposition of the $NiCO_3$ particles into a conventional porous carrier was performed with particles containing

TiO_2 (Degussa) and γ-Al_2O_3 (Sasol). The carrier characteristics are summarised in Table 1. Automated Gas Sorption System Quantachrome NOVA with precision of the relative pressure P/Po Toler 0.050/0.050 was used for characterisation of the carriers.

Table 1. Characteristics of catalyst carriers

Carrier	Particle size (mm)	Pore size (nm)	Pore volume (cc/g)	Specific area (m^2/g)
7 TiO_2	1.5	31.19	0.3690	47.31
γ-Al_2O_3	1.8	10.33	0.5071	196.4

Before the deposition process, the carriers were thermally treated to remove the residual moisture. The nanoparticles were layered by a standard impregnation procedure. The impregnation was chosen since the activity of the nanoparticles deposited onto inorganic carriers is by several orders higher than that of the complex catalysts.

A consequent calcination in an oven (up to 573 K) to attain full decomposition of $NiCO_3$ was performed to obtain a catalyst with a composition: NiO/TiO_2 and NiO/γ-Al_2O_3. The catalyst synthesised in this way allows applications to partial oxidation of low-molecular alkanes.

RESULTS AND DISCUSSION

Experiments performed provided nanosized $NiCO_3$ particles. They were identified by electron microscopy analysis (TEM) carried out at the Central Scientific Research Laboratory of University ‘Prof. D-r A. Zlatarov’ – Bourgas and the Laboratory of Transmission Electron Microscopy at the Institute of Metal Science, Equipment and Technologies ‘Acad. A. Balevski’ with Centre of Hydro and Aerodynamics at the Bulgarian Academy of Sciences.

The particle shape, structure and size were determined by transmission electron microscopy (TEM, ‘Opton’ EM-10 B (Germany)). The particles were almost spherical in shape, have a crystalline structure and a size varying from 10 to 20 nm (from 10×10^{-9} to 20×10^{-9} m). The latter allows assuming that the obtained powders are monodispersed in size. Sample TEM photographs are presented in Fig. 3 (*a*, *b*, *c*). Since the particles are fine enough and in large numbers, they give diffraction maxima in all directions. The electrograms (Figs 3*b* and *c*) reveal that the particles produced clear diffraction pattern due to well-formed crystalline structures.

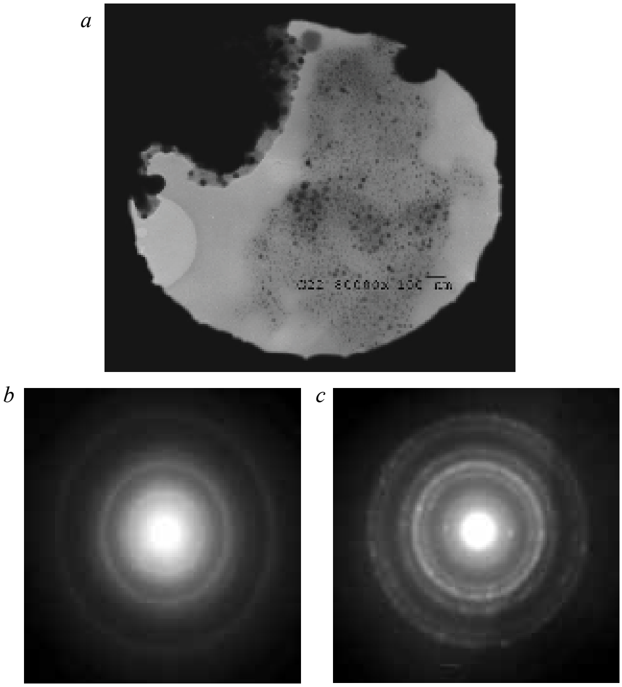

Fig. 3. TEM images of $NiCO_3$ nanostructures (d_{cp} = (10–20) × 10^{-9} m)
Microemulsion system: $NiSO_4.7H_2O/n\text{-}C_6H_{14}/C_{20}H_{37}NaO_7S$; synthesis conditions: $C = 1 \times 10^{-2}$ mol/l, $n = 800$ min^{-1}, $t_1 = 60$ min, $t_2 = 60$ min, $R = 20$, $T = 25$°C

The electron microscopy observations of the nanostructured catalysts (Fig. 4) were carried out in the Institute of Physical Chemistry of the BAS, Sofia, on a Scanning electron microscope (SEM, 'Tesla' BS-340 (Czech Republic)). Before the observations, the samples were contrasted with gold.

It can be seen from the images of different parts of the samples (1 and 2) that the pores of the substrate TiO_2 (31.19 × 10^{-9} m) (Fig. 4*a*) are completely filled by the deposited nanoparticles, unlike these of $\gamma\text{-}Al_2O_3$ (10.33 × 10^{-9} m) (Fig. 4*b*).

This fact confirms that the size (diameter) of the nanoparticles synthesised is between 10 and 20 nm. The photographs reveal that the thermal treatment does not provoke either the carrier shape or size (destruction); as well as sintering of the nanoparticles.

The NiO content in the nanocatalysts was determined by atomic absorption spectroscopy to be 8.9 × 10^{-4}% for sample 1 and 19.0 × 10^{-4}% for sample 2.

The catalyst systems obtained are aimed to intensify the partial oxidation of low molecular weight hydrocarbons.

The efficiency of the nanostructured NiO catalyst deposited onto $\gamma\text{-}Al_2O_3$ was studied in a process of oxidative dehydration of ethane to obtain the goal product – ethene. The process was carried out in the Otto-von-Guericke-Universität Magdeburg, Germany, in a metal reactor with fluidised bed (Fig. 5) and cross-section area of 1 × 10^{-2} m^2 at temperatures of 813 and 851 K.

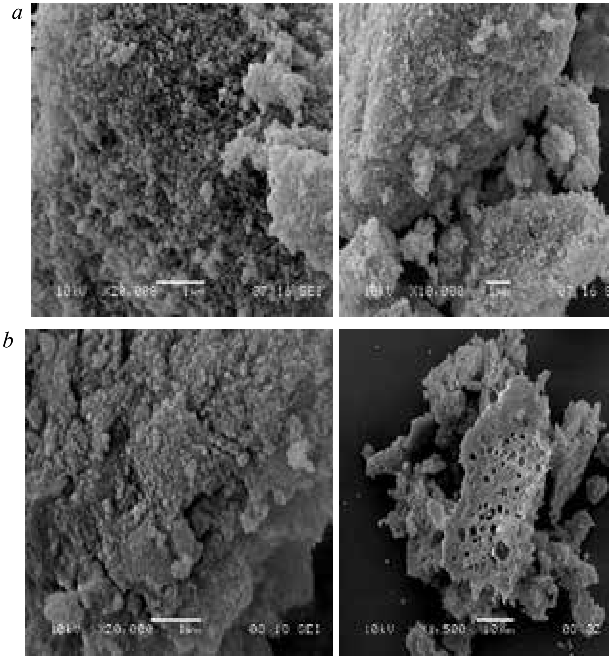

Fig. 4. SEM images of the catalyst systems with partial nanostructure obtained: sample 1 – NiO/TiO_2 – *a*; sample 2 – $NiO/\gamma\text{-}Al_2O_3$ – *b*

The mass of the catalyst layer of $NiO/\gamma\text{-}Al_2O_3$ in the reactor was 150 × 10^{-3} kg and the fluidising gas contained ethane and nitrogen. Oxygen was supplied under a gas-distribution grid through ceramic membranes.

The reagents ethane and oxygen were fed at ratio: C_2H_6/O_2 = 0.2; 0.5; 1.1; 1.5; 2.0. The stoichiometric ratio of the reagents was 2. The temperature in the catalyst layer was monitored by a thermocouple mounted in the layer. The composition of the initial gas was controlled by the gas-chromatograph which was part of the system.

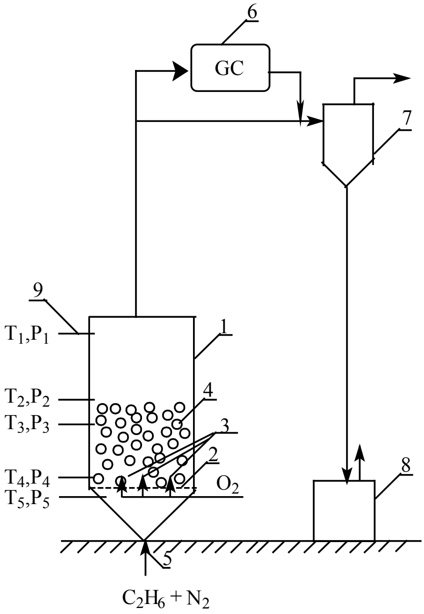

Fig. 5. Scheme of installation for the process of oxidative dehydration of ethane in presence of nanostructured catalyst NiO/γ-Al_2O_3
1 – reactor with steady layer; 2 – gas-distributing grating; 3 – membranes for oxygen supply; 4 – NiO/γ-Al_2O_3 catalyst; 5 – ethane and air supply; 6 – gas chromatograph; 7 – cyclone; 8 – gas-collecting vessel; 9 – indicator for temperature and pressure

The experimental studies on the process of oxidative dehydration of ethane in presence of the ‘nanocatalyst’ were carried out under reaction conditions shown in Table 2 and ratio ethane/oxygen in the range of 0.2–2.0.

The results obtained from the experiments performed at temperature 851 K in the presence of the nanocatalyst system (NiO/γ-Al_2O_3) were compared to these for the same catalysed process realised earlier in presence of catalyst VOx/γ-Al_2O_3.

The yield and the selectivity to ethene in the catalytic process carried out at temperature of 851 K were calculated.

Table 2. Experimental parameters of the process of oxidative dehydration of ethane in presence of nanostructured catalyst

No	Temperature (°C)	Pressure (Pa)	Concentration of C_2H_6 (vol%)	C_2H_6/O_2*
1	815	126.25	1.22	0.24
2	816	122.50	1.37	0.27
3	817	96.25	1.37	0.27
4	813	107.50	1.23	0.53
5	813	103.75	1.23	0.53
6	811	100.00	1.00	1.14
7	811	97.50	1.00	1.14
8	811	101.25	1.00	1.78
9	811	110.00	1.00	1.78
10	851	120.00	1.00	2.29
11	850	98.75	1.00	2.29
12	850	101.25	1.00	1.78
13	849	106.25	1.00	1.78
14	850	126.25	1.00	1.14
15	849	96.25	1.00	1.14
16	853	71.25	1.23	0.53
17	853	103.75	1.23	0.53
18	857	120.00	1.37	0.27
19	857	110.00	1.37	0.27

* Molar ratio.

Figure 6 shows the yields of ethene, CO_2 and CO observed by the experiment carried out at 873 K. The catalyst selectivity increases with increase in C_2H_6/O_2 the ratio and exhibits high selectivity at stoichiometric ratio of the reagents about $C_2H_6/O_2 = 2$ (Fig. 7).

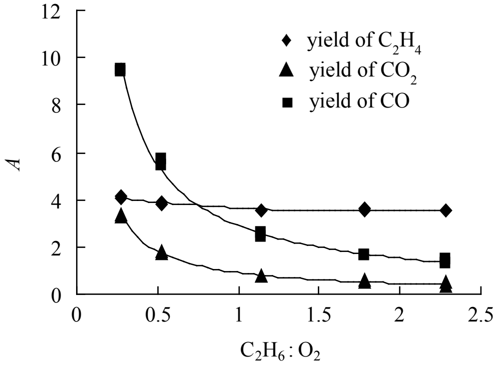

Fig. 6. Dependence of the yields of C_2H_4, CO and CO_2 on the ratio C_2H_6/O_2 for NiO/γ-Al_2O_3 nanocatalyst

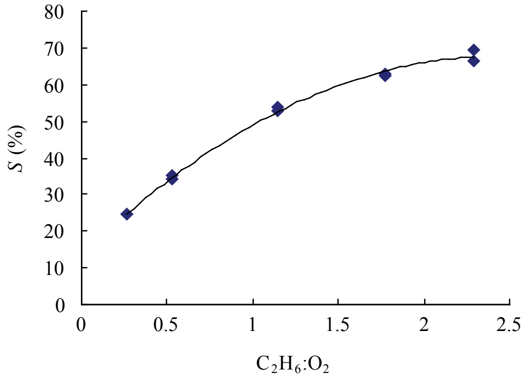

Fig. 7. Dependence of the selectivity of C_2H_4 on the ratio of C_2H_6/O_2 for the NiO/γ-Al_2O_3 nanocatalyst

CONCLUSIONS

As a result of the studies carried out and the results obtained, the following conclusions can be made:

1. As a result of the experiments carried out, solid nanosized nickel carbonate particles were synthesised. The studies of the nanoparticles proved that:

1.1. The carbonate nanostructures were obtained by chemical reaction under microemulsion conditions at various mass ratios of the phases forming the reverse microemulsion system.

1.2. The presence of the corresponding bonded carbonate ions was established by qualitative analysis of each phase of the microemulsion water/oil used.

2. The nanoparticles obtained were identified and characterised using the methods of electron microscopy (SEM, TEM). Their spherical shape, crystalline structure and narrow distribution of the particles by size (mono dispersity) were proved. The ultrafine particles of $NiCO_3$ were approximately of the same diameter (size) which varied in the narrow interval from 10×10^{-9} to 20×10^{-9} m.

3. A technology for preparation of partially nanostructured catalyst systems was realised by which the ultrafine $NiCO_3$ particles were successfully used to obtain 'nanocatalysts' with composition: NiO/TiO_2 and NiO/γ-Al_2O_3.

3.1. The catalytic efficiency of the nanocatalyst system NiO/γ-Al_2O_3 was studied in the process of oxidative dehydration of ethane to obtain the goal product – ethene in a fluidised bed reactor.

3.2. The yield and selectivity to ethene were calculated for the catalysed process carried out at temperature of 851 K. At stoichiometric ratio of the reagents $C_2H_6/O_2 = 2$, high value of the selectivity of the partially nanostructured catalyst with composition NiO/γ-Al_2O_3 was observed.

REFERENCES

1. M. A. LOPEZ – QUINTELA, J. RIVAS: Chemical Reaction in Microemulsions: a Powerfull Method to Obtain Ultrafine Particles. J Colloid In, **158** (2), 446 (1993).
2. J. SJÖBLOM, R. LINDBERG, S. E. FRIBERG: Microemulsions – Phase Equilibria Characterization, Structures, Applications and Chemical Reactions. Adv Colloid Interfac, **65**, 125 (1996).
3. B. K PAUL, S. P. MOULIK: Microemulsions: An Overview. J Disper Sci Technol, **18** (4), 301 (1997).
4. K. P. BIDYUT, S. P. MOULIK: Uses and Application of Microemulsions. Curr Sci, **80** (8), 990 (2001).
5. K. LANDFESTE: The Generation of Nanoparticles in Miniemulsions. Adv Mater, **10,** 765 (2001).
6. J. H. FENDLER: Colloid Chemical Approach to Nanotechnology. Korean J Chem Eng, **18** (1), 1 (2001).
7. M. A. LOPEZ – QUINTELA: Synthesis of Nanomaterials in Microemulsions: Formation Mechanisms and Growth Control. Curr Opin Colloid In, **8**, 137 (2003).
8. I. CAPEK: Preparation of Metal Nanoparticles in Water-in-Oil (w/o) Microemulsions. Adv Colloid Interfac, **110**, 49 (2004).
9. I. M. ISMAIL, H. A. EWAIS: Formation and Characterization of a Stable Aqueous Dispersion of Silver Nanoparticles in Aqueous and Micellar Media. A Kinetic Study. Oxid Commun, **39** (1), 62 (2016).
10. R. VALENCUELA, G. BUENO, A. SOLBES: Nanostructured Ceria-based Catalysts for Oxydehydrogenation of Ethane with CO_2. Top Catal, **15**, 2 (2001).
11. J. RYMES, G. EHRET, L. HILAÎRE, M. BOUTONNET, K. JIRATOVA: Microemulsions in the Preparation of Highly Active Combustion Catalysts. Catal Today, 7**5**, 297 (2002).
12. H. H. INGELSTEN, J. Ch. BEZIAT, K. BERGKVIST, A. PALMQVIST, M. SKOGLUNDH, H. QIUHONG, L. K. FALK, K. HOLMBERG: Deposition of Platinum Nanoparticle, Synthesized in Water-in-Oil Microemulsions on Alumina Supports. Langmuir, **18**, 1811 (2002).
13. Y. HE, B. YANG, G. CHENG, H. PAN: Synthesis of $La_2O_3/BaCO_3$ Nanocatalysts and Their Catalytic Performance. Powder Technol, 4773 (2003).
14. Y. HE, B. YANG, G. CHENG: On the Oxidative Coupling of Methane with Carbon Dioxide over CeO_2/ZnO Nanocatalysts. Catal Today, **98**, 595 (2004).
15. S. ERICKSSON, U. NYLEN, S. ROJAS, M. BOUTONNET: Preparation of Catalysts from Microemulsions and Their Application in Heterogeneous Catalysts. Appl Catal A-Gen, **265**, 207 (2004).
16. M. E. ASSAL, M. R. SHAIK, M. KUNIYIL, M. KHAN, A. AL-WARTHAN, M. RAFIQ, H. SIDDIQUI, S. F. ADIL: ZnO_x–$MnCO_3$, –MnO_2 OR –Mn_2O_3 Deposited on Highly Reduced Graphene Oxide Nanocomposites as an Efficient Catalyst for Aerial Oxidation of Different Types of Alcohols. Oxid Commun, **41** (3), 372 (2018).
17. P. TARTAJ, M. MORALES, S. VEINTEMILLAS-VERDAGUER: The Preparation of Magnetic Nanoparticles for Applications in Biomedicine. J Phys D-Appl Phys, **36,** 182 (2003).
18. A. K. PRADHAN: Growth and Magnetism of Ni Nanoparticles in $Ni/Al_2O_3/Si$ or Si_3N_4 Multilayers. Appl Surf Sci, **220**, 26 (2003).
19. X. ZHANG, J. LIU, Y. JING, Y. XIE: Support Effects on the Catalytic Behavior of NiO/Al_2O_3 for Oxidative Dehydrogenation of Ethane to Ethylene. Appl Catal A-Gen, **240**, 143 (2003).
20. P. TARTAJ, M. MORALES, S. VEINTEMILLAS-VERDAGUER: The Preparation of Magnetic Nanoparticles for Applications in Biomedicine. J Phys D-Appl Phys, **36**, 182 (2003).
21. WU SZU-HAU, DONG-HWANG CHEN: Synthesis and Characterization of Nickel Nanoparticles by Hydrazine Reduction in Ethylene Glycol. J Colloid Interf Sci, **259**, 282 (2003).
22. A. GEORGIEVA: Nanotechnology of Carbonate Nanostructures – Obtaining, Properties and Modeling. University 'Prof. D-r Assen Zlatarov' – Bourgas, 2017.

Received 26 February 2019
Revised 9 March 2019

Oxidation Communications 42, No 2, 132–137 (*2019*)

Biological and biochemical oxidation processes

DYNAMICS OF CONCENTRATION OF LACTATE IN COMPETITION IN RUNNING AT MIDDLE DISTANCES

I. LAZAROV

Department 'Track and Field', National Sports Academy, Sofia, Bulgaria
E-mail: *ivolazarov81@gmail.com*

ABSTRACT

The aim of the research is to increase the effectiveness of the training process in middle-distance running through disclosure and justification of the dynamics of lactate accumulation, as a marker for determining threshold levels of running loads. As effective research contingent persons recommend the following quantitative values of adaptation markers of respiratory and metabolic activities and accordingly their associated speed running: aerobic threshold – 2 mmol/l in running speed lower than 4.05 m/s and pulse limit to 160 h/min (zone for stabilising capacity of aerobic metabolic mechanism); anaerobic threshold – 4 mmol/l in pulse limit 160–175 h/min – effective aerobic zone (zone for economy development of aerobic insurance); 175–185 h/min – zone for developing maximum power of respiratory processes.

Keywords: lactate accumulation, adaptation markers, aerobic zone.

AIMS AND BACKGROUND

One of the aims of functional diagnostics in sports is the study of changes in the metabolism of the body energy supply during a certain training activity[1–5].

While the cardiovascular and respiratory systems transport oxygen and nutrients to the working muscles, the metabolic processes provide the energy needed for its work. Consequently, changes in the concentration of metabolites associated with the energy-supplying processes of muscle work are of particular diagnostic value for the assessment of physical capacity. Such a metabolite is lactic acid, which gives special attention in modern functional diagnostics[6]. Increased lactic acid formation occurs when the rate at which the energy needs of the working musculature increase exceeds that at which they are covering by aerobic decomposition of the substances of water and carbon dioxide[7,8].

Therefore, the increase in blood lactate concentration is an indicator of a change in energy supply of muscle work from aerobic to anaerobic. Assuming that changes in lactic acid concentration in arterial blood matches with those of ventilation, Holman[6] defines this point as the point of optimum breathing effectiveness. Therefore, it was defined as the ‘Threshold of Anaerobic Exchange’. In the current stage of the development of the functional role of functional diagnostics to improve the training methodology, the determination of the anaerobic threshold is a mandatory part of the protocols of all sports-functional diagnostic tests.

What is new in sports theory? In the practice is that these results are a function of studies conducted entirely in the conditions of the training activity. Such complex research activities of the cardiorespiratory system and metabolic effects of exercise, in this case running with progressive increases in speed were made only in laboratory conditions. Conducted our study allows us to compare the results of laboratory and field tests and thus to improve the regulatory system for monitoring and evaluation of adaptation processes that characterise the effectiveness of the training process.

The aim of the study is to increase the efficiency of the middle distance running by revealing and justifying the dynamics of lactate concentration as a marker for determining the threshold levels of the running loads.

The goal thus pursued involves the following tasks:

1. Exploring the functional capabilities of athletes in middle distance runs;
2. Analysis of the changes in the level of lactate concentration at standard load with progressive increase of the intensity;
3. Determination of quantitative values of adaptation markers of respiratory and metabolic activities.

EXPERIMENTAL

The object of the study was the adaptation changes in the lactate concentration in the conditions of the training activity.

Contingent includes 25 male middle distance competitors with results in 800 m from 1:47.14 to 1:54.75 min.

The competitors were tested in sports training. The test they performed was a 5 × 1000 m load over a 3-min passive pause with progressive time reduction (speed increasing) for each segment as follows: 1 – 4:00 min (4.17 m/s), 2 – 3:40 min (4.54 m/s), 3 – 3:15 min (5.13 m/s), 4 – 3:00 min (5.55 m/s), 5 – 2:50 min (5.88 m/s).

The test was performed on the athletics track using a special K4 set which recorded the pulse frequency and oxygen consumption dynamics in the load and rest phases between runs.

In addition, the concentration of lactate in capillary blood was measured as follows:

– a drop of blood from the earlobe or the finger of one of the two hands was taken at the first minute after the respective run, from which a lactate analyser was automatically read by the lactate analyser.

– after the last run, the blood sampling procedure was repeated at 6 and 12 min, i.e. took into the current elimination half-life (immediate recovery).

The data obtained correlated to the corresponding running speed with a mathematical analysis of the respective correlation and regression dependences.

RESULTS AND DISCUSSION

Table 1 shows the result of the variance analysis of the researched functional mark, which confirm the thesis. At the same time, although the body is working at a similar level, the amount of oxygen that provides the systems is inadequate and the body falls into a state of deep acidosis. Training that develops resistance to such conditions requires precise determination of the critical levels in the workings of the body's main systems, and in particular the cardiorespiratory.

Table 1. Variance analysis of functional mark

	n	X_{min}	X_{max}	*R*	*X*	*S*	*V*	K	Sk
VO_{2max}	25	60.4	77.80	17.40	67.40	4.11	7.10	1.82	0.61
vVO_{2max}	25	4.2	5.90	1.70	5.15	0.51	10.50	–0.83	0.11
vAnT	25	3.5	4.85	1.35	4.14	0.31	4.04	–0.61	0.28
vAeT	25	3.6	4.50	0.90	4.21	0.22	5.91	2.11	1.53
vrdst	25	4.4	6.80	2.40	5.50	0.52	9.90	1.83	–0.54
$htrVO_{2max}$	25	186	217	31	205	5.91	2.79	0.69	0.84
htrAnT	25	170	195	25	185	7.75	3.98	0.11	0.42
htrAeT	25	140	176	36	157	7.54	4.57	–0.28	0.12

Legend: X_{min} – lowest values, X_{max} – highest values, *R* – spread, *X* – mid-range, *S* – standard deviation, *V* – variation, K – kurtosis, Sk – skewness; VO_{2max} – maximum oxygen consumption, vVO_{2max} – speed of running in maximum oxygen consumption, vAnT – speed of anaerobic threshold, vAeT – speed of aerobic threshold, vrdst – maximum running speed (m/s), $htrVO_{2max}$ – heart rate in maximum oxygen consumption, htrAnT – heart rate in threshold of anaerobic possibilities, htrAeT – heart rate in threshold of aerobic possibilities.

Figure 1 shows the data from the processing of the results of the study. The two graphs – the factual and the logarithmic – show the main trends that characterise the dependence between the power of the breathing processes and the lactic accumulation in the capillary blood. Comparing the dynamics and the location of these curves gave us reason to fix the following two 'critical' (inflectional) points of adaptation changes in the metabolism of energy processes:

– the first one corresponds to the first intersection of the two curves at 2.5 mmol/l capillary blood lactate content provided by an oxygen supplement of 45 ml per kg of body weight per min.

– the second one corresponds to the next intersection of the two curves with a capillary blood lactate content of 4 mmol/l provided by an oxygen supply of 58 ml per kg of body weight.

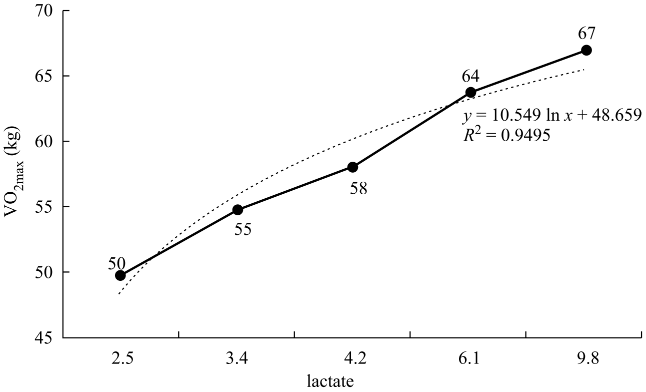

Fig. 1. Logarithmic expression of the interdependence between VO_{2max}/kg and lactate

The results define the two 'thresholds' of the energetic metabolism of physical performance: 'aerobic' and 'anaerobic'. Identifying the intensity of muscular work that provokes transitions from one area to another is a central issue of the theory and practice of functional training in sport, in general, and of course, in particular. Our research confirmed the scientific hypothesis that the interdependence between the dynamics of metabolic acidosis and the progressive increase in the intensity of muscle work is exponential. This phenomenon confirmed by the dynamics of the graphs of Fig. 2. The interaction of the graphs (factual and theoretical) implies almost functional dependence, which is confirmed by the correlation coefficient ($r = 0.9645$).

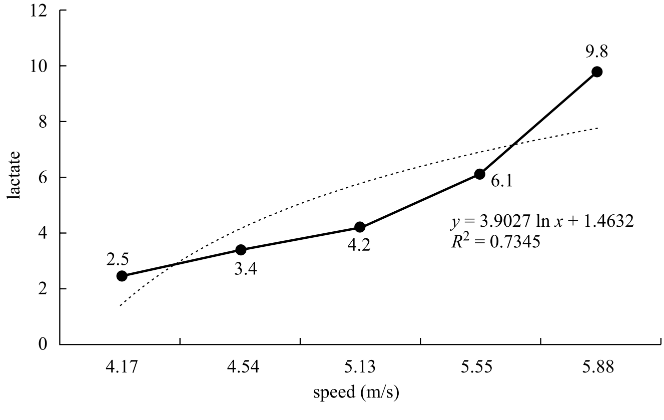

Fig. 2. Graphical expression of the exponential dependence between running speed and lactate concentration

Adaptive markers defined by the above dependence are as follows: Running speed in effective aerobic mode of 4.17 m/s up to 5.13 m/s or translated into the 'language of practice' at 4:07 min/km (24.69″ per 100 m) to 3:34 min/km (21.41″ per 100 m), i.e. running efforts aimed at improving functional capabilities should conduct at a running speed within that range. The values given are valid mainly for the competitor (middle distance elite athletes – men and women) or those with a similar qualification. To facilitate the control of the functional effect of the applied running loads, we have supplemented the data with the results of the pulse behaviour analysis in the relevant metabolic zones.

The graphs in Fig. 3 reveal the behavioral dynamics of this indicator and its relationship to the development of metabolic acidosis processes in the course of running load with a progressive increase in intensity. This dependence is expected to be exponential. It repeats one of the tendencies described so far defining the quantitative parameters of the respective critical (adaptation) markers. The first critical point is 2.2 mmol of lactate associated with a pulse rate of 157 h/min. The second critical point – 4 mmol lactate at a pulse rate of 178 h/min. Here, however, we also find a third critical point that corresponds to 5.5 mmol and pulse rate 185 h/min. These values complement the information on the determinate effective aerobic work area of muscle work, which in this case is limited in the pulse range from 157 to 178 h/min. At the same time, one of the most popular functional prepairnes indicators is the pulse rate dynamics in rest pauses.

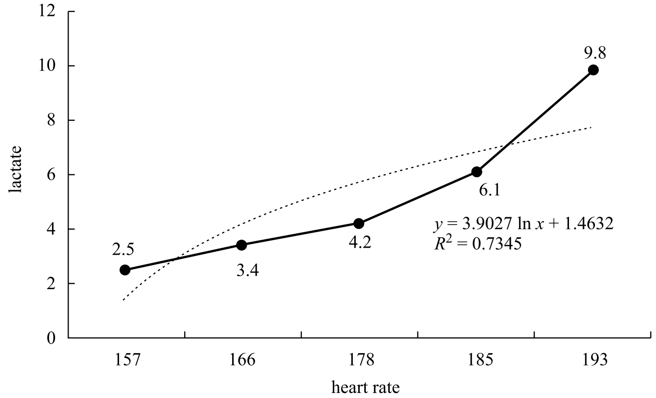

Fig. 3. Graphical expression of the exponential dependence between heart rate and lactate accumulation in capillary blood

The data from the study allowed a quantitative analysis of its dependence with lactate accumulation, which also measures in the resting phase between individual 1000-meter segments, and the corresponding pulse and lactate values immediately before the start of the test load. As can be seen (Fig. 4), the polynomial dependence between the dynamics of pulse recovery and lactate accumulation is functional (R = 0.9911). The medium and high intensity areas are clearly defined, as well as the quantitative data reflecting the degree of training and adaptability to the applied running loads. This phenomenon is extremely important in the implementation of operational control and regulation of the running loads. The resulting quantitative limits of metabolic processes reveal wide possibilities for improvement of the methodology for individual functional training.

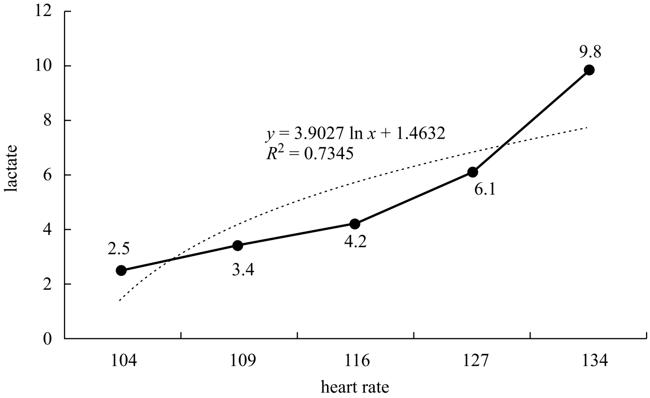

Fig. 4. Graphic representation of the polynomial dependence between heart rate in the phases of rest and lactic acid accumulation in capillary blood

CONCLUSIONS

As effective persons, we recommend the following quantitative values of the respiratory and metabolic adaptation markers and their associated running speeds:

– Aerobic threshold – 2 mmol/l at a running speed of less than 4.05 m/s and a pulse limit of up to 160 h/min (zone stabilising the capacity of the aerobic metabolic mechanism);

– Anaerobic threshold – 4 mmol/l at pulse limit 160–175 h/min – an effective aerobic zone (development area aerobic safety area); 175–185 h/min – a zone developing maximum breathing power).

REFERENCES

1. P. BONOV: Running Endurance and Adaptation. Sofia, Tip-top Press, 2003 (in Bulgarian).
2. D. DASHEVA: Training and Adaptation in Sport. Bins, Sofia, 2002 (in Bulgarian).
3. F. W. DICK: Sports Training Principles. A&C Black, London, 2002.
4. V. FURNADJIEV, I. ABADJIEV: Adaptation in Sport. NSA, Sofia, 2005 (in Bulgarian).
5. S. NEIKOV, D. DASHEVA: Planning and Management of the Final Stage of Preparation for Major Competitions of Elite Athletes. Sport and Science, (1), 7 (2017) (in Bulgarian).
6. N. GRANCHAROV: Anaerobic Threshold – Nature and Applied Value. PhD Thesis, NSA, Sofia, 1997.
7. P. O. ASTRAND, K. RODAHL: Textbook of Work Physiology. New York – St. Louis, 1986, 120–122.
8. J. BAUCKAERT, J. VRIGENS, J. PAUNER: Effect Special Tests Procedures on Plasma Lactate Concentration and Epoxy Oxygen Uptake in Endurance Athletes. The Journal of Sport Medicine and Physical Fitness, **30**, 12 (1999).

Received 9 April 2019
Revised 15 April 2019

Oxidation Communications 42, No 2, 138–150 (2019)

Medical image processing

LUNG CANCER DIAGNOSIS USING HYBRID DRAGONFLY OPTIMISATION AND RADIAL BASIS NEURAL NETWORK CLASSIFICATION

F. LEENAVINMALAR*, A. KUMAR KOMBAIYA

Department of Computer Science, Chikkanna Goverment Arts College, Tirupur, India
E-mail: *leenavinmalar.f@yahoo.com*

ABSTRACT

Recent medical research has common challenges and issues based on lung cancer diagnosis. Reasons for lung cancer strongly correlated with using tobacco and cigarettes in regular days. This research is concentrated on the data set consisting of five normal and five abnormal patients for lung cancer prognosis. The data set is padded with data to facilitate the classification of gene expression. The statistical calculations were performed on the gene expression to extract the features. The feature with the highest score is one of the features for training the network. The feature, which gives the least error rate for training the network, is the second feature of the network. In the present work the radial basis neural network is used. The features from PCA (Principal component analysis) and dragonfly are used for training. The data set is classified as testing and training using cross-fold validation. Proposed research provides an improved performance metrics estimation. Performance metrics are classified as accuracy, sensitivity and specificity and are utilised in medical treatment and prognosis application.

Keywords: radial basis neural network, lung cancer diagnosis, PCA, gene expression data set, dragonfly, performance evaluation.

AIMS AND BACKGROUND

Lung cancer is one of the common cancer type and based on calculating results of the 2019 survey list presents 250 000 deaths, 325 000 cases and $13 billion in health care. The major objectives of this research work are lung cancer diagnosis, tissue and abnormal cell growths identification. This is occurring from using tobacco and cigarette habits to kill people survival life time. Clinical report is based on five normal and five

---

[*] For correspondence.

abnormal patients and data are collected to identify lung cancer disease diagnosis. Also, the data of the proposed research work were compared to the previous research work with minimum performance metric efficient level. The proposed lung cancer diagnosis technique research work is providing an improved performance metrics estimation by using feature extraction and classification technique.

Chellappan et al.[1] presented lung cancer disease prognosis by using disease affected CT (Computed tomography) images. Bag of visual words (BoVW) is used to image classification section. Graphical representation of simulation outputs is obtained using MATLAB 2016 version. This class presents 96% best results comparing with other classifier segments. The BoVW classification method may enhance the automatic prognosis of lung cancer pictures. This BoVW minimises the computational complexity. CAD is one of the benefit of this research work.

Guan et al.[2] proposed regulatory subunit of ribonucleotide reductase (RRM1) and repair cross-complementing one gene in image processing feature analysis scheme. Prognosis of lung cancer is as a normal stage for computer tomography pictures based. Here protein articulation and two genomic bio concepts were used. The output of this research work presents an area under curve values. Two multilayer classifiers further enhanced prediction performance. Kaplan-Meier investigation displays between starting lung disease to corresponding survival and anticipated to correlative survival by three different methods. This helps clinicians in a precisely arranging dimension I NSCLC patients to limit malignant growth repeat chances.

McWilliams et al.[3] have found that Volatile organic compounds (VOCs) in exhaled breath as measured by electronic nose (e-nose) could be used as biomarkers to detect subjects at risk of having lung cancer in a screening setting. Here, a sensor resistivity cluster was utilised as a screening tool to discriminate patients diagnosed with lung cancer from high-risk smokers. This is one of the significant advantages of this exploration. Execution assessment relies on patient age, sex and cigarette smoking report accomplished under differently repeatable conditions. The proposed graphical view depends on the region under the bend, the sensitivity and specificity of the performance metric numerical values configuration.

Balagurunathan et el.[4] presented classification of two common sub-types of lung cancer. They are: NSCLC (non-small cell) and SCLS (small-cell lung cancer). In this NSCLC and SCLS diagnosis by using CT scan images, 3-D features are selected in radiomics configuration. If the feature selection section presents 77% of output determination is based on cross calculation. Data sets are used to feature selected segment. The result shows the sample computed tomography lung cancer image. Feature selection presents an initial lung cancer image. Classified as two segments they are lung segmentation and tumor segmentation. Finally, graphical representation presents the Kaplan-Meier stimulation output.

Raut et al.[5] presented Network markers (NMs), based on identifying cancer types by using various gene expression data sets from micro array and RNA sequence platform. Features are extracted from DEGs (Differentially Expressed Genes) to RNA sequence. Hub nodes are observed the cancer network growth and classification. Thus, breast cancer and lung cancer are identified. Here, PPI data parameterising gene groups are at LFC > 2, log-FC (LFC) > 1, and LFC > 1.5 and the interconnection between hub nodes.

EXPERIMENTAL

PROPOSED HYBRID DF-RBFN RESEARCH WORK

The data set was padded with its data to facilitate the classification of gene expression. The statistical calculations were performed on gene expression method to extract the features. It was performed in two stages. The first stage is PCA having highest score will be one of the first feature for training network. The second stage is dragonfly, which gives the least error rate for training the network and will be the second feature of the network. Classification segment was based on the Radial basis neural network. Training state was performed based on the features, they were named as PCA and dragonfly. The data set was classified as testing and training. The cross-fold validation function was the initial state of testing and training. Performance evaluation identified as following metrics: Accuracy, Sensitivity, Specificity. The research work on lung cancer prognosis is to get lots of efficient performance metrics estimation by using proposed Hybrid DF-RBFN concept research work (Fig. 1) .

LUNG CANCER DATA SET

Lung cancer Gene expression data set reports were collected from http://biogps.org/#goto=generepor t&id=1017&show_dataset=E-GEOD-23066. The data consisted of 5 normal and 5 abnormal patients.

Gene expression. Gene regulation gives the cell control over functionality and structure, the basis for cellular differentiation, morpho genesis and the versatility and adaptability of any organism. Several steps in the gene expression process may be changed, including the transcription, splicing, translation, RNA and post-translational modification of a protein. Gene expression is the process by which data from a gene are used in the synthesis of a functional gene product. These products are often proteins, but in non-protein coding genes such as transfer RNA (tRNA) or small nuclear RNA (snRNA) genes, the product is a functional RNA. This configuration used for lung cancer based gene expression data set. Collected by using the Biogps web site.

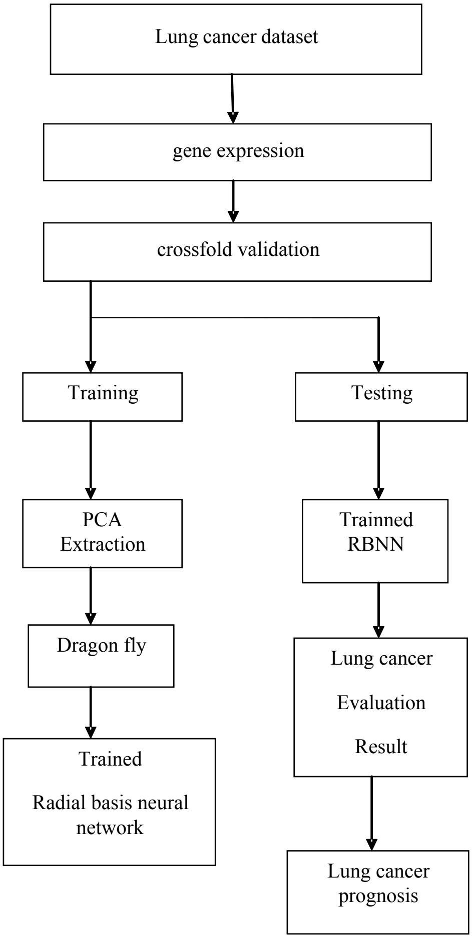

Fig. 1. Radial basis neural network-based lung cancer prognosis

Cross-fold validation. The cross-fold validation function was used for the statistical calculations, performed on the gene expression to extract the features. This presents the accurate evaluation of performance prediction.

$$1/n \sum_{i=1}^{n} (y_i - a - \beta^{\mathrm{T}} x_i)^2 = 1/n \sum_{i=1}^{n} (y_i - a - \beta_i x_i - \ldots - \beta_p x_{ip})^2 \quad (1)$$

Table 1. Cross-fold pseudo code

```
Input:

x, {vector of length N with x-values of data points}

y, {vector of length N with y-values of data points}

Output:

err, {estimate for the prediction error}

Steps:

err ← 0

for i ← 1, . . . , N do

    // define the cross-validation subsets

    x_in ← (x[1], . . . , x[i − 1], x[i + 1], . . . , x[N])

    y_in ← (y[1], . . . , y[i − 1], y[i + 1], . . . , y[N]

    x_out ← x[i]

    y_out ← interpolate(x_in, y_in, x_out, y_out)

    err ← err + (y[i] − y_out)^2

end for

err ← err/N
```

Cross-fold pseudo-code has one or numerous vague quality attributes (Table 1). On the off chance dataset fits to the preparation dataset arrangement. Fitting procedure additionally takes an autonomous dataset test approval from comparable populaces of a preparation set quality. Ordinarily, turn out and does not fit the approval information, yet fits the preparation informational collection. Different sizes of the dataset (i.e. small, medium, large) and numerical estimation of quality trademark way are gauge cross-approval size of quality impacts.

PCA extraction. PCA distinguishes the eigenvectors of a covariance grid with the most astounding eigenvalues and dimensionality decrease systems. PCA has least loss of the absolute information. This highlight determination keeps the highlights flawless and chooses *n* – number of the best features, among them, disposing of the co-direct and excess highlights. The PCA change is the direct change that most precisely reproduces the quality preparing informational index. The ideal PCA lattice is gotten utilising a Singular value decomposition (SVD). In AI task, the significance of properties dependent on the class type was assessed. PCA feature choice is a procedure of progressive the given list of capabilities as indicated by couple of exhibitions metric with the goal that the least huge highlights can be disposed of from the issues.

Table 2. Dragonfly pseudo-code

```
Initialize the dragonflies population Xi (i = 1, 2,..., n)
Initialize step vectors ΔXi (i = 1, 2, ..., n)

while the end condition is not satisfied

    Calculate the objective values of all dragonflies
    Update the food source and enemy
    Calculate
    Update neighbouring radius

    if a dragonfly has at least one neighbouring dragonfly

        Update velocity vector
        Update position vector
        Update position vector
    end if
    Check and correct the new positions based on the boundaries of variables
end while
```

Dragonfly (Table 2) is expressed as:

$$D^{K+1}a = D^{S}_{a} + F\,D\,\exp(-\gamma r^{2}_{ab})(D^{K}_{b} - D^{K}_{a}) + \alpha_{K}\,\varepsilon_{K} \tag{2}$$

which, optimises

$$D(h) = F_1(h), F_2(h), ..., F_M(h), M = 1, ..., n, \text{ value} \tag{3}$$

The following equation provides when gene expression is maximum variance:

$$\arg\min_{S} \sum_{i=1}^{k} \frac{1}{2|S_i|} \sum_{x,y\in S_i} \|x-y\|^2 \tag{4}$$

where

$$\sum_{x\in S_i} \|x - \mu_i\|^2 = \sum_{x\neq y\in S_i} (x - \mu_i)(\mu_i - y). \tag{5}$$

A dragonfly optimisation has been genetically changed with light-sensitive ‘steering neurons’ in this nerve cord to make a cyborg-like ‘Dragonfly Eye’. The neurons consist of genes such as those in the eye to create them sensitive to light.

Radial basis neural network (Fig. 2). In the field of mathematical modelling, a radial basis neural network is an artificial neural network that uses radial basis functions as activation functions. Radial basis neural networks (RBNN) have many uses, including function approximation, time series prediction, classification, and system control. The output of the network is a linear combination of radial basis functions of the inputs and neuron parameters.

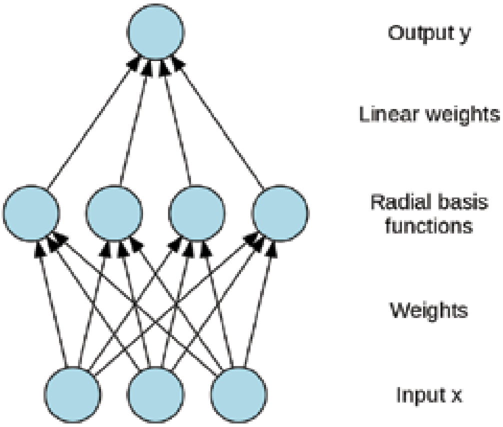

Fig. 2. Radial basis neural network

The input can be modelled as a vector of real numbers $x \in R^n$. The output of the network is then a scalar function of the input vector, $\varphi: R^n \rightarrow R$, and is given by:

$$\varphi(x) = \sum_{i=1}^{N} a_i \rho(\|x - c_i\|) \tag{6}$$

where N is the number of neurons in the hidden layer; c_i – the centre vector for neuron i, and a_i – the weight of neuron i.

Radial basis function is commonly taken to be Gaussian:

$$\rho(\|x - c_i\|) = \exp(-\beta \, \|x - c_i\|^2) \tag{7}$$

The Gaussian basis functions are local to the centre vector in the sense that:

$$\lim_{\|x\|\rightarrow\infty} \rho(\|x - c_i\|) = 0 \tag{8}$$

$$a_i(t+1) = a_i(t) + v(y(t) - \varphi(x(t), w)) \frac{\rho(\|x(t) - c_i\|)}{\sum_{i=1}^{N} \rho^2(\|x(t) - c_i\|} \quad (9)$$

Unnormalised case:

$$e_{ij}(t+1) = e_{ij}(t) + v(y(t) - \varphi(x(t), w)) \frac{v_{ij}(x(t) - c_i)}{\sum_{i=1}^{N} \sum_{j=1}^{n} v_{ij}^2(x(t) - c_i)} \quad (10)$$

Normalised case:

$$e_{ij}(t+1) = e_{ij}(t) + v(y(t) - \varphi(x(t), w)) \frac{v_{ij}(x(t) - c_i)}{\sum_{i=1}^{N} \sum_{j=1}^{n} v_{ij}^2(x(t) - c_i)} \quad (11)$$

In the local-linear case:

For one basis function, projection operator training reduces to the Newton scheme.

Performance analysis. Performance metrics are estimated for each factor for feature testing and classification purposes (Fig. 3).

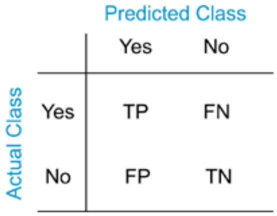

Actual Class		Predicted Class	
		Yes	No
	Yes	TP	FN
	No	FP	TN

Fig. 3. Confusion matrix for RBNN

Actual class and Predicted class wise determined the following parameter metrics:

$$\text{accuracy} = \frac{\text{true positive} + \text{true negative}}{\text{true positive} + \text{true negative} + \text{false negative} + \text{false positive}};$$

$$\text{sensitivity} = \frac{\text{true positive}}{\text{true positive} + \text{false negative}};$$

$$\text{specticity} = \frac{\text{true negative}}{\text{true negative} + \text{false positive}}.$$

RESULTS AND DISCUSSION

Lung cancer gene expression data set was collected from following web http://biogps.org/#goto= gener eport&id=1 017&showdataset=E-GEOD-23066. The data consist of five normal and five abnormal patients (Figs 4 and 5).

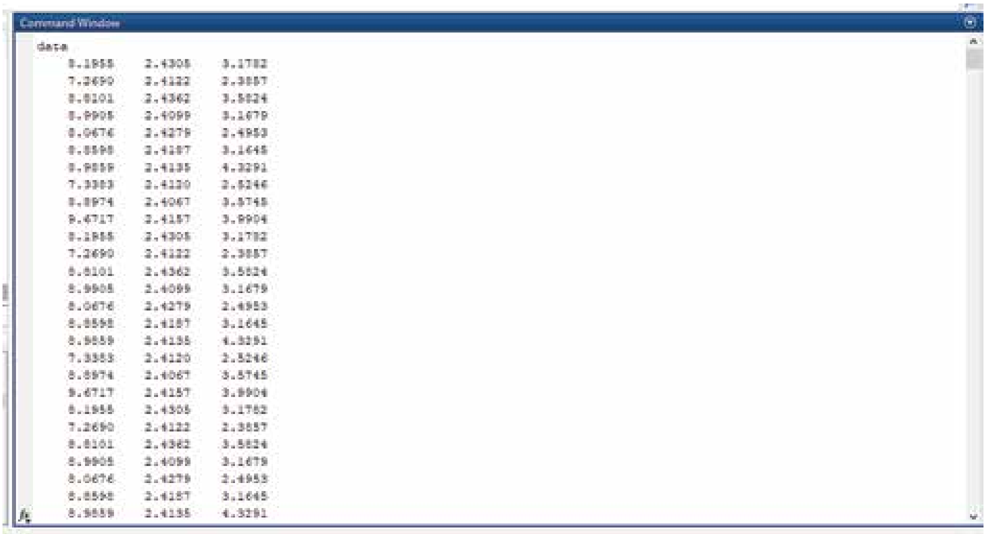

```
data
    8.1955    2.4305    3.1782
    7.2690    2.4122    2.3857
    8.8101    2.4362    3.5824
    8.9905    2.4099    3.1679
    8.0676    2.4279    2.4953
    8.8598    2.4187    3.1645
    8.9859    2.4135    4.3291
    7.3383    2.4120    2.5246
    8.8974    2.4067    3.5745
    9.6717    2.4157    3.9904
    8.1955    2.4305    3.1782
    7.2690    2.4122    2.3857
    8.8101    2.4362    3.5824
    8.9905    2.4099    3.1679
    8.0676    2.4279    2.4953
    8.8598    2.4187    3.1645
    8.9859    2.4135    4.3291
    7.3383    2.4120    2.5246
    8.8974    2.4067    3.5745
    9.6717    2.4157    3.9904
    8.1955    2.4305    3.1782
    7.2690    2.4122    2.3857
    8.8101    2.4362    3.5824
    8.9905    2.4099    3.1679
    8.0676    2.4279    2.4953
    8.8598    2.4187    3.1645
    8.9859    2.4135    4.3291
```

Fig. 4. Patients data

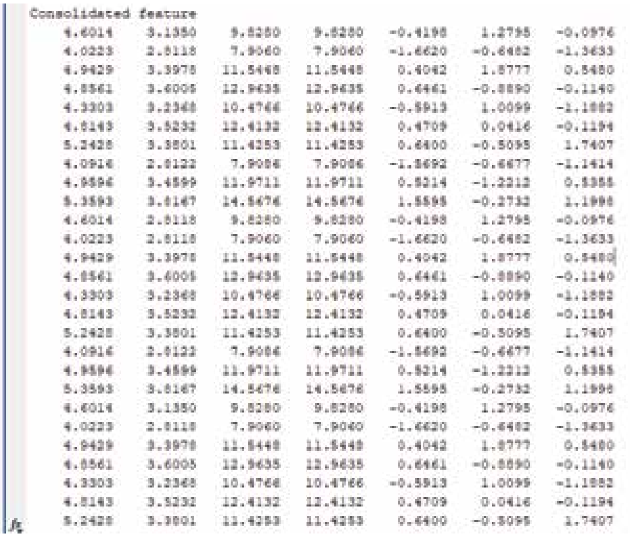

```
Consolidated feature
    4.6014    3.1350    9.8280    9.8280   -0.4198    1.2795   -0.0976
    4.0223    2.8118    7.9060    7.9060   -1.6620   -0.6482   -1.3633
    4.9429    3.3978   11.5448   11.5448    0.4042    1.8777    0.5480
    4.8561    3.6005   12.9635   12.9635    0.6461   -0.8890   -0.1140
    4.3303    3.2368   10.4766   10.4766   -0.5913    1.0099   -1.1882
    4.8143    3.5232   12.4132   12.4132    0.4709    0.0416   -0.1194
    5.2428    3.3801   11.4253   11.4253    0.6400   -0.5095    1.7407
    4.0916    2.8122    7.9086    7.9086   -1.5692   -0.6677   -1.1414
    4.9596    3.4599   11.9711   11.9711    0.5214   -1.2212    0.5355
    5.3593    3.8167   14.5676   14.5676    1.5595   -0.2732    1.1998
    4.6014    2.8118    9.8280    9.8280   -0.4198    1.2795   -0.0976
    4.0223    2.8118    7.9060    7.9060   -1.6620   -0.6482   -1.3633
    4.9429    3.3978   11.5448   11.5448    0.4042    1.8777    0.5480
    4.8561    3.6005   12.9635   12.9635    0.6461   -0.8890   -0.1140
    4.3303    3.2368   10.4766   10.4766   -0.5913    1.0099   -1.1882
    4.8143    3.5232   12.4132   12.4132    0.4709    0.0416   -0.1194
    5.2428    3.3801   11.4253   11.4253    0.6400   -0.5095    1.7407
    4.0916    2.8122    7.9086    7.9086   -1.5692   -0.6677   -1.1414
    4.9596    3.4599   11.9711   11.9711    0.5214   -1.2212    0.5355
    5.3593    3.8167   14.5676   14.5676    1.5595   -0.2732    1.1998
    4.6014    3.1350    9.8280    9.8280   -0.4198    1.2795   -0.0976
    4.0223    2.8118    7.9060    7.9060   -1.6620   -0.6482   -1.3633
    4.9429    3.3978   11.5448   11.5448    0.4042    1.8777    0.5480
    4.8561    3.6005   12.9635   12.9635    0.6461   -0.8890   -0.1140
    4.3303    3.2368   10.4766   10.4766   -0.5913    1.0099   -1.1882
    4.8143    3.5232   12.4132   12.4132    0.4709    0.0416   -0.1194
    5.2428    3.3801   11.4253   11.4253    0.6400   -0.5095    1.7407
```

Fig. 5. Consolidated feature

The statistical calculations were performed on the gene expression to extract the features. It was performed in two stages.

```
PCA dominant feature
    4.6014
    4.0223
    4.9429
    4.8561
    4.3303
    4.8143
    5.2428
    4.0916
    4.9596
    5.3593
    4.6014
    4.0223
    4.9429
    4.8561
    4.3303
    4.8143
    5.2428
    4.0916
    4.9596
    5.3593
    4.6014
    4.0223
    4.9429
    4.8561
    4.3303
    4.8143
    5.2428
```

Fig. 6. PCA

The first stage is PCA (Fig. 6). This feature estimated with the highest score will be one of the feature for training the network.

```
Dragon fly dominant feature
   -0.0976
   -1.3433
    0.5480
   -0.1140
   -1.1082
   -0.1194
    1.7407
   -1.1414
    0.5355
    1.1998
   -0.0976
   -1.3433
    0.5480
   -0.1140
   -1.1082
   -0.1194
    1.7407
   -1.1414
    0.5355
    1.1998
   -0.0976
   -1.3433
```

Fig. 7. Dragonfly

The second stage is dragonfly optimisation (Fig. 7). Here, a feature which gives the least error rate for training the network will be the second feature of the network. The features from PCA and dragonfly are used for training. The data set is classified as testing and training using crossfold validation (Fig. 8).

```
ACCURACY
    91

SENSITIVITY
    90

SPECIFICITY
    91

>> |
```

Fig. 8. Proposed hybrid DF-RBFN performance metrics evaluation

Table 3. Performance metrics

Performances	Existing method	Proposed method
Metric	Prefiltering & GBS	Hybrid DF-RBFN
Accuracy	79.4	91
Sensitivity	80.0	90
Specificity	79.4	91

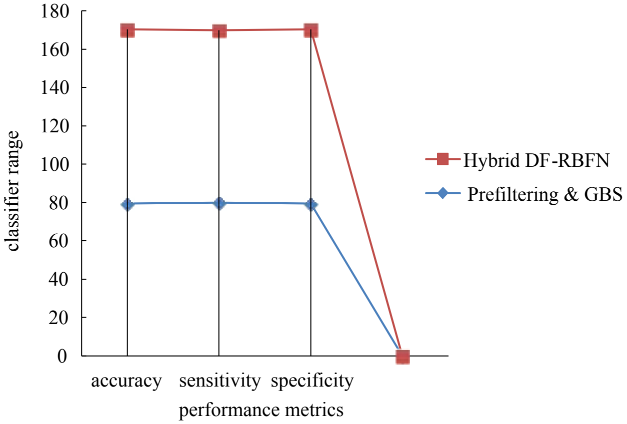

Fig. 9. Graph for performance analysis

In Fig. 9 is shown the graphical representation of the previous research work pre-filtering concept and the proposed Hybrid DF-RBFN concept based on Table 3. The Hybrid Dragon Filter and Radial basis function network (Radial basis neural network) concept wise performance metrics are estimated by improved manner.

CONCLUSIONS

In the proposed research work is proved the efficient diagnosis of lung cancer by using Dragonfly optimisation (DA), PCA, Gene expression data set, improved radial basis neural network concept and performance metrics. Proposed research provides an improved performance metrics estimation. The accuracy level is 91%, sensitivity level is 90%, and specificity level is 91%.

REFERENCES

1. T. D. CHELLAN, A. K. CHELLAPPAN: Novel Computer-aided Diagnosis of Lung Cancer Using Bag of Visual Words to Achieve High Accuracy Rates. The Journal of Engineering, (12), 1941 (2018).
2. N. EMAMINEJAD, W. QIAN, Y. GUAN, M. TAN, Y. QIU, H. LIU, B. ZHENG: Fusion of Quantitative Image and Genomic Biomarkers to Improve Prognosis Assessment of Early Stage Lung Cancer Patients. IEEE T Bio-Med Eng, **63** (5), 1034 (2016).
3. A. McWILLIAMS, P. BEIGI, S. LAM, C. E. MACAULAY: Sex and Smoking Status Effects on the Early Detection of Early Lung Cancer in High-risk Smokers Using an Electronic Nose. IEEE T Bio-Med Eng, **62** (8), 2044 (2015).
4. S. H. HAWKINS, J. N. KORECKI, Y. BALAGURUNATHAN, R. J. GILLIES: Predicting Outcomes of Nonsmall Cell Lung Cancer Using CT Image Features. IEEE access, **2**, 1418 (2014).
5. R. K. MAKHIJANI, S. A. RAUT, H. J. PUROHIT: Fold Change Based Approach for Identification of Significant Network Markers in Breast, Lung and Prostate Cancer. IET Systems Biology, (2018).
6. N. MELLIOS, M. SUR: The Emerging Role of Micro RNAs in Schizophrenia and Autism Spectrum Disorders. Frontiers in Psychiatry, **3**, 39 (2012).
7. V. IYER, R. NANDAKUMAR, A. WANG et al.: Living IoT: a Flying Wireless Platform on Live Insects. arXiv preprint arXiv:1812.09419, 2018.
8. M. GUO, I. FINK-BALDAUF, Y. MAEDA: Abstract A30: Gene Regulatory Mechanisms Governing Invasive Mucinous Adenocarcinoma of the Lung (IMA). 2018.
9. A. HERREROS-POMARES, J. D. De MAYA, H. AMADO, R. FARRAS: A Gene Expression Signature to Characterize Human Lung Adenocarcinoma Cancer Stem Cells. J Clin Oncol, (2018).
10. R. A. SOO, S. M. LIM, N. L. SYN, R. TENG, B. C. CHO: Immune Checkpoint Inhibitors in Epidermal Growth Factor Receptor Mutant Non-small Cell Lung Cancer: Current Controversies and Future Directions. Lung Cancer, **115**, 12 (2018).
11. C. DRESLER, G. W. WARREN, D. ARENBERG, M. K. J.JASSEM: Teachable Moment Interventions in Lung Cancer: Why Action Matters. J Thorac Oncol, **13** (5), 603 (2018).
12. X. WANG, Z. JIA, C. PAN: Identification and Evaluation of Two Circulating Micro RNA s for Non-small Cell Lung Cancer Diagnosis. Clin Exp Pharmacol, (2018).
13. R. HUIDROM, Y. J. CHANU, K. M. SINGH: A Fast Automated Lung Segmentation Method for the Diagnosis of Lung Cancer. In: Proceedings of the Region 10 Conference, TENCON 2017-2017 IEEE, 2017, 1499-1502.
14. H. AZZAWI, J. HOU, R. ALANNI: Lung Cancer Prediction from Microarray Data by Gene Expression Programming. IET Syst Biol, **10** (5), 168 (2016).
15. C. LIU, Y. DENG, R. ZHANG: Early Diagnostic Value of Circulating MiRNA-21 in Lung Cancer: a Meta-analysis. Tsinghua Science and Technology, **18** (5), 441 (2013).
16. A. C. SILVA, M. GATTASS: Diagnosis of Solitary Lung Nodule Using Texture Geometry in Computerized Tomography Images: Preliminary Results. IEEE Lat Am T, **2** (2), 75 (2004).

17. S. CHEN, K. SUZUKI: Computerized Detection of Lung Nodules by Means of ‘Virtual Dual-Energy’ Radiography. IEEE T Bio-Med Eng, **60** (2), 369 (2013).
18. I. MAGLOGIANNIS, H. SARIMVEIS, V. AIDINIS: Radial Basis Function Neural Networks Classification for the Recognition of Idiopathic Pulmonary Fibrosis in Microscopic Images. IEEE T Inf Technol B, **12** (1), 42 (2008).
19. C. WANG, D. J.HILL: Learning from Neural Control. IEEE T Neural Networ, **17** (1), 130 (2006).
20. M. J. ABINASH, V. VASUDEVAN: A Hybrid Forward Selection Based LASSO Technique for Liver Cancer Classification. In: Nanoelectronics, Circuits and Communication Systems. Springer, Singapore, 2019, 185-193.

Received 6 April 2019
Revised 25 April 2019

Oxidation Communications 42, No 2, 151–159 (2019)

Medical image processing

LITERATURE SURVEY OF IMAGE COMPRESSION/ DECOMPRESSION TECHNIQUES FOR SPACE AND TELEHEALTH APPLICATIONS

K. PRANITHA*, G. KAVYA

Department of Electronics and Communication Engineering, S.A Engineering College, Chennai-77, India
E-mail: *pranithayashika@gmail.com*

ABSTRACT

Image compression refers to convert data of more memory storage to the lesser one. Image data compression becomes foremost method for reducing the data redundancy to save more hardware area and transposal capacity. Image compression techniques are mainly used in space and telehealth applications. Image decompression is to give back the original image; it is an application to get much better image in terms of quality or size and also original image are obtained from their compressed form. Various algorithms for image compression/decompression techniques in previous works for space and telehealth applications are: watermarking algorithm, clustering-based compression method, improved watershed transform method, Set partitioning in hierarchical trees (SPHIT) algorithm, Discrete wavelet transform (DWT) with Bit plane encoding (BPE), Content based adaptive scanning method, Adaptive lifting DWT and modified SPIHT algorithm.

Keywords: image compression, image decompression, DWT with BPE, SPIHT, watermarking, clustering.

AIMS AND BACKGROUND

Imaging effect deals with capturing, storing, manipulating, and displaying of images. In graphics, it gives rise to special features like blurring, rotating, resizing, stretching, etc. changes made to the original image. Image processing is of two types – analog and digital image processing. Analog image processing is the form of hard copies like photographs. Digital image processing techniques are image preprocessing, enhancement, segmentation, feature extraction, classification, compression/decompression. Image processing is used in various applications like remote sensing, medical imaging,

---

[*] For correspondence.

non-destructive evaluation, forensic studies, textiles, material science, military, film industry, document processing, graphic arts, printing industry, etc. Image compression is a type of data compression applied to the digital images to reduce their cost for storage or transmission. Image compression may be lossy or lossless. Lossless often is used for medical imaging. Lossy often is used for natural images such as photographs and in satellite imaging. Image decompression provides a restored image with reduced visibility of transform coding artifacts and improved perceived quality. This paper gives an overview of image compression and various compression methods and summarises existing compression and decompression algorithms.

LITERATURE REVIEW OF COMPRESSION METHODS FOR SPACE AND TELEHEALTH APPLICATIONS

Satellite multispectral image compression method[1]. It is based on removing subbands to decrease the storage size of multispectral images with high quality resolution. Here discrete wavelet transform with entropy coder are adopted to perform compression process. By using this technique, image quality obtained by 3–11 db. Enhanced Thematic Mapper plus based satellite multispectral images are used to perform validation for the above compression technique.

Binary tree coding with adaptive scanning order (*BTCA*)[2]. It is an appropriate algorithm to provide compression with low complexity. BTCA provide large memory space but it does not provide Random Access Memory (RAM). But in this paper, a new coding technique BTCA with optimum truncation is used. According to BTCA, images are divided into several blocks which are encoded individually. It will select the valid truncation points for each block to optimise the ratio of distortion at high CR with low memory requirement and RAM is obtained. Remote sensing image data are large in size so that they require compression with low-complexity algorithm which can be used for space-borne equipment. This method is simple and fast which is suitable for space borne equipment. It improves PSNR as well as image visual quality.

Wavelet transform followed by adaptive scanning method[3]. This compression technique is preferred for a remote sensing image which is suitable for the on board compression. Wavelet transform is used to reduce the storage size and adaptive scanning method concentrates on protecting the texture information of a particular image. This combination of techniques improves the coding performance. Here entropy coding or any other complicated components are not used.

FPGA-based communication stack[4]. It is used on nano satellite space missions. This method permits the satellite operator to interact with satellite using CCSDS compliant RF link for the efficient communication. It is used for both space ground and on board communications. Here the nano satellite is incorporate with ground station provisions. Here the method is constructed with less appliance usage so it diverts most of the limited usage resources towards endeavors.

Interpolation based adaptive lifting DWT with modified SPIHT algorithm[5]. In general, DWT is adopted for fast computation and low memory requirement. But it does not concentrate on region information. It provides both geometric and spatial information which concentrate on texture information. But new technique interpolation-based adaptive lifting DWT, which more concentrates on image texture features, and modified SPIHT algorithm improves scanning process, reduces code bit length and run time.

Joint watermarking compression scheme[6]. In this scheme there is a possibility to shadow the images or to justify their reliability exactly from their compressed bit stream. It concentrates on embedded capacity and distortion. A watermarked image does not differ from their original visual which offers large capacity to provide support for various security services. This scheme is further extended for verifying the image integrity and authenticity.

Multiple transmission optimisations[7]. It is mainly used in telehealth applications especially adopted for medical images. It analyses the observed complacent of the numerous medical images and depends upon the lineament of mobile transmission systems. In multiple transmission optimisation, set of transmittal images are correlated according to the pixel resolution and are organised into arrays based on optic resemblance. After performing multiple transmission optimisation, images are reconstructed and displayed for the different users.

Visual quality evaluation method[8]. For telemedicine applications, this is a recent way for evaluating image quality and video quality. It investigates the trait of perceive decreased size logo encapsulated in an idle section of medical ultrasound frame. This method concentrates on three different metrics, peak signal to noise ratio, structure similarity index metric, differential mean opinion score and it does not need the initial stage to evaluate the aspect; it acquires huge correspondence for the different metrics used. It also improves the quality between derived logo and the original frame. It results in compressed logo data with its overhead protection.

Clustering-based compression[9]. It is adopted for the telemedicine applications and to improve the transference percentage, arcade scope and contact among medicinal team and outpatients. This method includes competitive Hopfield neural network and Modified block truncation coding. Competitive Hopfield neural network is to bring out better clustering accuracy and to beaten the defects in oscillating basic rates of clustering. Modified block truncation coding is to analyse the clustering regions with contrast compression ratio and to secure relevant image virtue data in case of small size images. This method is also recommended for the purpose of remote future responsibility coupled to cloud databases.

Novel segmentation-based compression scheme[10]. It is used for telecommunication in telemedicine applications. The main objective of this method is to upgrade the knowledge displacement and conversation between patients and medicinal workers. This method includes improved watershed transform and modified vector quantisation.

Improved watershed transform is to sector a medical image into different domains to manage valuable estimation and designation. Modified vector quantisation is to inspect the sliced regions with distinct compression rates allowing to sustain necessary lineaments and depress the image size.

COMPRESSION PROCESS – AN OVERVIEW

Nowadays image processing is widely used for the computer vision system and for other various applications such as medical field, object tracking, satellite image, etc. Satellite imaging is important and crucial field of research. Satellite images are used for weather monitoring, space information exploration, military and surveillance system. The lossy compression is used extensively in space system or multimedia application for one or more objective like reducing transmission time, reducing transmission bandwidth utilisation and reducing data rate. Satellite imaging is a powerful approach for the researchers to study about the space information, geo-science and space information exploration. Image compression is utilised to decrease the size of the information with a specific end goal to reduce memory space for information stockpiling, lessening data transfer capacity necessities for ongoing transmission. Image decompression is to give back the original image with no misfortune.

Image compression and decompression play an important role in data transmission. Image compression is one of key technologies for imaging instruments and it is the process to remove the redundant and irrelevant information from the image so that only essential information can be represented using less number of bits to reduce the storage size, transmission bandwidth and transmission time requirements. Image decompression is to decode and to reconstruct the original image. It is an application to get a much better image in terms of quality or size.

Telemedicine is the process to provide better health care for the patients at a distance. Patients who are living in remote area, they can receive medical care from doctors far or specialists far away instead of visiting them directly. Categories involved in telemedicine are store and forward, remote monitoring, real time interactive. Emerging technologies in this field are video telephony, health information technology. This type of medical care is given to the developing country where patients in remote area are more. Specialist care delivery deals with telecardiology, teletransmission, telepsychiatry, teleradiology, telepathology, teledermatology, teledentistry, teleaudiology, telephthalmology. An advanced and experimental service deals with telesurgery.

The proposed research work focuses on image compression/decompression algorithm for fast transmission of images. Efficient image compression/decompression algorithm reduces the storage size of the particular image for fast transmission. Lossless compression plays an important role in medical image transmission. Image compression/decompression is an important requirement of imaging payloads on telemedicine applications.

PROPOSED COMPRESSION STRUCTURE

Image compression is an important requirement in telemedicine and space applications. In this research work, the proposed compression/decompression algorithm transmits the images in faster manner. The proposed work is mainly useful for the people in rural areas or at distant to provide better medical care and to provide better storage capacity for spatial data. The general block of the proposed compression/decompression algorithm is given in Fig. 1.

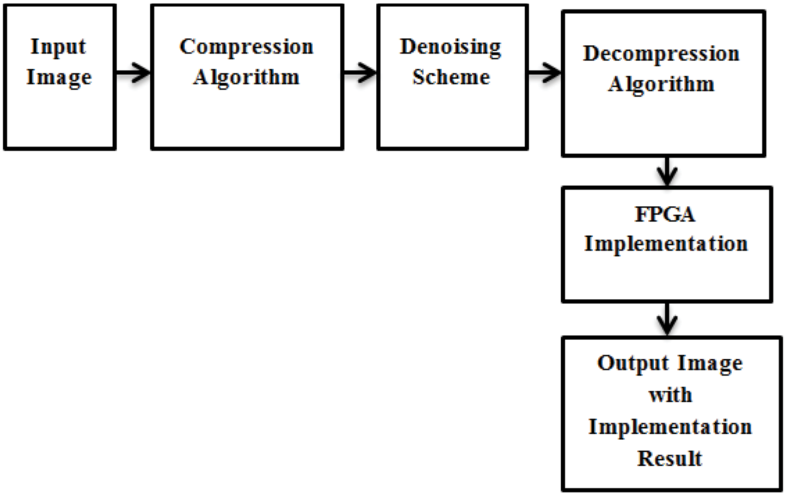

Fig. 1. Block diagram of proposed algorithm

Denoising. Denoising is a process of estimating the original data from the noisy image. Various types of noises which affect the image quality such as amplifier noise, shot noise, quantisation noise and speckle noise, etc. in medical imaging, these images are mostly affected with the speckle noise. Digital image processing techniques play a vital role in medical field. Images like computed tomography (CT), magnetic resonance imaging (MRI) and X-ray ultrasound are considered. This process improves the quality of an image by removing noise to get a better medical diagnosis.

Quality of image is a critical parameter which helps to extract the information from the medical images. By keeping this challenge in mind, the proposed denoising scheme for medical images uses suitable filter to remove noise in an image. The block diagram for denoising scheme is represented in Fig. 2.

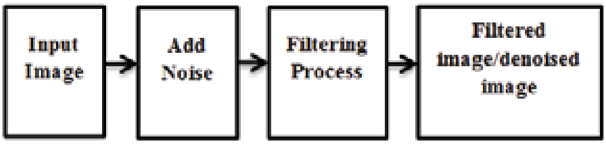

Fig. 2. Block diagram of denoising scheme

Filtering. Filtering is a technique for removing noise present in an image. Image filtering deals with different types of noises like salt and pepper noise, Gaussian and speckle noise. It mainly deals with removing other features in an image. Most commonly used filtering method is linear filtering. The equation can be written as follows:

$$g(i, j) = h(i, j) \circ f(i, j) \tag{1}$$

where $g(i, j)$ is the product of convolution $h(i, j)$ and filter (i, j) which gives clear image without noise and, i and j – the pixel values.

Image filtering deals with convolution and correlation, predefined and custom filters, linear filtering, nonlinear filtering, edge-preserving filters.

Noise measurements. The block diagram for noise measurements is represented in Fig. 3.

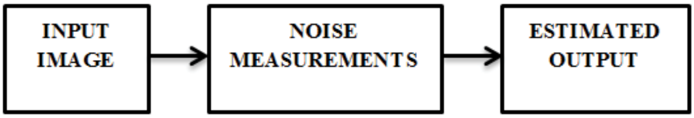

Fig. 3. Block diagram for noise measurements

FORMULAS FOR STANDARD PARAMETERS

The standard parameters which are compared for all the existing algorithms mentioned above are:

- Peak to signal noise ratio
- Signal to noise ratio
- Maximum absolute error
- Mean square error
- Compression ratio

Mean square error. It gives the error between original image and compressed image.

$$\mathrm{MSE} = \sum_{i=0}^{n} \sum_{j=0}^{n} (x'_{i,j} - x_{i,j}) \tag{2}$$

where $x_{i,j}$ is the original image pixel value; $x'_{i,j}$ – the compressed image pixel value; i, j – the row and column of an image.

Signal to noise ratio

$$\mathrm{SNR} = 10 \log \sigma^2/\sigma_e^2, \tag{3}$$

where σ^2 is the variance of desired image; σ_e^2 – the average variance.

Peak signal to noise ratio

$$\mathrm{PSNR} = 20 \log 2\mathrm{B}/\sqrt{\mathrm{MSE}} \tag{4}$$

where B is the bit depth of the original image. It gives better quality of the compressed image, if PSNR is high.

Compression ratio

$$\text{CR} = \text{uncompressed image bits/compressed image bits} \tag{5}$$

It gives information how much time image is compressed to original.

Maximum absolute error

$$\text{MAE} = \max \left| x_{i,j} - x'_{i,j} \right| \tag{6}$$

where $x_{i,j}$ is the original image pixel value; $x'_{i,j}$ – the compressed image pixel value; i, j – the row and column of an image. It gives maximum error of compressed image with original image.

Tables 1 and 2 indicate the comparison of standard parameters using various algorithms for space and telehealth applications.

Table 1. Comparison of standard parameters for space applications

Compression /decompression algorithm used	Evaluation of performance parameters					Work not discussed
	PSNR	SNR	MAE	MSE	CR	
Satellite multispectral image compression based on remote sub bands	–	–	–	–	–	regarding implementation not discussed
Remote sensing image compression based on binary tree and optimised truncation	26.61	–	–	–	–	regarding implementation not discussed
Content based on board compression for remote sensing images	–	–	–	–	–	regarding implementation not discussed
FPGA based CCSDS compliant miniaturised satellite communication stack	–	–	–	–		–
Interpolation-based direction-adaptive lifting DWT and SPIHT for image compression in multimedia communication	52.52	–	–	–		regarding implementation not discussed

Table 2. Comparison of standard parameters for telehealth applications

Compression/decompression algorithm used	Evaluation of performance parameters					Work not discussed
	PSNR	SNR	MAE	MSE	CR	
Visual quality evaluation method for telemedicine applications	0.995	–	–	–	–	regarding FPGA implementation not discussed
Clustering-based compression connected to cloud databases in telemedicine and long term care applications	25.71	–	–	–	–	regarding FPGA implementation not discussed
Multiple transmission optimisation of medical images in recourse-constraint mobile telemedicine systems	20.00	–	–	–	–	regarding FPGA implementation not discussed
Joint watermarking and lossless JPEG-LS compression for medical image security	–	–	–	–	–	regarding FPGA implementation not discussed
Segmentation-based compression: new frontiers of telemedicine in telecommunications	28.24	–	–	–	–	regarding FPGA implementation not discussed

Software tool used for image compression/decompression: MATLAB R2017a, and for hardware implementation: Xilinx FPGA Virtex version kit can be used.

CONCLUSIONS

This paper has examined various types of image compression techniques. An overview of all related image compression techniques such as DWT and Modified SPIHT algorithm, Watershed algorithm, Clustering based segmentation, Multiple transmission optimisation, Binary code truncation have been described in this paper. All these algorithms are compared with the standard parameters like PSNR, SNR, MAE, MSE, CR, RMS, CIBR and tabulated. These algorithms are mainly used in space and telehealth applications.

REFERENCES

1. A. HAGAG, E. S. HASSAN, M. AMIN, F. E. ABD El-SAMIE, XIAOPENG FAN: Satellite Multispectral Image Compression Based on Remote Sub-bands. Optic, **131**, 1023 (2017).
2. KE-KUN HUANG, HUI LU, CHUAN–XIAN REN, YU-FENG YU, ZHAO-RONG LAI: Remote Sensing Image Compression Based on Binary Tree and Optimized Truncation. Digit Signal Process, **64**, 96 (2017).
3. S. HADDAD, G. COATRIEUX, M. COZIE, D. BOUSLIMI: Joint Watermarking and Lossless JPEG – LS Compression for Medical Image Security. Elsevier Masson, RITS, 2017.

4. NAN JIANG, YI ZHUANG, DICKSON K. W. CHIU: Multiple Transmission Optimization Medical images in Recourse – Constraint Mobile Telemedicine Systems. Comput Meth Prog Bio, **145** (C), 103 (2017).
5. KARIM M. NASR, MARIA G. MARTINI: A Visual Quality Evaluation Method for Telemedicine Applications. Signal Processing: Image Communication, **57** (2017).
6. WEI – YEN HSU: Clustering-based Compression Connected to Cloud Databases in Telemedicine and Long-term Care Applications. Telematics and Informatics, **34**, 299 (2017).
7. CUIPING SHI, JUNPING ZHANG, YE ZHANG: Content-based Onboard Compression for Remote Sensing Images. NeuroComputing, **191**, 330 (2016).
8. DAVID SELEAN, GREGOR KIRBIN, IZBOK KRAMBERGES: FPGA-based CCSDS Compliant Miniaturized Satellite Communication Stack. IFAC-48-10, 028–033 (2015).
9. WEI-YEN HSU: Segmentation Based Compression: New Frontiers of Telemedicine in Telecommunication. Telematics and Informatics, **32**, 475 (2015).
10. D. BOUSLIMI, G. COATRIEUX, C. QUANTIN, F.A ALLAERT, M. COZIC, ROUXC: A Teleassistance Protocol Based on Joint Watermarking–Encryption Evidence for Identification of Liabilities in Case af Litigation. Science Direct IRBM, **36** (5), 279 (2015).

Received 5 April 2019
Revised 25 April 2019

Oxidation Communications 42, No 2, 160–168 (*2019*)

ENERGY PROCESSES BY GREENHOUSE EFFECT AND MODELLING OF TOTAL SOLAR RADIATION

Z. NIKOLAEVA

Department of Mathematics and Physics, Prof. Dr. Asen Zlatarov University,
1 Prof. Yakimov Street, 8010 Burgas, Bulgaria
E-mail: *z.v.burieva@gmail.com*

ABSTRACT

The present paper discusses the energy processes by the greenhouse effect. A theoretical equation for calculation of the total solar radiation is derived. The hourly values of the total solar radiation were calculated for four monitoring sites in the municipality of Burgas. Certain calculations were made and a regression model was developed. To estimate the quality of the two models, the coefficient of determination was used which determines the degree of linear dependence between the regressors involved in the model and the predicted values of the initial quantities. Scientific studies of this type are important for science and technologies today when solar energy as an alternative is of greatest significance for preservation of the Earth natural recourses.

Keywords: greenhouse effect, total solar radiation, regression analysis, coefficient of determination, *F*-statistics.

AIMS AND BACKGROUND

Solar radiation is an important natural factor forming the climate of the planet and affecting all living organisms and the environment. It is the main source of energy for almost all physicochemical processes taking place of the surface of the Earth and in the atmosphere[1,2]. By its passing through the atmosphere, about 35% are reflected back into space, about 23% are scattered by air molecules, particulate matter, water vapour and droplets, etc., and about 15% are absorbed by water vapour, carbon dioxide and particulate matter in the air. The rest of 27% of the solar radiation reaches Earth surface[3] and it is called direct solar radiation. This, together with the diffuse radiation reached the surface of the Earth form the total solar radiation.

Life on Earth is totally dependent on solar radiation which is the main source of energy for all natural processes. Solar radiation is basic ecologic factor which leads to extensive efforts for its study.

Greenhouse effect is a process by which the infrared radiation of some gases in the atmosphere heats Earth surface. It results in increased temperature of low atmospheric layers compared to the infrared radiation from the planet. Without this effect the average temperature would have been about –18°C (255 K) instead of the present day 15°C (288 K). This would make the existence of liquid water almost impossible (except around volcanoes) which would deprive the Earth of liquid oceans and they are the basic prerequisite for the origination and diversity of life[4].

At present, especially in Bulgaria, the efforts and activities in studies on solar radiation are concentrated mainly on accumulation and statistical processing of data from measurements. Information about the solar radiation is necessary for the design of heating domestic and cooling systems, construction of greenhouses, etc.[5]

The paper presents a modelling of the total solar radiation using simple formula of heating and taking account for the energy flows. It discusses the change of the temperature in a closed space with cubic shape, insulated and black coloured inside. The incident solar radiation is assumed to come perpendicularly to the transparent upper wall of the cube. It is assumed also that the incoming solar energy and the adjacent environment are constant. A formula describing the energy within the cube was derived. The method suggested provides possibilities for hourly calculation of the daylight values of the total solar radiation over certain region.

EXPERIMENTAL

The present paper is a continuation of our studies on the energy processes by greenhouse effect[6]. The method is used for hourly calculation of the daylight values of the total solar radiation.

The total solar radiation was modelled by a simplified formula of heating and taking into account the energy flows[6]. The temperature change in cubic formed space coloured black inside is considered. The incident sun rays are assumed to come perpendicularly to the transparent upper wall of the cube.

It is assumed also that the incoming energy flows from the sun W_{IN} and adjacent environment are constant (Fig. 1).

The denotations in Fig. 1 are as follows: 1 is transparent lid (made from glass or polymer foil); 2 is heat insulation; W_{IN} is incoming energy; W_{EMIT} is energy emitted through the wall transparent for the sun rays; W, T – energy and temperature inside the cube; W_0, T_0 – initial energy and temperature inside the cube (W_0 = min).

By reaching stationary equilibrium state, the incoming and emitted energy are equal: $W_{IN} = W_{EMIT}$. Then, the internal energy has maximum value W_{MAX}.

During the heating, if the internal energy at moment t is W, then at moment $t + \Delta t$ it will be $W + \Delta W$.

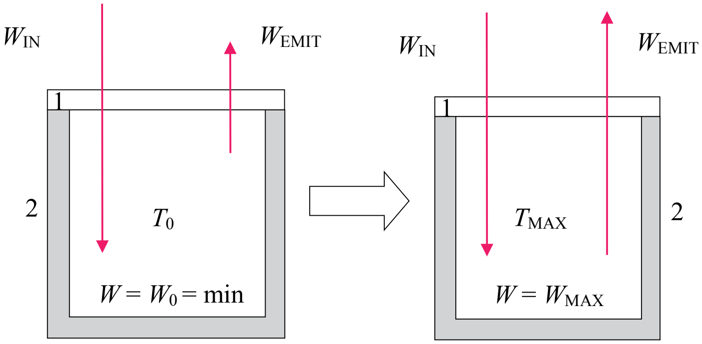

Fig. 1. Scheme of the mathematical model

The energy change is higher than zero ($dW > 0$) because a process of heating is going on. The increase of the energy at any moment is proportional to the difference between the maximum energy W_{MAX} and the energy inside the greenhouse W, as well as to the time interval (basic hypothesis for the theoretical model at first approximation):

$$dW = \mu(W_{MAX} - W)dt, \tag{1}$$

where μ is the coefficient of proportionality which depends on cube size, walls, volume, material, external temperature, etc.

After solving the differential equation (1), the following formula is obtained for the energy inside the cube:

$$W = W_{MAX} - (W_{MAX} - W_0)\, e^{-\mu t}. \tag{2}$$

A regression model was suggested by which the calculations are substantially reduced and are also suitable for studies on the hourly distribution of the total solar radiation. The regression model had the following form:

$$G = b + a_1 t + a_2 t^2 + a_3 t^3 + a_4 t^4 + a_5 t^5 + a_6 t^6, \tag{3}$$

where G is the total solar radiation per unit area per unit time, W/m^2; b, a_1, a_2, ..., a_6 – regression coefficients, t – time.

For estimation of the quality of the regression models (2) and (3), the coefficient of determination R^2 was used which determines the degree of the linear dependence between the regressors involved in the model and the predicted value of the initial quantity[7–10]. In this case, the significance of R^2 must be checked for which the Fisher criterion is usually used:

$$F = \frac{R^2}{1 - R^2} \frac{N_1 - k}{k - 1}, \tag{4}$$

where k is the number of estimated parameters of the model; N_1 – the volume of the set of experimental data. The higher the calculated value of R^2 the more reliable is the regression model.

RESULTS AND DISCUSSION

A necessary condition for the use of dependence (2) is to estimate the coefficient μ. For this purpose, data on the measured values of the total solar radiation accumulated for a period of 12 years were used[11].

According to the methods generally accepted in world practice (Klein, 1977)[11], one 'representative' day is taken for every month of the year (usually, the 15th day). The distribution of the radiation values measured at 15 min intervals for the 'representative' day is determined by taking the average of the data for the whole 12 year period of observations. This is the distribution used for the estimation of the coefficient μ for every month for certain location. This was done as follows:

For each 15 min interval of the representative day, the coefficient is calculated by the formula:

$$\mu = \frac{\ln \dfrac{G_2 - G_0}{G_2 - G_1}}{t}, \tag{5}$$

where G_2 is the value of the total solar radiation measured for the current 15 min interval, W/m^2; G_1 – the value of the total solar radiation measured for the preceding 15 min interval, W/m^2; G_0 – the lowest value of the total solar radiation for the representative day of the month, W/m^2; t – the time from the initial moment of measurement of the radiation until the current 15 min interval, h.

The average value of the coefficient μ is calculated and used in equation (2) for the specific month and specific location.

To check the accuracy of the model derived, the hourly values of the total solar radiation were calculated for four monitoring sites in the municipality of Burgas: AMS Dolno Ezerovo (European code BG0044A); AMS Meden Rudnik (European code BG0063A); OPSIS DOAS (European code BG0056A) and Mobile station.

The data source was Solar Radiation Databases[12]. The values measured were from 4.87 to 19.87 h at 0.25 h (15 min) interval.

The prediction accuracy was checked by comparing the measured and calculated by equation (2) for the monitoring sites and for every month of the year. Because of the great amount of data, the comparison was made for a 2-hour interval of the day, namely from 11.12 to 13.12 h.

For example, the results obtained from the comparison carried out for the AMS Dolno Ezerovo are presented in Table 1 where the following denotations were used: G_{calc} is the value of the total solar radiation calculated by equation (2), W/m^2; G_{meas} – the measured value of the total solar radiation, W/m^2, and ε – the relative error, %.

Table 1. Values of the total solar radiation measured by equation (2) and measured at AMS Dolno Ezerovo on monthly basis

Month	μ	Time (h)	G_{calc} (W/m^2)	$G_{meas.}$(W/m^2)	ε (%)
January	1.123378	11.12	331.686	337	–1.58
		12.12	346.157	348	–0.53
		13.12	324.410	329	–1.40
February	1.043158	11.12	429.375	435	–1.29
		12.12	445.877	448	–0.47
		13.12	422.215	427	–1.12
March	0.928605	11.12	501.428	508	–1.29
		12.12	517.149	520	–0.55
		13.12	495.407	500	–0.92
April	0.869915	11.12	589.400	595	–0.94
		12.12	604.445	607	–0.42
		13.12	582.436	587	–0.78
May	0.851073	11.12	714.893	719	–0.57
		12.12	733.138	735	–0.25
		13.12	705.528	709	–0.49
June	0.735029	11.12	707.214	714	–0.95
		12.12	726.532	730	–0.47
		13.12	698.328	704	–0.81
July	0.723815	11.12	771.864	780	–1.04
		12.12	793.834	798	–0.52
		13.12	761.193	768	–0.89
August	0.747627	11.12	795.489	808	–1.55
		12.12	821.766	828	–0.75
		13.12	783.622	794	–1.32
September	0.909868	11.12	664.349	671	–0.99
		12.12	684.186	687	–0.41
		13.12	654.634	660	–0.81
October	1.012466	11.12	507.088	513	–1.15
		12.12	524.704	527	–0.44
		13.12	499.158	504	–0.96
November	1.090676	11.12	420.547	428	–1.74
		12.12	439.318	442	–0.61
		13.12	411.924	418	–1.45
December	1.194931	11.12	328.835	334	–1.55
		12.12	343.418	345	–0.46
		13.12	322.436	327	–1.40

The analysis of the results obtained from the study showed that:

- The maximum error of prediction was observed for OPSIS DOAS and it was 1.94%;
- The average error of prediction for the individual monitoring sites was as follows:

– AMS Meden Rudnik – 0.80%;

– AMS Dolno Ezerovo – 0.91%;
– OPSIS DOAS – 0.94%;
– Mobile station – 0.92%;

● It can be seen that all the errors were negative. This was probably due to systematic error connected with the experimental study. However, it should be noted also that the error was too small to raise any concern.

Figure 2 shows graphically the change of the total solar radiation calculated for AMS Dolno Ezerovo according to the model suggested (model **(**2**)**). The period from sunrise to sunset was included and each curve corresponds to concrete month.

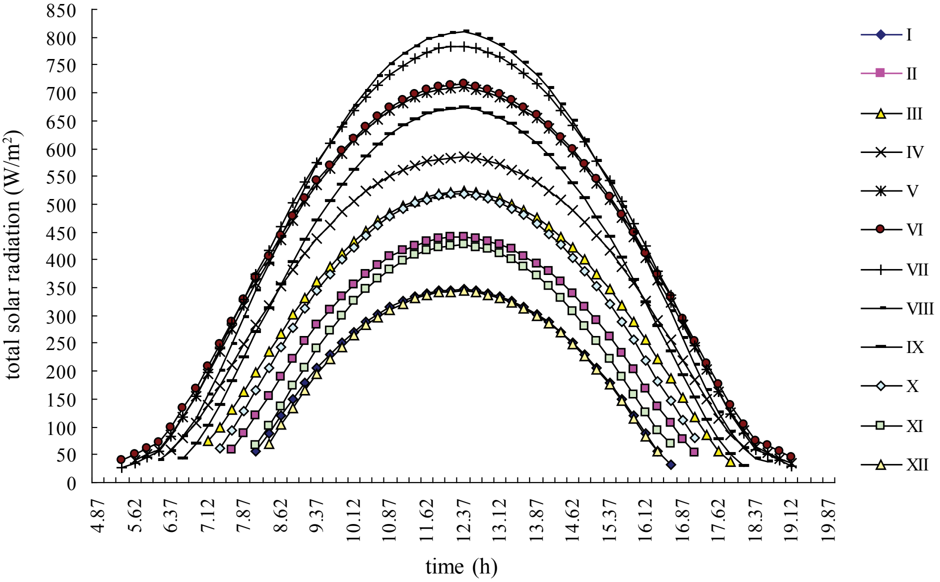

Fig. 2. Hourly values of the total solar radiation calculated on a monthly basis for AMS Dolno Ezerovo

In conclusion, the following can be stated for the model for determination of the total solar radiation suggested (model (2)):

● The model is universal;

● The model has physical sense;

● Based on a not large set of measurements, it can be adapted and used for various regions in Bulgaria and around the world;

● The accuracy of prediction of the total solar radiation is high;

● The model can be used with bigger success for more profound scientific research but it is not very convenient for everyday practical application.

Calculations were made also with the regression model derived (model 3) where the calculations are substantially reduced and it is suitable for studying the hourly distribution of the total solar radiation.

Table 2 contains the coefficients of determination obtained for models (2) and (3) by sites and months.

Figure 3 shows graphically the values of the total solar radiation calculated by models (2) and (3) for AMS Dolno Ezerovo, as example.

Table 2. Coefficients of determination R^2 for models (2) and (3) by sites and months

Month	AMS Dolno Ezerovo		AMS Meden Rudnik	
	R^2 model (2)	R^2 model (3)	R^2 model (2)	R^2 model (3)
January	0.9974	0.9976	0.9971	0.9988
February	0.9975	0.9951	0.9973	0.9951
March	0.9957	0.9967	0.9956	0.9964
April	0.9966	0.9964	0.9964	0.9964
May	0.9992	0.9968	0.9991	0.9968
June	0.9985	0.9969	0.9983	0.9969
July	0.9984	0.9973	0.9984	0.9974
August	0.9964	0.9970	0.9963	0.9970
September	0.9969	0.9965	0.9969	0.9965
October	0.9978	0.9966	0.9964	0.9966
November	0.9954	0.9968	0.9953	0.9969
December	0.9942	0.9967	0.9976	0.9964
Month	OPSIS DOAS		Mobile station	
	R^2 model (2)	R^2 model (3)	R^2 model (2)	R^2 model (3)
January	0.9970	0.9977	0.9971	0.9977
February	0.9957	0.9958	0.9958	0.9957
March	0.9955	0.9964	0.9956	0.9964
April	0.9964	0.9962	0.9964	0.9963
May	0.9992	0.9967	0.9992	0.9968
June	0.9982	0.9968	0.9983	0.9969
July	0.9984	0.9974	0.9985	0.9975
August	0.9961	0.9969	0.9962	0.9969
September	0.9968	0.9964	0.9968	0.9964
October	0.9964	0.9967	0.9964	0.9966
November	0.9952	0.9970	0.9954	0.9970
December	0.9938	0.9964	0.9975	0.9964

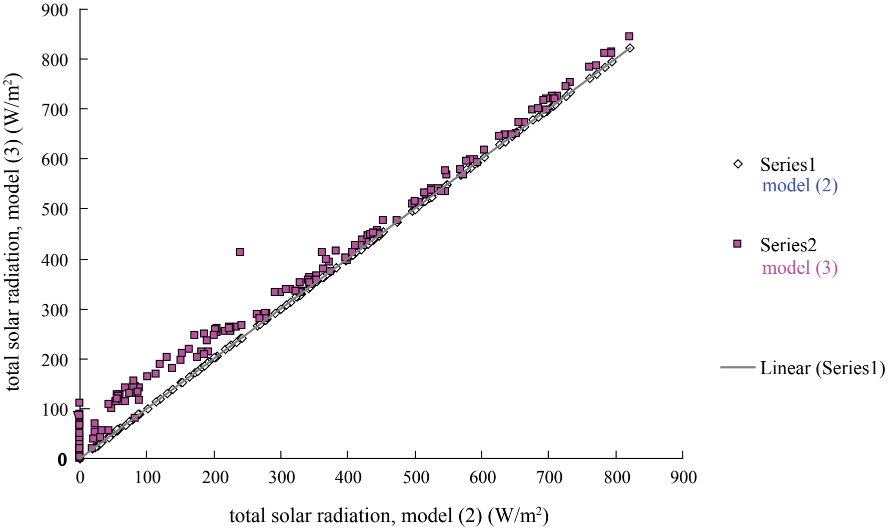

Fig. 3. Values of total solar radiation calculated by models (2) and (3) for AMS Dolno Ezerovo

It can be seen from Table 2 that the coefficients of determination for all months had values very close to unity ($R^2 > 0.99$) and Fig. 3 illustrates the very good coincidence of the predictions of the two models (2) and (3).

The calculations made using the regression model suggested are substantially reduced and they are suitable for studying the hourly distribution of the total solar radiation. The method is suitable for practical purposes (by design of solar systems, greenhouses, photovoltaics, etc.).

CONCLUSIONS

From the above results and discussion it is concluded that:

The present paper presents a theoretical equation for calculation of the total solar radiation. The hourly values of the total solar radiation were calculated for four monitoring sites in the municipality of Burgas.

The maximum error of the predictions was found to be 1.94% observed for OPSIS DOAS. The average prediction errors were: AMS Meden Rudnik – 0.80%; AMS Dolono Ezerovo – 0.91%; OPSIS DOAS – 0.94 and mobile station – 0.92. It should be noted that all the errors were negative. This was most probably due to systematic error connected with the experimental study. It must be indicated, however, that although systematic, the error was too small to raise concerns.

The theoretical model suggested is: universal; has physical sense; on the basis of not big set of data it can be adapted and used for different regions in Bulgaria and around the world; the accuracy of the prediction of the total solar radiation is high; the model could be used mostly for detailed scientific research but it is not convenient for every day practical purposes.

Calculations were made also using the regression model derived by which the calculations were substantially eased and are more suitable for studies on the hourly distribution of the total solar radiation. A check was made to find whether the simplified model (3) retains the quality of model (2). Obviously, the coefficients of determination for all the months had values close to unity which indicates that the method can be used to calculate the total solar radiation over the municipality of Burgas.

The calculations required by the regression model suggested are considerably reduced and they are suitable for studies on the hourly distribution of the total solar radiation. The method is practically convenient (for the design of solar systems, greenhouses, photovoltaics, etc.).

REFERENCES

1. A. DIMOV, P. TOROMANOVA: Introduction to the Chemical and Metallurgical Technology and Ecology. Technics, Sofia, 1998.
2. W. ZDUNKOWSKI, W.-G. PANHANS, R. WELCH, G. KORB: A Radiation Scheme for Circulation and Climate Models. Beitr Phys Atmos, **55**, 215 (1982).
3. National Inventary Report 2013 for Greenhouse Gas Emissions, Submission under UNFCCC and the Kyoto Protocol, April 2013.
4. V. ALEXANDROV, P. SIMEONOV, V. KAZANDZHIEV, G. KORCHEV, A. YOTOVA: Climate Change. NIMH – BAS, Sofia, 2010.
5. V. ALEXANDROV, M. SCHNEIDER, E. KOLEVA, J. MOISSELIN: Climate Variability and Change in Bulgaria during the 20th Century. Journal Theoretical and Applied Climatology, **79**, 133 (2003).
6. Z. NIKOLAEVA, G. BAIKUSHEVA – DIMITROVA, G. VISOKOV: Investigation of the Energy Processes in the Greenhouse Effect. Oxid Commun, **35** (2), 516 (2012).
7. N. LJUBOJEV, J. VESELINOVIC, M. DUKIC – MIJATOVIC: Protection of the Quality of Air in the Legislation of the Republic of Serbia as a Process of Harmonization with the EU Legislation. Oxid Commun, **36** (4), 1217 (2013).
8. A. SENTURK: Investigating the Weight of Variables Causing Air Pollution through Factor Analysis. Oxid Commun, **37** (3), 817 (2014).
9. G. BAIKUSHEVA-DIMITROVA: Calculation and Prognosis of the Thermodynamic Properties of Rare Earth Tellurites of the $Ln_2Te_4O_{11}$ Type. Oxid Commun, **35** (3), 776 (2012).
10. Z. IVANOV, A. GEORGIEVA, K. PANAYOTOVA: Determination of Interphase Surface by Rectification Process in a Laboratory Column. Oxid Commun, **41** (3), 365 (2018).
11. S. KLEIN: Calculation of Monthly Average Insulation on Tilted Surfaces. Journal of Solar Energy, **19**, 325 (1977).
12. Solar Radiation Databases. (2012) www.photovoltaic-software.com/solar-irradiation-database.php.

Received 5 March 2019
Revised 19 April 2019

Oxidation Communications 42, No 2, 169–176 (2019)

Methods for spectroscopic investigations of oxy-reduction processes

SPECTROPHOTOMETRIC DETERMINATION OF 5-AMINOSALICYLIC ACID IN PHARMACEUTICAL SAMPLES

CHAND PASHA

Department of General Studies (Chemistry), Yanbu Industrial College, Royal Commission Yanbu Colleges and Institues (RCYCI), Royal Commission for Jubail and Yanbu, P.O. Box 30436, 21 477 Yanbu, Kingdom of Saudi Arabia
E-mail: *drcpasha@gmail.com*

ABSTRACT

An easy and specific method for the spectrophotometric quantitative analysis of 5-aminosalicylic acid is described. This method is based on the reaction of 5-aminosalicylic acid with nitrite in acidic standard to form diazonium ion, which is coupled with thymol in basic standard to produce azo dyes, which shows absorption maxima at 470 nm. The Beer law obeys in the concentration range of 0.5–11.2 $\mu g\ ml^{-1}$ of 5-aminosalicylic acid with thymol. The molar absorptivity of 5-aminosalicylic acid-thymol azo dye is $2.672 \times 10^4\ l\ mol^{-1}\ cm^{-1}$ and Sandell sensitivity of 5-aminosalicylic acid-thymol azo dye is $5.731 \times 10^{-3}\ \mu g\ cm^{-2}$, respectively. The dye formed is stable for 10 h. The optimum reaction circumstances and other analytical critical parameters are evaluated. Interference due to foreign organic compounds has been investigated. The method has been effectively applied to the determination of 5-aminosalicylic acid in pharmaceutical samples.

Keywords: spectrophotometry, diazotisation, 5-aminosalicylic acid, nitrite, thymol.

AIMS AND BACKGROUND

5-aminosalicylic acid (5-ASA), also known as mesalazine/mesalamine is an aminosalicylate and non-steroid anti inflammatory drug. It is used to heal inflamatory bowel ailment, ulcerative colitis/inflamed anus/rectum, and to sustain remission in the Crohn disease[1–7], and as a rectal suppository[8] and an enema for the lower bowel conditions[8]. It is generic and sold worldwide with the brand names Azacol, Lialda, pentasa and apriso[9].

5-aminosalicylic acid is the moiety of sulphasalazine, which is processed to sulphapyridine and 5-aminosalicylic acid[10]. Mesalamine is obtained by bacterial action in the colon[11]. Mucosal formation of arachidonic acid metabolites and is increased in patients with inflammatory bowel disease and it is possible that mesalamine diminishes inflammation by blocking cyclo-oxygenase in the colon[12]. 5-aminosalicylic acid is a potent scrounger of reactive O_2 species in the pathogenesis of inflammatory bowel ailment, inhibition of natural killer cell activity and impairment of neutrophil function[13,14]. It is the active component of the prodrug balsalazide along with the inert carter molecule 4-aminobenzoyl-beta-alanine[15]. Many types of formulations are available for the 5-aminosalicylic acid[16].

Literature survey shows that there are various methods for the determination of 5-aminosalicylic acid in pharmaceutical samples including potentiometry[17], differential pulse voltammetry[18], coulometry[19], fluorimetry[20], chromatography[21–25], micellar electrokinetic chromatography[26], fluorescence[24], liquid chromatography[27], HPLC (Refs 28 and 29), HPLC with electrochemical detections[30], mass spectrometry[31,32], charge transfer complex formation[33,34], oxidative coupling[35,36], Schiff base[37,38] and oxidation-reduction reactions[39], and UV-spectrophotometry[40–49].

Some of the above methods need high complex instruments, expensive chemicals and reagents, acquired multi-manipulated steps and many derivatisation reactions[17–20,26–28]. Chromatographic procedures have been used and recommended[21–25]. Nevertheless these methods required complex and expensive equipment, labour intensive sample preparation procedures. Spectrophotometric methods are the often used technique because of the low cost instruments, sensitivity, simplicity and their availability. However, these methods[40–49] presented for the determination of 5-aminosalicylic acid in their pharmaceutical dosage were linked with some major shortcomings, such as dreary extraction methods, time consumption, lack of sensitivity, heating problems and cooling effects. The current paper describes a simple spectrophotometric analysis of 5-aminosalicylic acid in pharmaceutical samples which is free from all of the above-mentioned drawbacks.

EXPERIMENTAL

A SHIMADZU Deutschland GmbH UV-2550 spectrophotometer and a pH meter-WTW pH 330 were used.

MATERIALS AND REAGENTS

Stock standard solution of 5-aminosalicylic acid (*gift sample from Matrix Laboratory, Hyderabad, India*). An amount of 0.102 g 5-aminosalicylic acid was weighed and dissolved in distilled water, then transferred into a 100 ml standard flask fulfilled to the mark with double distilled water (1000 μg ml^{-1}). Working solution was prepared as required by dilution.

Sodium nitrite solution (*0.5%*). Dissolved 0.5 g of sodium nitrite in 100 ml distilled water in a volumetric flask.

Hydrochloric acid solution (*0.5 M*). Diluted 4.25 ml of the concentrated acid to 100 ml volumetric flask with distilled water.

Thymol solution (*1%*). Dissolved ≈ 1g of thymol in 100 ml distilled water.

Sodium hydroxide solution (*2M*). Dissolved ≈ 8 g of NaOH in 100 ml distilled water in a volumetric flask and kept in a plastic bottle.

Pharmaceutical preparations of 5-aminosalicylic acid. Pharmaceutical preparations were obtained from commercial sources: Walasa, 400 mg (Wallace Pharmaceuticals Limited, Goa), Asacol, 400 mg (Win Medicare, New Delhi), Mesacol, 400 mg (Sun Pharma Limited Sikkim), Salofalk GR, 250 mg (German remedies, Mumbai) and Pentasa formulations, 500 mg (Ferring Pharmaceuticals Private Limited, Mumbai).

Procedure for assay of pharmaceutical preparations. Tablets solution (100 µg ml^{-1}): Weighed an amount of 5 samples (≈ 100 mg each) of 5-aminosalicylic acid, dissolved with 10 ml absolute ethanol and diluted with 40 ml distilled water, mixed well and filtered. The solutions were diluted to 100 ml with water.

Procedure for determination of 5-aminosalicylic acid. An aliquot of the solution containing 5-aminosalicylic acid (µg ml^{-1}) was transferred into a string of 10 ml calibrated flasks. Add 1 ml of 0.5% solution of $NaNO_2$ and 0.5 ml of 0.5 M HCl and then the solution was mixed thoroughly and kept away for accomplishment of diazotisation reaction. Then, add 1 ml of 1% thymol and 1.5 ml of 2 M NaOH solutions and then diluted to 10 ml, using distilled water and mixed thoroughly. Later the absorbance of the coloured azo dye formed was measured at 470 nm beside the reagent blank.

RESULTS AND DISCUSSION

The method involves the diazotisation of 5-aminosalicylic acid with nitrite, followed by the coupling of thymol in alkaline standard. The absorption spectra of the azo dye obtained from 5-aminosalicylic acid and thymol are presented in Fig. 1, having absorption maximum at 470 nm respectively and the reaction method is shown in Scheme 1.

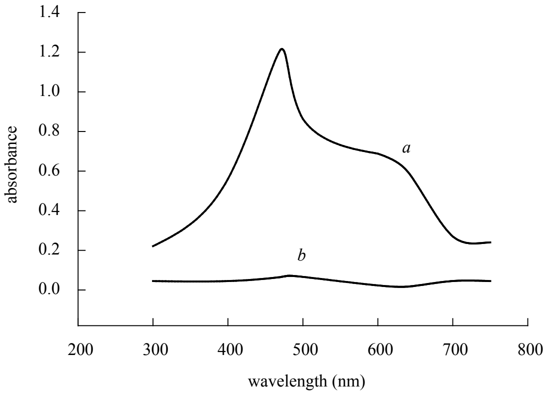

Fig. 1. Absorption spectra of: diazocouple of nitrite with thymol against reagent blank – *a* and reagent blank against distilled water – *b*

Scheme 1

5-aminosalicylic acid using diazocouple of nitrite and thymol

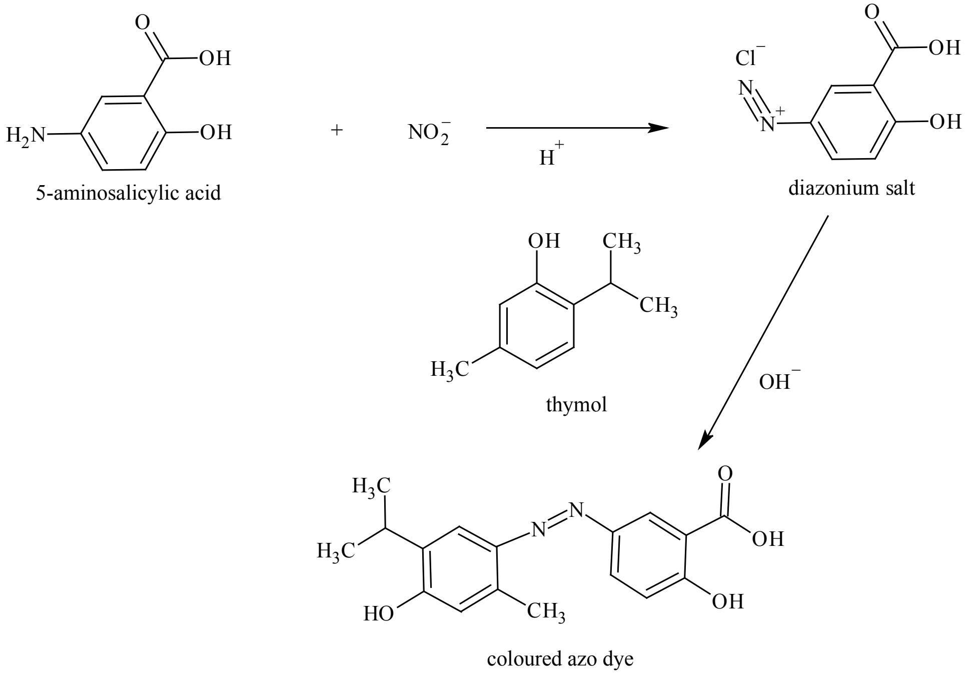

Effect of acid concentration, acids and temperature. The acidity effect on the diazotisation reaction was considered with 2 μg ml^{-1} of 5-aminosalicylic acid, in the range 0.1–0.5 M HCl. From the results, it can be observed that 0.5 ml of 0.5 M HCl is the suitable concentration which gives the highest value of absorbance. Beyond this range, a decrease in the absorbance was detected.

The effect of the amount of different acids (weak and strong) on the diazotisation of 5-aminosalicylic acid has been investigated. The results indicated that 0.5 ml of 0.5 M HCl produced the highest intensity for the dye, so it has been selected in the subsequent experiments. Diazotisation was conceded at room temperature (25 ± 5°C).

Effect of nitrite concentration. The colour reached maximum intensity when using 1 ml of 0.5% sodium nitrite solution using the current procedure with 2 μg ml^{-1} of 5-aminosalicylic acid and adding 1 ml of 0.1–1.0% solutions of the nitrite in hydrochloric acid (0.5 M) to a series of nitrite solutions. Higher concentration did not build up the absorbance further, and at lower concentration, no good results were obtain.

Effect of coupling agent. Thymol is used as a coupling agent was in the current procedure, by taking 2 μg ml^{-1} of 5-aminosalicylic acid and adding 0.25–2.0 ml of 1% thymol to a string of nitrite solutions. It was found that utmost and firm colour was obtained with 1 ml of thymol (1%) solution in an ultimate volume of 10 ml.

Effect of NaOH concentration. The experiment showed that 1.5 ml of NaOH gave utmost absorbance and 1.5 ml of 2 M NaOH solutions was preferred for the procedure using 2 μg ml^{-1} of 5-aminosalicylic acid. Other alkaline solutions were applied, but the best results were gained by the use of NaOH solution.

Interference of foreign compounds. The results specified that the studied foreign compounds do not interfere in the determination of 2 μg ml^{-1} of 5-aminosalicylic acid. The error was below ± 2% error in the absorbance values of 5-aminosalicylic acid at 2 μg ml^{-1}.

Analytical data. By plotting absorbance against concentration of 5-aminosalicylic acid, a straight line is obtained in the graph. The Beer law obeys in the range of 0.5–11.2 μg ml^{-1} for 5-aminosalicylic acid with thymol. The molar absorptivity of coloured system with nitrite-thymol was 2.672×10^4 l mol^{-1} cm^{-1} and the Sandell sensitivity of coloured system with nitrite-thymol was found to be 5.731×10^{-3} μg cm^{-2}. The detection limit ($D_L = 3.3\ \sigma/S$) was found 0.190 μg ml^{-1}, quantitation limit ($Q_L = 10\ \sigma/S$) was 0.578 μg ml^{-1} (where σ = standard deviation ($n = 5$) and S = slope of the curve) and the correlation coefficient was 0.9996.

Applications. The current scheme was useful for the determination of 5-aminosalicylic acid in pharmaceuticals samples. The outcomes were compared with the reference method[38,49] (Table 1). The outcomes by *t* and *F*-tests illustrated no major distinction in precision and accuracy. The additional ingredients present in pharmaceutical sample appearances did form not hinder.

Table 1. Determination of 5-aminosalicylic acid in different pharmaceutical samples using diazocouple of nitrite with thymol

Pharmaceuticals samples	Sample taken (μg ml^{-1})	Proposed method		Reference method[44,55]	*t*-test[b]	*F*-test[c]
		sample found ±SD[a] (μg ml^{-1})	recovery (%)	recovery (%) ± SD[a]		
Walasa	5.0	5.02 ± 0.544	100.40	–	–	–
(400 mg/tab)	10.0	9.98 ± 0.564	99.80	–	–	–
Asacol	5.0	5.01 ± 0.670	100.20	100.19 ± 0.651	0.024	1.06
(400 mg/tab)	10.0	10.02 ± 0.654	102.00	–	–	–
Mesacol	5.0	4.97 ± 0.742	99.40	98.52 ± 0.712	0.065	1.09
(400 mg/tab)	10.0	9.96 ± 0.731	99.60	98.90 ± –	–	–
Salofalk GR	5.0	5.02 ± 0.632	100.40	100.31 ± 0.594	0.051	1.13
(250 mg/tab)	10.0	10.01 ± 0.694	100.10	99.86 ± –	–	–
Pentasa	5.0	5.03 ± 0.774	100.60	97.80 ± –	–	–
(500 mg/tab)	10.0	10.00± 0.736	100.00	103.30 ± –	–	–

[a] – Mean ($n = 5$) ± SD (standard deviation); [b] *t*-value (8 degree of freedom at P (0.95) = 2.306); [c] *F*-value ((4,4) degree of freedom at P (0.95) = 6.39).

CONCLUSIONS

The current method is easy, simple and common foreign compounds such as glucose, lactose, starch and urea do not interfere. The current reaction technique has an ample range with no need of heating, cooling and extraction. Also the method have the benefit of low absorbance, high sensitivity and the technique does not fabricate any rigorous reaction circumstances and have high colour stability (more than 24 h). The current method is more effective than the techniques reported in literature and it has been effectively applied for the spectrophotometric analysis of 5-aminosalicylic acid in several pharmaceutical dosage samples.

ACKNOWLEDGEMENTS

Author is thankful to the Department of General Studies, Yanbu Industrial College and RCYCI, KSA, for the constant support and encouragement.

REFERENCES

1. W. J. SANDBORN, B. G. FEAGAN, G. R. LICHTENSTEIN: Medical Management of Mild to Moderate Crohn’s Disease: Evidence-based Treatment Algorithms for Induction and Maintenance of Remission. Alimentary Pharmacology & Therapeutics, **26** (7), 987 (2017).
2. G. C. ACTIS, R. PELLICANO, M. RIZZETTO, M. AYOUBI, N. LEONE: Individually Administered or Co-prescribed Thiopurines and Mesalamines for Inflammatory Bowel Disease. World J Gastroenterol, **15**, 1420 (2009).
3. S. HANAUER, J. SCHWARTZ, M. ROBINSON, W. ROUFAIL, S. ARORA, S. J. CELLO, M. SAFDI: Mesalamine Capsules for Treatment of Active Ulcerative Colitis: Results of a Controlled Trial. Pentasa Study Group. Am J Gastroenterol, **88**, 1188 (1993).
4. E. GONSALVES, L. M. ALMEIDA, T. C. DINIS: Antioxidant Activity of 5-Aminosalicylic Acid against Peroxidation of Phosphatidylcholine Liposomes in the Presence of Alpha-Tocopherol. Free Radic Res, **29** (1), 53 (1998).
5. C. A. SNINSKY, D. H. CORT, F. SHANAHAN, B. J. POWERS, J. T. SESSIONS, R. E. PRUITT, W. H. JACOBS, S. K. LO, S. R. TARGAN, J. J. CERDA: Oral Mesalamine (Asacol) for Mildly to Moderately Active Ulcerative Colitis. A Multicenter Study. Ann Intern Med, **115**, 350 (1991).
6. S. BONDESEN, J. HEGNHOJ, F. LARSEN, S. H. HANSEN, C. P. HANSEN, S. N. RASMUSSEN: Pharmacokinetics of 5-Aminosalicylic Acid in Man Following Administration of Intravenous Bolus and Per Os Slow-Release Formulation. Dig Dis Sci, **36**, 1735 (1991).
7. A. B. R. THOMSON: New Developments in the Use of 5-Aminosalicylic Acid in Patients with Inflammatory Bowel Disease. Aliment Pharmacol Ther, **5**, 449 (1991).
8. UK, Electronic Medicines Compendium Suppository Label, 2016: UK Enema Label, January 2016**.**
9. Drugs International Trade Names for 5-Aminosalicylic Acid, April 20, 2016**.**
10. FINKEL, CUBEDDU, CLARK: Lipp Illustr Rev Pharm, 4th ed. 2009.
11. H. SCOTT, N. W. RICH, B. ATHOS, Z. ANNA, M. RIE, B. PETER, M. FREDERICK, R. SARATHCHANDRA, B. ROBERT, F. SONIA: 5-Aminosalicylate Therapy Is Associated with Higher 6-Thioguanine Levels in Adults and Children with Inflammatory Bowel Disease in Remission on 6-Mercaptopurine or Azathioprine. Inflamm Bowel Dis, 12, 251 (2006).
12. R. E. SMALL, C. C. SCHRAA: Chemistry, Pharmacology, Pharmacokinetics, and Clinical Applications of Mesalamine for the Treatment of Inflammatory Bowel Disease. Pharmacotherapy, 14, 385 (1994).

13. L. R. SUTHERLAND, G. R. MAY, E. A. SHAFFER: Sulfasalazine Revisited: a Meta-Analysis of 5-Aminosalicylic Acid in the Treatment of Ulcerative Colitis. Ann Intern Med, 118, 540 (1993).
14. G. PALUMBO, G. CARLUCCI, P. MAZZEO: Simultaneous Determination of 5-Aminosalicylic Acid, Acetyl-5-aminosalicylic Acid and 2,5-Dihydroxybenzoic Acid in Endoscopie Intestinal Biopsy Samples in Humans by High-performance Liquid Chromatography with Electrochemical Detection. J Pharm Biomed Anal Oxford, **14**, 175 (1995).
15. Drugs & Therapy Properties, **19**, 10 (2003).
16. B. YE, D. R. van LANGENBERG: 5-Aminosalicylic Acid Preparations for the Treatment of Ulcerative Colitis: Are All Created Equal. World J Gastrointest Pharmacol Ther, **6** (4), 137 (2015).
17. J. A. RAFAEL, J. R. JABOR, R. CASAGRANDE, S. R. GEORGETTI, M. F. BORIN, M. J. V. FONSECA: Validation of HPLC, DPPH and Nitrosation Methods for Mesalamine Determination in Pharmaceutical Dosage Forms. Rev Bras Cienc Farm, **43**, 97 (2007).
18. B. NIGOVIC, B. SIMUNIC: Determination of 5-Aminosalicylic Acid in Pharmaceutical Formulation by Differential Pulse Voltammetry. J Pharm Biomed Anal, **31**, 169 (2003).
19. I. F. AHDULLIN, N. N. CHERNYSHEVA, G. K. BUDNIKOV: Galvanostatic Coulometric Determination of Salicylic Acid and Some of Its Derivatives Using Electrogenerated Halogens. J Anal Chem, **57**, 721 (2002).
20. H. A. ZADEH, S. KOHANSAL: Determination of Mesalamine by Spectrofluorometry in Human Serum after Solid-phase Extraction with Ni-Al Layered Double Hydroxide as a Nanosorbent. J Braz Chem Soc, **23**, 473 (2012).
21. S. NANDIPATI, V. K. REDDY, S. UBA: A Validated Ultra Performance Liquid Chromatography Method for Assay Determination of Mesalamine. Int J Pharmacy Pharm Sci, **5**, 312 (2013).
22. C. GANDINI, G. CACCIALANZA, M. KITSOS, G. MASSOLINI: Determination of 5-Aminosalicylic Acid and Related Compounds in Raw Materials and Pharmaceutical Dosage Forms by High-performance Liquid Chromatography. J Chromatogr A, **540**, 416 (1991).
23. C. AGUZZI, P. CAPRA, C. BONFERONI, P. CEREZO, I. SALCEDO, R. SÁNCHEZ, C. CARAMELLA, C. VISERAS: Chitosan–Silicate Biocomposites to Be Used in Modified Drug Release of 5-Aminosalicylic Acid. Appl Clay Sci, **50**, 106 (2010).
24. F. N. HUSSAIN, R. A. AJJAN, M. MOUSTAFA, J. C. ANDERSON, S. A. RILEY: Simple Method for the Determination of 5-Aminosalicylic and N-acetyl-5-aminosalicylic Acid in Rectal Tissue Biopsies. J Chromatogr B, Biomed Sci Appl, **716** (1), 257 (1998).
25. B. BYSTROWSKA, J. NOWAK, J. BRANDYS: Validation of a LC Method for the Determination of 5-Aminosalicylic Acid and Its Metabolite in Plasma and Urine. J Pharm Biomed Anal, **22**, 341 (2000).
26. R. GOTTI, R. POMPONIO, C. BERTUCCI, V. CAVRINI: Determination of 5-Aminosalicylic Acid-related Impurities by Micellar Electrokinetic Chromatography with an Ion-Pair Reagent. J Chromatogr A, **916**, 175 (2001).
27. P. W. HANEY, A. K. DASH: Simple Liquid Chromatographic Method for the Analysis of 5-Aminosalicyclic Acid and its Degradation Product. J Chromatogr A, **765**, 233 (1997).
28. V. DARAK, A. B. KARADI, S. A. RAJU, M. D. ARSHAD, A. L. GANURE: Development and Validation of HPLC Method for Determination of Mesalamine in Tablet Dosage Forms. Pharma Sci Monitor, **3** (1), 74 (2012).
29. M. NOBILIS, Z. VYBIRALOVA, K. SLADKOVA, M. LISA, M. HOLCAPEK: High Performance Liquid-chromatographic Determination of 5-Aminosalicylic Acid and Its Metabolites in Blood Plasma. J Chromatogr A, **1119**, 299 (2006).
30. G. PALUMBO, S. BACCHI, L. PRIMAVERA, P. PALUMBO, G. CARLUCCI: A Validated HPLC Method with Electrochemical Detection for Simultaneous Assay of 5-Aminosalicylic Acid and Its Metabolite in Human Plasma. Biomed Chromatogr, **19**, 350 (2005).
31. M. ORIOLI, C. MARINELLO, R. COZZI, L. P. PIODI, M. CARINI: LC-MS/MS and Ft-Ir Analyses of Stones from a Patient with Crohn's Disease: a Case Report. J Pharm Biomed Anal, **35**, 1263 (2004).
32. E. PASTORINI, M. LOCATELLI, P. SIMONI, G. RODA, E. RODA, A. RODA: Development and Validation of a HPLC-ESI-MS/MS Method for the Determination of 5-Aminosalicylic Acid and Its

Major Metabolite N-Acetyl-5-Aminosalicylic Acid in Human Plasma. J Chromatogr B, Anal Tech Biomed Life Sci, **872**, 99 (2008).

33. M. S. AL-ENIZZI, T. N. Al-SABHA, T. S. Al-GHABSHA: Use of Charge Transfer Complex Formation Reaction in Spectrophotometric Microdetermination of Some Drugs. Jordan J Chem, **7** (1), 87 (2012).
34. T. N. Al-SABHA, M. S. Al-ENIZZI, O. A. Al-TAEE: Application of Chloranil and Fluoranil Π-Acceptors for the Spectrophotometric Determination of Mesalamine in Pharmaceutical Bulk and Dosage Forms. Eur Chem Bull, **3** (5), 377 (2014).
35. I. A. SHIHAB: Spectrophotometric Determination of Mesalazine via Oxidative Coupling Reaction. Tikrit J Pure Sci, **16** (4), 64 (2011).
36. S. SHAKEELA, B. S. RAM, C. B. SEKARAN: Application of Horseradish Peroxidase Mediated Oxidative Coupling Reaction for the Determination of Mesalazine. Chiang Mai J Sci, **38**, 551 (2011).
37. N. S. SAMA, B. M. GURUPADAYYA, A. KUMAR: Spectrophotometric Determination of Mesalamine by PDAC and NQS Reagents in Bulk and Tablet Dosage Form. J Pharm Res, **4**, 39 (2011).
38. B. S. CHANDRA, S. S. BHOGELA, M. SHAIK, C. S. VADLAMUDI, M. CHAPPA, N. S. MADDIRALA: Simple and Sensitive Spectrophotometric Methods for the Analysis of Mesalamine in Bulk and Tablet Dosage Forms. Quim Nova, **34**, 1068 (2011).
39. S. RAO, NARALA, K. SARASWATHI: Three Simple and Sensitive Spectrophotometric Methods for Quantitative Determination of Mesalamine in Bulk and Tablet Dosage Forms. Int J Res Pharm Biomed Sci, **1**, 10 (2010).
40. S. K. LOVRIC, B. NIGOVI: Identification of 5-Aminosalicylic Acid, Ciprofloxacin and Azithromycin by Abrasive Stripping Voltammetry. J Pharm Biomed Anal, **36**, 81 (2004).
41. S. K. ACHARJYA, A. SAHU, S. DAS, P. SAGAR, M. M. ANNAPURNA: Development and Validation of Spectrophotometric Methods for the Estimation of Mesalamine in Pharmaceutical Preparations. J Pharm Educ Res, **11**, 63 (2010).
42. V. DARAK, A. B. KARADI, M. D. ARSHAD, R. S. APPAL: Derivative Spectroscopic Determination of Mesalamine in Tablets Dosage Forms. Pharm Sci Monitor, **2**, 31 (2011).
43. V. MADHAVI, V. PANCHAKSHARI, T. N. PRATHYUSHA, C. B. SEKARAN: Spectrophotometric Determination of Mesalamine in Bulk and Tablet Dosage Forms Based on Diaz-coupling Reaction with Resorcinol. Int J Pharm Sci Rev Res, 105 (2011).
44. A. K. MOHARANA, M. BANERJEE, S. PANDA, J. N. MUDULI: Development and Validation of UV Spectrophotometric Method for the Determination of Mesalamine in Bulk and Tablet Formulation. Int J Pharmacy Pharm Sci, **3**, 19 (2011).
45. M. ROHITAS, A. AGRAWAL, A. K. JAIN, N. K. LARIYA, A. K. KHARYA: Development of Simultaneous Spectrophotometric Method of 5-Aminosalicylic Acid and Prednisolone in Same Dosage Form. Int J Appl Pharm, **2**, 8 (2010).
46. S. RAKESH KUMAR, P. PANKAJ SINGH, G. PRAGYA: UV Spectrophotometric Method for the Estimation of Mesalazine in Bulk and its Pharmaceutical Dosage Forms. Int J Pharm Sci Res, **1**, 44 (2010).
47. A. RAWA, J. ZAKARIA: Spectrophotometric Determination of Mesalazine by Diazotisation Coupling Method with Resorcinol. J Raf Sci, **20** (1), 90 (2009).
48. A. A. FATIMA, ABDALLA, A. A. ELBASHIR: Development and Validation of Spectrophotometric Methods for the Determination of Mesalazine in Pharmaceutical Formulation. Med Chem, **4** (3), 361 (2014).
49. T. N. Al-SABHA, N. N. HABEEB: Spectrophotometric Determination of Mesalamine Using Sodium Nitroprusside as Chromogenic Reagent. Eur Chem Bull, **4** (8), 384 (2015).

Received 24 February 2019
Revised 17 March 2019

Oxidation Communications 42, No 2, 177–184 (2019)

SPECTROPHOTOMETRIC DETERMINATION OF HEXAVALENT CHROMIUM IN ENVIRONMENTAL SAMPLES

K. STANCHEVA[a]*, C. PASHA[b]

[a]*Department of Inorganic and Analytical Chemistry, 'Prof. Dr. Asen Zlatarov' University, 8010 Burgas, Bulgaria*
[b]*Department of General Studies, Yanbu Industrial College, P. O. Box 30436, 21 477 Yanbu, Kingdom of Saudi Arabia*
E-mail: *krasimiraangelova@abv.bg*

ABSTRACT

In this work a spectrophotometric determination of hexavalent chromium in various environmental samples is presented. The method is based on two successive chemical reactions – an oxidation of iodide ions to iodine from chromium(VI) and an interaction of the liberated iodine with organic dye fuchsine in acid media. The light absorption is maximum at λ_{max} 355 nm. Under the optimum conditions the calibration curve is obtained in the linear range of 0.5–5.0 mg l^{-1}. The molar apsorptivity, detection limit and limit of quantification are found to be: 4.8×10^4 l mol^{-1} cm^{-1}, 0.031 µg ml^{-1} and 0.096 µg ml^{-1}. The method is free from common interferences and is successfully applied for the determination of chromium(VI) in drinking, lake, sea water and sea salt .

Keywords: spectrophotometry, chromium(VI) determination, fuchsine, environmental samples.

AIMS AND BACKGROUND

The content of hexavalent chromium in environmental samples is under control throughout the world. Cr(VI) is highly toxic and known human carcinogen and mutagen[1–3]. The compounds of chromium(VI) in the environment are distributed as a result of industrial pollution. Trace element exists as a raw material crocoite $PbCrO_4$ mainly used for the steel and cement productions. Industries dealing with paints, pigments, dyes, textile, leather, etc. are also an important source of discharge of chromium(VI) in the environment. Since the European Community has established rules for implementing the restrictions on the amount of toxic metals, thus monitoring

---

[*] For correspondence.

of chromium(VI) is of great importance for the preservation of human health and to ensure minimum environmental impact.

There is an increasing interest to develop sensitive analytical procedures for the determination of trace amounts of chromium(VI). Several analytical instrumental techniques can be employed, such as ICP-MS (Refs 4 and 5), HPLC (Ref. 6), X-ray absorption spectroscopy[7], complexometry[8], voltammetry[9] and UV-vis. spectrophotometry[10–12].

UV-vis. spectrophotometry is the most important method for the quantitative analysis of trace ions in environmental, industrial and biological samples. Among the instrumental analytical techniques, spectrophotometric techniques are precise and occupy an unique position because of its simplicity, sensitivity, accuracy and rapidity[13]. In comparison with atomic emission spectroscopy, atomic absorption spectroscopy and similar techniques, it offers the advantage of having calibration graphs that are linear over a wider range. Another benefit is the time and the cost of analyses.

A survey of literature revealed that a large number of reagents are suitable for the spectrophotometric determination of chromium such as methylene blue[14], N-*m*-tolyl-*p*-methoxybenzohydroxamic acid[15], leuco Xylene cyanol FF (Ref. 16), iodnitrotetrazolium chloride[17], trifluoperazine hydrochloride[18], saccharin[19], variamine blue[20] and azure B (Ref. 21). Resently a simple, rapid, selective and sensitive spectrophotometric method was reported for the micro determination of chromium(VI) using fuchsine as new reagent[22].

This study is important for regular monitoring of toxic Cr(VI) concentrations in environmental samples.

EXPERIMENTAL

Instrumentation. A Thermo Scientific UV-Visible Double Beem Spectrophotometer equipped with 1-cm short path length quartz cells was used for absorbance measurements of the solutions. The pH was measured using an Expert 001, model 3 (0.1) pH meter/potentiometer (Ekoniks-Expert RF) with glass electrode.

Reagents and solutions. All chemicals (Merck, Germany, purity >99 %) were of analytical-reagent grade and employed without further purification. Distilled water was used in the preparation of the various solutions.

Proposed methods. Standard chromium(VI) stock solution of 1 g l^{-1} was prepared from dried $K_2Cr_2O_7$ (Sigma Aldrich, ≥99% purity) and the working solutions were diluted as needed. Hydrochloric acid (2M), potassium iodide (2%), acetate buffer solution of pH 4; 0.05% fuchsine ($C_{20}H_{20}N_3 \cdot HCl$, 4-[(4-aminophenyl)-(4-imino-1-cyclohexa-2,5-dienylidene)methyl]aniline hydrochloride, M = 337.86 g mol^{-1}), aqua solutions were also used.

ANALYTICAL PROCEDURES AND CALIBRATION GRAPH

Construction of calibration graph. Working standards were prepared daily from the stock solution. Into a series of 100-ml calibrated flasks aliquots of standard solutions equivalent to 0.5–5.0 μg ml^{-1} of chromium(VI) were transferred. Potassium iodide (1 ml), then hydrochloric acid (1 ml) were added and the mixture was gently shaken until the appearance of yellow colour indicating the liberation of iodine. Then, 0.5 ml fuchsine was added to it, followed by the addition of 2 ml of acetate buffer (pH = 4) solution. The contents were diluted to the mark with distilled water and mixed well. After 15–30 min the absorbance of the coloured species was measured at 355 nm against the reagent blank. Blank was prepared with the same reagents, but without addition of Cr(VI) solution and fuchsine. The absorbance-calibration curve was plotted with a correlation coefficient of 0.9973.

Determination of chromium(*VI*) *in water samples*. Each filtered environmental water samples were analysed for chromium (VI). All the tested samples gave negative results. To these samples known amounts (2.0–4.0 μg ml^{-1} of chromium(VI)) were spiked and analysed for chromium(VI) by the proposed method and by the reference diphenylcarbazide metrod.

Determination of chromium(*VI*) *in sea water and salt*. The decomposition was carried out by the mineralisation method to wet salts. Sample preparation of seawater and lye involved incinerating the residue in a muffle furnace at a temperature of about 400° C for 30–40 min. Sea salt samples were dried at 110°C, tempered in a desiccator and the exact mass was dissolved in an accurate volume of distilled water. The concentrations of all samples prepared were 1 g l^{-1}.

Suitable aliquot of this solution was transferred to a 100-ml calibrated flask and known amount of Cr(VI) was added. The absorptions were measured and chromium(VI) concentrations were determined.

RESULTS AND DISCUSSION

This study was carried out in order to establish the most favourable conditions for the complex formation for the spectrophotometric method of the reagents with iodine, to achieve maximum colour development, good linearity over the working concentration range, sensitivity, selectivity, accuracy and precision and finally analytical applications.

The organic reagents with high molecular weights as fuchsine furnish maximum sensitivity[23,24]. The technique emploed to increase the detection limit is to use indirect determinations[22–25], where a stoichiometric gain in the number of chromophores may result or the newly formed chromophore may have a higher molar absorptivity. The methodology chosen for the analysis had a goal to achieve relative standard deviations in concentrations as low as about 0.5–2.0%. This enables the determination of microquantities of components.

Absorption spectra. The method proposed is based on the reaction of chromium(VI) with potassium iodide in acid medium to liberate iodine which is equivalent of Cr(VI) concentration. The liberated iodine bleaches the colour of the fuchsine. The liberated iodine oxidises the indicators to yellow-brown colour at maximum absorption at 355 nm for Cr(VI)-fuchsine system, which is probably due to a formation of complexes. The absorption spectra of Cr(VI)-fuchsine system is presented in Fig. 1 and the reactions of iodine with fuchsine is presented in Fig. 2.

Adherence of the Beer law. Varying the concentrations of the reagents a straight line graph was obtained in the linear range of 0.5–5.0 mg l^{-1}. The molar apsorptivity was found to be: 4.8 × 10^{4} l mol^{-1} cm^{-1}.

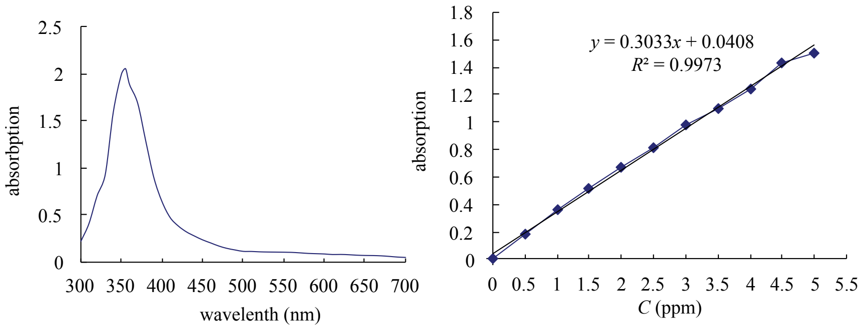

Fig. 1. Absorption spectra of Cr(VI)-fuchsine system (λ_{max} 355 nm) and calibration curve

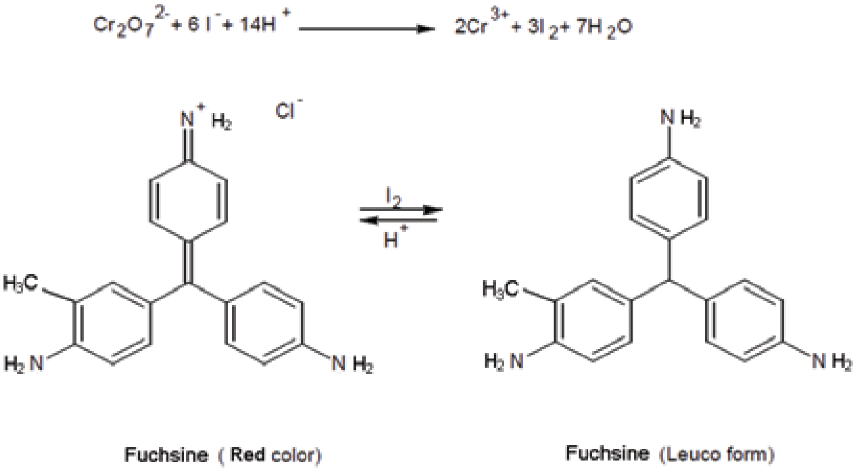

$$Cr_2O_7^{2-} + 6I^- + 14H^+ \longrightarrow 2Cr^{3+} + 3I_2 + 7H_2O$$

Fig. 2. Reaction scheme of $K_2Cr_2O_7$ with iodide and of fuchsine–iodine system

A calibration equation derived from a calibration curve was plotted from standards for the quantitation of Cr(VI) in the samples. However, due to the low sensitivity to low Cr(VI) concentration and/or no Cr(VI) in the samples it was not colour developed on complexation with fuchsine in the samples. Therefore, a standard addition method was employed for Cr(VI) determination. Thus, all samples were spiked with 2 ppm and 4 ppm Cr(VI) standard.

Effect of reagent concentration. The effect of acidity and reagent concentrations was investigated in order to find the optimum reaction conditions. The liberation of iodine from KI in an acid medium is quantitative. The appearance of yellow colour indicates the liberation of iodine and it oxidises indicators to yellow coloured species. It was found that 1 ml of each 2% KI and 2M HCl are sufficient for the liberation of iodine from iodide by chromium(VI) and 0.5 ml of 0.05% fuchsine is sufficient for the decolourisation reaction. The bleached reaction system was found to be stable for more than 1 h for chromium-fuchsine system.

Limit of detection (*LOD*) *and limit of quantitation* (*LOQ*). Based on the standard deviation of the blank samples and the slope of the calibration curve, molar absorptivity, detection limit and quantitation limit for chromium-fuchsine system are found to be 4.8×10^4 l mol^{-1} cm^{-1}, 0.031 µg ml^{-1}, and 0.096 µg ml^{-1}.

LOD may be expressed as: $\text{LOD} = 3.3\ \sigma/S$; (Ref. 26), LOQ may be expressed as: $\text{LOQ} = 10\ \sigma/S$; (Ref. 27), where σ is the standard deviation of the reagent blank and S – the slope of the calibration curve.

Effect of interfering species. The effect of various of ions at microgram levels on the determination of chromium(VI) was examined. The tolerance limits of interfering species are established at those concentration that do not cause more than ± 2% error in absorbance values of chromium with fixed concentration. The results are shown in Table 1.

Table 1. Effect of diverse ions on the determination of Cr(VI) using fuchsine as reagent

Foreign ion	Tolerance limit (mg l^{-1})
Oxalate, tartrate, acetate, citrate	>2000
Ba^{2+}, Cd^{2+}, Ca^{2+}, Ni^{2+}	1000
Mg^{2+}, Mn^{2+}, Al^{3+}	1000
EDTA	>1500
Na^+, Cl^-	800

Applications. The proposed method has the advantage of simplicity, sensitivity, rapidity and will compete with most of the spectrophotometric methods available in the literature. Accurate and reproducible results are obtained with permissible standard deviation. The precision and accuracy of the method is studied by analysing the sample solution containing known amounts of the cited reagents within the Beer law limit. The low values of the relative standard deviation in percentages indicates the high accuracy of the methods. The proposed method is applied to the determination of Cr(VI) in water samples and sea salt (Tables 2 and 3).

Table 2. Determination of hexavalent chromium in water samples

Samples	Chromium added (mg l^{-1})	Standard method		Proposed method	
		Cr(VI) found $\bar{x} \pm tS/\sqrt{n}$ (mg l^{-1})	RSD $S_r = (S/\bar{x}) \times 100$ (%)	Cr(VI) found $\bar{x} \pm tS/\sqrt{n}$ (mg l^{-1})	RSD $S_r = (S/\bar{x}) \times 100$ (%)
Lake water	2.0	1.960 ± 0.03	1.35	1.960 ± 0.04	1.82
	4.0	3.960 ± 0.04	0.74	3.950 ± 0.04	0.81
Tap water	2.0	1.952 ± 0.036	1.47	1.956 ± 0.039	1.60
	4.0	3.968 ± 0.032	0.65	3.970 ± 0.029	0.59
Mineral water	2.0	1.966 ± 0.033	1.37	1.958 ± 0.037	1.55
	4.0	3.986 ± 0.020	0.29	3.966 ± 0.033	0.68

Table 3. Determination of hexavalent chromium in sea water and sea salt

Samples	Chromium added (mg l^{-1})	Standard method		Proposed method	
		Cr(VI) found $\bar{x} \pm tS/\sqrt{n}$ (mg l^{-1})	RSD $S_r = (S/\bar{x}) \times 100$ (%)	Cr(VI) found $\bar{x} \pm tS/\sqrt{n}$ (mg l^{-1})	RSD $S_r = (S/\bar{x}) \times 100$ (%)
Sea water	2.0	1.96 ± 0.04	0.95	1.95 ± 0.05	2.13
	4.0	3.95 ± 0.05	1.02	3.95 ± 0.04	1.12
Sea salt	2.0	1.95 ± 0.04	1.83	1.94 ± 0.05	2.26
	4.0	3.94 ± 0.05	0.99	3.95 ± 0.05	1.16

Number of determination $n = 5$; t – Students t-value at 95% probability; S – standard deviation; $\bar{x}$, an average.

The Cr(VI) concentrations found meet the proposed lower limits (20 ng l^{-1}) in tap water set by the Office of Environmental Health Hazard Assessment (OEHHA) (Ref. 29) as a public health goal for chromate.

CONCLUSIONS

Simple, sensitive and rapid, spectrophotometric method was developed for the spectrophotometric determination of hexavalent chromium using fuchsine as new reagent. The proposed method is based on the use of nontoxic solvent that makes analysis friendly both for the operator and the environment. The determination is indirect and is based on the reaction of Cr(VI) with potassium iodide in acid medium to liberate iodine. The liberated iodine bleaches the magenta red colour of the fuchsine and has an absorption maximum at λ_{max} 355 nm. The method has good precision and accuracy and offer advantages of using water as solvent and high colour stability in comparison with standard diphenylcarbazide method (30 min). The proposed method can be used as alternative method to the reported ones for the routine determination of Cr(VI) in environmental samples.

REFERENCES

1. D. R. LIDE: CRS Hand Book of Chemistry and Physics. 74 ed, SRS Press USA, 1998.

2. D. G. BARCELOUX, D. BARCELOUX: Chromium. Toxicology, **37** (2), 173 (1999).
3. A. D. DAYAN, A. J. PAINE: Mechanisms of Chromium Toxicity, Carcinogenicity and Allergenicity: Review of the Literature from 1985 to 2000. Human and Experimental Toxicology, **20** (9), 439 (1999).
4. C. F. WANG, C. J. CHIN, S. K. LUO, L. C. MEN: Determination of Chromium in Airborne Particulate Matter by High Resolution and Laser Ablation Inductively Coupled Plasma Mass Spectrometry. Anal Chim Acta, **389**, 257 (1999).
5. H. GURLEY, D. WALLSCHLAEGER: Determination of Chromium(III) and Chromium(VI) Using Suppressed Ion Chromatography Inductively Coupled Plasma Mass Spectrometry. J Anal Atom Spectrum, **16**, 926 (2001).
6. A. IMRAN, Y. A. HASSAN: Speciation of Arsenic and Chromium Metal ions by Reversed Phase High Performance Liquid Chromatography. Chemosphere, **48**, 275 (2002).
7. R. E. SHAFFER, J. O. CROSS, S. L. ROSE-PEHRSSON, W. T. ELAM: Speciation of Chromium in Simulated Soil Samples Using X-ray Absorption Spectroscopy and Multivariate Calibration. Anal Chim Acta, **442**, 295 (2001).
8. G. H. JEFFERY, J. BASSETT, J. MENDHAM, R. C. DENNEY, A. I. VOGEL: Textbook of Quantitative Inorganic Analysis. 5th ed. Longmans, 1989.
9. N. J. S. FURTADOA, EMANUEL A. O. FARIASB, C. EIRASC, J. L. MAGALHÃESA, J. B. SILVAD: Electrochemical Behaviors of Alizarin and Cr(VI)–Alizarin Complex Adsorbed on Edge-Plane Pyrolytic Graphite Electrode. Surfaces and Interfaces, **14**, 238 (2019).
10. S. BALASUBRAMANIAN, V. PUGALENTHI: Determination of Total Chromium in Tannery Waste Water by Inductively Coupled Plasma-atomic Emission Spectrometry, Flame Atomic Absorption Spectrometry and UV–visible Spectrophotometric Methods. Talanta, **50**, 457 (1999).
11. M. I. C. MONTEIRO, I. C. S. FRAGA, A. V. YALLOUZ, N. M. M. OLIVEIRA, S. H. RIBEIRO: Determination of Total Chromium Traces in Tannery Effluents by Electrothermal Atomic Absorption Spectrometry, Flame Atomic Absorption Spectrometry and UV-vis. Spectrophotometric Methods. Talanta, **58,** 629 (2002).
12. K. K. ONCHOKE, S. A. SASU: Determination of Hexavalent Chromium (Cr(VI)) Concentrations via Ion Chromatography and UV-Vis Spectrophotometry in Samples Collected from Nacogdoches Wastewater Treatment Plant, East Texas (USA). Advances in Environmental Chem, 1 (2016).
13. Z. MARCZENKO: Separation and Spectrophotometric Determination of Elements. John Wiley and Sons, New York, 1986.
14. M. KAMBUROVA: Spectrophotometric Determination of Chromium (VI) with Methylene Blue. Talanta, **40**, 713 (1993).
15. S. B. GHOLSE, B. K. DESHMUKH, P. J. ANOLCAR: Extractive Micro Determination of Chromium (VI) with N-*m*-tolyl-*p*-methoxy Benzohydroxamic acid. J Indian Chem Soc, **61**, 465 (1984).
16. H. D. REVANASIDDAPPA, T. N. KIRAN KUMAR: A Highly Sensitive Spectrophotometric Determination of Chromium Using Leuco Xylene cyanol FF. Talanta, **60**, 1 (2003).
17. M. KAMBUROVA: Iodnitrotetrazolium Chloride-A New Analytical Reagent for Determination of Chromium. Talanta, **40**, 725 (1993).
18. H. D. REVANASIDDAPPA, T. N. KIRAN KUMAR: Rapid Spectrophotometric Determination of Chromium with Trifluoperazine Hydrochloride. Chem Anal (Warsaw), **47**, 311 (2002).
19. T. CHERIAN, B. NARAYANA: Spectrophotometric Determination of Chromium Using Saccharin. Indian J Chem Technol, **12**, 596 (2005).
20. B. NARAYANA, T. CHERIAN: Rapid Spectrophotometric Determination of Trace Amounts of Chromium Using Variamine Blue as a Chromogenic Reagent. J Braz Chem Soc, **16**, 197 (2005).
21. B. NARAYANA, T. CHERIAN: Spectrophotometric Determination of Trace Amounts of Chromium by the Oxidation of Azure B. Oxid Commun, **28**, 923 (2005).
22. K. A. STANCHEVA, C. PASHA: Spectrophotometric Determinations of Trace Amounts Chromium(VI) Using Crystal Violet and Fuchsine as New Reagents. Oxid Commun, **37**, 836 (2014).

23. K. A. STANCHEVA, C. PASHA: Spectrophotometric Determinations of Trace Amounts Vanadium(V) Using Safranine O and Fuchsine as New Reagents. Oxid Commun, **38**, 2113 (2015).
24. K. A. STANCHEVA, C. PASHA: Spectrophotometric Determinations of Trace Amounts Arsenic(III) and Arsenic(V) Using Safranine O and Fuchsine as New Reagents. Oxid Commun, **39**, 1538 (2016).
25. C. PASHA, B. NARAYANA, K. STANCHEVA: Selenium Determination in Environmental and Pharmaceutical Samples by New Spectrophotometic Method. Oxid Commun, **40** (1-I), 292 (2017).
26. J. M. GREEN: A Practical Guide to Analytical Method Validation. Anal Chem News and Features, 305A (1996).
27. J. VESSELMAN: Selectivity or Specificity? Validation of Analytical Methods from the Perspective of an Analytical Chemist in the Pharmaceutical Industry. J Pharm Biomed Anal, **14**, 867 (1996).
28. California Office of Environmental Health Hazard Assessment (OEHHA): Announcement of Second Public Comment Period Draft Technical Support Document on Proposed Public Health Goal for Hexavalent Chromium in Drinking Water. 2011.

Received 11 March 2019
Revised 27 March 2019

Oxidation Communications 42, No 2, 185–193 (2019)

Methods for investigation of biological products

ORDINARY LEAST SQUARES LINEAR REGRESSION MODEL FOR ESTIMATION OF COPPER IN WILD EDIBLE MUSHROOMS

L. DOSPATLIEV[a]*, M. IVANOVA[b]

[a]*Department of Pharmacology, Animal Physiology and Physiological Chemistry, Faculty of Veterinary Medicine, Trakia University, Stara Zagora, Bulgaria*
E-mail: *lkd@abv.bg*
[b]*Department of Informatics and Mathematics, Faculty of Economics, Trakia University, Stara Zagora, Bulgaria*

ABSTRACT

This study examines the dependence of Cu on Fe, Zn, Mn, Co, Cd and Pb, using data on trace elements content in the wild edible mushroom *Suillus luteus* growing in the Batak Mountain, Bulgaria. Quantitative determination of the concentration of the studied trace elements was carried out in mineralised samples by Perkin Elmer AAnalyst 800 atomic absorption spectrometer with deuterium background corrector. All statistical computing, analysis and all charts were performed with the statistical software R program. We received an ordinary least squares multiple linear regression model showed that: if Fe, Co and Cd increase by 1%, the effect of this increase would result in an increase in Cu by 5.08% on the average; if Zn, Mn and Pb decrease by 1%, the effect of this decrease would result in an decrease in Cu by 0.29% on the average.

Keywords: atomic absorption spectrometry, trace elements, linear regression model, ordinary least squares, *Suillus luteus.*

AIMS AND BACKGROUND

Mushrooms have a distinct group of living organisms of considerable nutritive, harmaceutical and ecological value. They play a vital role in most of the ecosystems in the biosphere because they are able to biodegrade the substrate on which they grow. Fruit bodies of mushrooms are appreciated for their chemical[1–3] and nutritional properties[4–8] and also for texture and flavour. It is commonly known that mushrooms are source of micro- and macroelements[9–13]. The content of metallic elements in many mushroom species is considerably higher[14–21] than in fruits and vegetables[22].

---

[*] For correspondence.

Copper is an essential metal for normal plant growth and development, although it is also potentially toxic. For humans copper is an essential nutrient that plays a role in the production of hemoglobin (the main component of red blood cells), myelin (the substance that surrounds nerve fibres), collagen (a key component of bones and connective tissue), and melanin (a dark pigment that colours the hair and skin). The RDA (Recommended dietary allowance) for copper – is 900 μg a day for both men and women[2].

The aims of this article were to determine trace elements (Pb, Cd, Co, Cu, Mn, Zn and Fe) contents in wild edible mushroom *Suillus luteus* growing in the Batak Mountain, Bulgaria and to identify the relationship between Cu and the other elements using ordinary least squares multiple linear regression model.

EXPERIMENTAL

DATA DESCRIPTION

Plant material. Mushroom samples were collected in 2018 from the Batak Mountain, Bulgaria by the authors themselves. The Batak Mountain is located in western Rhodopes. Its western border is defined by the Chepinska river, the southern border – by Dospatska river and Dospat dam, the eastern border – by Vacha river and the northern border – by the Thracian Plane (GPS41°46′02.6″N 24°08′48.4″E). The region is industry-free and is characterised with forests, land and low buildings.

Chemical analysis methods. Quantitative determination of the concentration of the studied trace elements (Pb, Cd, Co, Cu, Mn, Zn and Fe) was carried out in the mineralised samples by Perkin Elmer AAnalyst 800 atomic absorption spectrometer with deuterium background corrector.

Digestion procedures. Multiwave 3000 closed vessel microwave system (maximum power was 1400 W, and the maximum pressure in Teflon vessels – 40 bar) was used in this study. Mushroom samples (0.25 g) were digested with 6 mL of HNO_3 (65%) and 1 ml of H_2O_2 (30%) in microwave digestion system for 23 min and diluted to 25 ml with deionised water. A blank digest was carried out in the same way. All sample solutions were clear.

STATISTICAL ANALYSIS

Statistical software. All statistical computing, analysis and all charts were performed with the Statistical software R program version 3.5.1.

Statistical tests. The Shapiro–Wilk test is a test for normal distribution exhibiting high power, leading to good results even with a small number of observations. In contrast to other comparison tests the Shapiro–Wilk test is only applicable to check for normality. The null-hypothesis (H_0): the population is normally distributed. The test statistic is[23]:

$$W = \frac{\left(\sum_{i=2}^{n} a_i y_i\right)^2}{\sum_{i=1}^{n} \left(x_i - \overline{y}\right)^2},$$

where n is the number of observations; y_i – the values of the ordered sample, and a_i – the tabulated coefficient.

The Durbin–Watson test statistic tests the null hypothesis that the residuals from an ordinary leastsquares regression are not autocorrelated. The Durbin–Watson statistic ranges in value from 0 to 4. A value near 2 indicates non-autocorrelation; a value toward 0 indicates positive autocorrelation; a value toward 4 indicates negative autocorrelation. The test statistic is[24]:

$$d = \frac{\sum_{t=2}^{n} \left(e_t - e_{t-1}\right)^2}{\sum_{t=1}^{n} e_t^2},$$

where e_t is the residual residual associated with the observation at time t and n – the number of observations.

Because of the dependence of any computed Durbin-Watson value on the associated data matrix, exact critical values of the Durbin–Watson statistic are not tabulated for all possible cases. Instead, Durbin and Watson established upper (DU) and lower bounds (DL) for the critical values. Typically, tabulated bounds are used to test the hypothesis of zero autocorrelation against the alternative of positive first-order autocorrelation, since positive autocorrelation is seen much more frequently in practice than negative autocorrelation[25].

The F-test for linear regression tests whether any of the independent variables in a multiple linear regression model are significant. The formula for F-test statistic is:

$$F = \frac{\text{explained variance}}{\text{unexplained variance}}.$$

F-test is greater as:

– distance between groups is greater or dispersion media groups around the general average is greater;

– groups are more homogeneous or error represented by scattering within the groups is less.

Thus, relatively high F values are strong arguments against H_0 (null hypothesis). P-value is the probability of obtaining a value of F which is at least as great as that observed by us if H_0 were true. Therefore, the smaller the p-value the lower chance that H_0 fair. For p-value < 0.05 to reject H_0 the following condition is necessary:

$$F_{\text{calculat}} > F_{\text{tabular}}$$
$$(F_{\text{calculated}} > F_{\text{tatbular}}).$$

Variance inflation factors (VIF) measure how much the variance of the estimated regression coefficients is inflated as compared to when the predictor variables are not linearly related. If VIF > 10 there is an indication for multicollinearity to be present[26].

Model specification. In econometrics, ordinary least squares (OLS) method is widely used to estimate the parameter of a linear regression model. OLS estimators minimise the sum of the squared errors (a difference between observed values and predicted values). The OLS estimator is consistent when the regressors are exogenous, and optimal in the class of linear unbiased estimators when the errors are homoscedastic and serially uncorrelated. Under these conditions, the method of OLS provides minimum-variance mean-unbiased estimation when the errors have finite variances. Under the additional assumption that the errors are normally distributed, OLS is the maximum likelihood estimator.

In this article OLS multiple linear regression model was used to identify the dependences of trace elements in wild edible mushroom *Suillus luteus*. The long-run functions are specified as follows:

$$\mathrm{Cu} = f(\mathrm{Fe}, \mathrm{Zn}, \mathrm{Mn}, \mathrm{Co}, \mathrm{Cd}, \mathrm{Pb}).$$

From the point of view of multiple linear regression, the constructed model must satisfy the following assumptions: linear relationship, multivariate normality, no or little multicollinearity, no autocorrelation and homoscedasticity[26].

RESULTS AND DISCUSSION

Concentrations of seven trace elements (Pb, Cd, Co, Cu, Mn, Zn and Fe) have been determined in this study. The trace element contents of the species depend on the ability of the species to extract elements from the substrate, and on the selective uptake and deposition of elements in tissues. The results obtained, in the current study, indicated that Pb, Cd, Co, Cu, Mn, Zn and Fe content of the investigated mushroom samples were found to be comparable with those reported in the literature (Table 1) (Refs 11–21). The averages of Pb, Cd, Co, Cu, Mn, Zn and Fe present in the studied wild mushrooms were far below the limit sets by the WHO (Ref. 27). Descriptive statistics was used to make a preliminary analysis of the database (Table 1). It was concluded that data were fairly symmetrical because the skewness was between –0.5 and 0.5, except Fe and Cu which were negatively skewed (skewness between –1 and –0.5). Co and Fe can be considered homogeneous data. From the Shapiro-Wilk Test, the p-value > 0.05 suggested that the distribution of the data was not significantly different from normal distribution. In other words, normality could be assumed.

Table 1. Descriptive statistics of the results for Pb, Cd, Co, Cu, Mn, Zn and Fe concentrations (mg kg^{-1}, dry weight basis) in *Suillus luteus* mushroom (n = 15)

Statistical index	Element						
	Pb	Cd	Co	Cu	Mn	Zn	Fe
Mean	7.957	0.973	1.032	6.121	14.457	78.563	84.947
Std. error	0.379	0.027	0.022	0.486	0.437	1.088	1.818
Median	7.910	0.950	1.028	6.751	14.084	77.901	86.844
Std. dev.	1.468	0.106	0.083	1.881	1.692	4.215	7.040
Variance	2.155	0.011	0.007	3.537	2.863	17.769	49.566
Kurtosis	–1.148	–0.817	–1.227	–0.580	–1.213	–0.918	–0.341
Skewness	0.015	0.245	–0.389	–0.574	0.034	0.398	–0.778
Range	4.851	0.361	0.237	5.858	5.232	12.057	22.030
Minimum	5.545	0.788	0.889	3.032	11.624	73.156	71.963
Maximum	10.396	1.150	1.126	8.890	16.856	85.213	93.993
Sum	119.357	14.589	15.483	91.819	216.854	1178.452	1274.216
Count	15.000	15.000	15.000	15.000	15.000	15.000	15.000
Conf. level (95.0%)	0.813	0.059	0.046	1.041	0.937	2.334	3.899
Homo-geneous coeff. (%)	18.450	10.905	8.069	30.723	11.705	5.366	8.288
Shapiro-Wilk Test	0.950	0.949	0.892	0.897	0.938	0.912	0.896
p-Value	0.532	0.518	0.072	0.085	0.359	0.144	0.0813

Ordinary least squares linear regression model for Cu. In an explicit and multiple linear regression form, the functions of Cu can be stated as:

$$\text{Cu} = a_0 + a_1\text{Fe} + a_2\text{Zn} + a_3\text{Mn} + a_4\text{Co} + a_5\text{Cd} + a_6\text{Pb}.$$

Table 2. Components of the ordinary least squares multiple linear regression model

Coefficient	Estimate	Std. error	t value	p-value (> $\|t\|$)
a_0	–29.441	23.0874	–1.275	0.238
a_1	0.555	0.3254	1.707	0.126
a_2	–0.226	0.218	–1.037	0.330
a_3	–0.484	0.578	–0.838	0.427
a_4	1.623	7.058	0.230	0.824
a_5	13.070	12.949	1.009	0.342
a_6	–0.160	0.438	–0.365	0.724
Multiple R-squared	0.537	F-statistic		15.481 (p-value = 1.902e^{-04})
Adjusted R-squared	0.190	Durbin-Watson stat.		1.962 (p-value = 0.0106)
Residual standard error	1.692			

For multiple linear regression modelling of the variables included in this study factor Cu we considered as a resultant factor and Fe, Zn, Mn, Co, Cd and Pb: as independent factors (Table 2). The regression analysis of the model highlighted the fact that the relation between dependent and independent factors was strong (Table 2): the correlation coefficient was $R = 0.733$ and the determination coefficient (R-squared) was 0.537 or roughly 54% of the variance found in the response variable (Cu) can be explained by predictor variables. The constructed model satisfy the assumptions of multiple linear regression: the Durbin-Watson test indicated non-autocorrelation (test statistic value was near 2, then the null hypothesis was not rejected); the calculated values of the Fisher F-test of the multiple regression model indicated the relevance of the model ($F = 15.481$, p-value $= 1.902\mathrm{e}^{-04}$); tabular value given by test was 4.48 for a probability of 0.05 (Ref. 28), which means that the resulting equation was: $F_{\text{calculated}} > F_{\text{tabular}}$, consequently the null hypothesis (H_0) was rejected and the variances included in the study differed significantly between them; the VIF values for the explanatory variables Fe, Zn, Mn, Co, Cd and Pb were: 5.657, 4.116, 4.675, 1.689, 9.220 and 2.023, respectively – the model is free from multicollinearity.

Thus, we have the following equation for the dependent variable Cu:

$$\mathrm{Cu} = -29.441 + 0.555\mathrm{Fe} - 0.226\mathrm{Zn} - 0.484\mathrm{Mn} + 1.623\mathrm{Co} + 13.070\mathrm{Cd} - 0.160\mathrm{Pb}.$$

According to the above equation, a direct influence, increasing the resultant factor Cu, was foud out for the factors Fe, Co and Cd. Classification ranges given by model coefficients are presented in Table 3. Calculations were performed with a probability of 90% and respectively 95%. Zn and Mn variables ranges were relevant in both cases of the evaluation.

Table 3. Coefficient confidence intervals

Coefficient	Estimate	90%		95%	
		lower	upper	lower	upper
a_0	–29.441	–72.373	13.492	–82.680	23.799
a_1	0.555	–0.049	1.161	–0.195	1.306
a_2	–0.226	–0.631	0.179	–0.728	0.276
a_3	–0.484	–1.559	0.591	–1.817	0.849
a_4	1.623	–11.502	14.747	–14.653	17.898
a_5	13.070	–11.009	37.150	–16.791	42.931
a_6	–0.160	–0.975	0.655	–1.170	0.850

Figure 1 depicts graphically the validity of regressors, i.e. variable plots and plots of residuals versus each regressor.

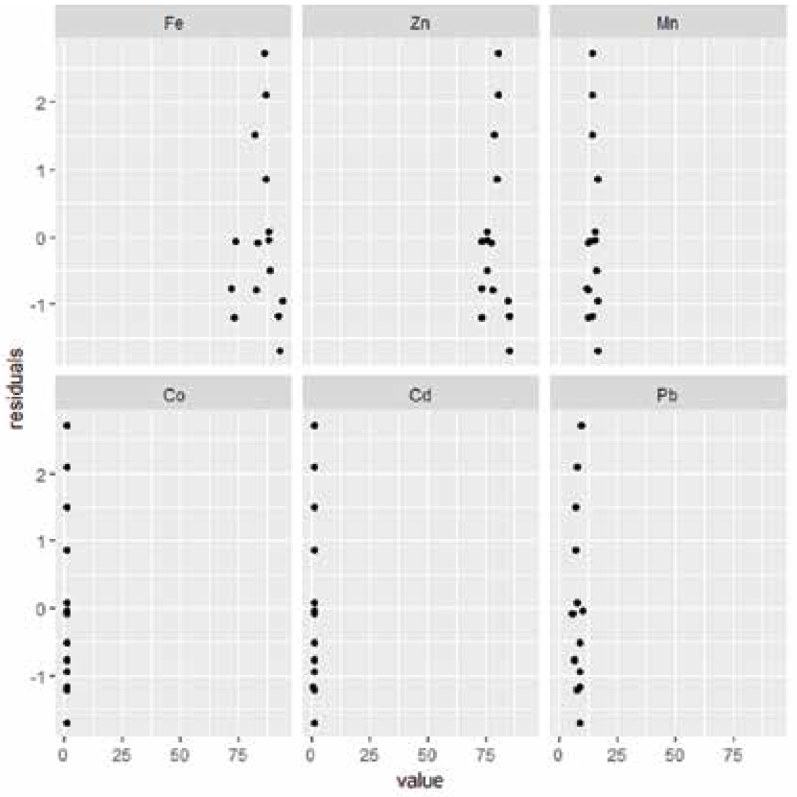

Fig. 1. Plots of the residuals versus each regressor

Figure 2 depicts graphically the differences in the calculation of actual data versus predicted data from the model, which indicate the ability to perform some calculations for different values of the variable Cu of the factors included in the presented model.

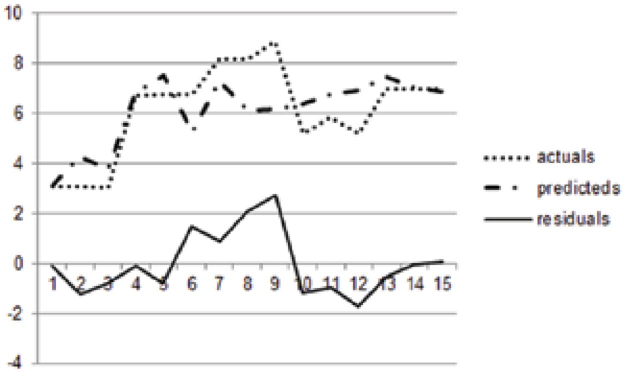

Fig. 2. Differences of actual data versus predicted data from the model of Cu

CONCLUSIONS

Results of the studied area showed that the selected metals concentrations were below the safe limits of WHO/FAO set for edible mushrooms and for foodstuffs. This could be attributed to the lack of anthropogenic input like mining and industry and low-scale agricultural activities. From the obtained concentrations of heavy metals it could be concluded that the locality Batak Mountain, Bulgaria is an ecologically clean area, very suitable for collecting wild edible mushrooms for daily rations.

Based on the obtained econometric model, the following interpretations for Cu contents in the wild edible mushroom *Suillus luteus* growing in the Batak Mountain, Bulgaria could be made:

– If Fe, Co and Cd increase by 1%, the effect of this increase would result in an increase in Cu by 5.08% on the average;

– If Zn, Mn and Pb contents decrease by 1%, the effect of this decrease would result in an decrease in Cu by 0.29% on the average.

REFERENCES

1. O. IŞILDAK, I. TURKEKUL, M. ELMASTAS, H.Y. ABOUL-ENEIN: Bioaccumulation of Heavy Metals in Some Wild-grown Edible Mushrooms. Anal Lett, **40**, 1099 (2007).
2. S. DOBRINAS, A. SOCEANU, G. STANCIU, V. POPESCU, L. ARNOLD: Trace Element Levels of Three Mushroom Species. Ovidius University Annals of Chemistry, **24**, 39 (2013).
3. L. DOSPATLIEV, V. LOZANOV, M. IVANOVA, P. PAPAZOV, P. SUGAREVA: Amino Acids in Edible Wild Mushroom from the Batak Mountain, Bulgaria. Bulg Chem Commun, **51**, 92 (2019).
4. P. KALAČ: Trace Element Contents in European Species of Wild Growing Edible Mushrooms: a Review for the Period 2000–009. Food Chem, **122**, 2 (2010).
5. F. ZHU, L. QU, W. FAN, M. QIAO, H. HAO, X. WANG: Assessment of Heavy Metals in Some Wild Edible Mushrooms Collected from Yunnan Province, China. Environ Monit Assess, **179**, 191 (2011).
6. K. GEZER, O. KAYGUSUZ, V. EYUPOGLU, A. SURUCU, S. DOKER: Determination by ICP/MS of Trace Metal Content in Ten Edible Wild Mushrooms from Turkey. Oxid Commun, **38**, 398 (2015).
7. L. DOSPATLIEV, V. LOZANOV, M. IVANOVA, P. PAPAZOV, P. SUGAREVA, Z. PETKOVA, D. BOJILOV: Comparison of Free Amino Acid Compositions of Stem and Cap in Wild Edible Mushrooms, Bulgaria. Oxid Commun, **41**, 542 (2018).
8. J. ÁRVAY, M. HAUPTVOGL, M. ŠNIRC, M. GAŽOVÁ, L. DEMKOVÁ, L. BOBUĽSKÁ, M. HRSTKOVÁ, D BAJČAN, L. HARANGOZO, J. BILČÍKOVÁ, M. MIŠKEJE, J. ŠTEFÁNIKOVÁ, V. KUNCA: Determination of Elements in Wild Edible Mushrooms: Levels and Risk Assessment. JMBFS, **8**, 999 (2019).
9. J. CAMPOS, N. TEJERA: Substrate Role in the Accumulation of Heavy Metals in Sporocarps of Wild Fungi. Biometals, **22**, 835 (2009).
10. I. ŠIRIĆ, I. KOS, D. BEDEKOVIĆ, A. KAIĆ, A. KASAP: Heavy Metals in Edible Mushrooms *Boletus reticulatus* Schaeff. Collected from Zrin, Mountain, Croatia. Period Biol, **116**, 319 (2014).
11. L. DOSPATLIEV, M. IVANOVA: Concentrations and Risk Assessment of Lead and Cadmiumin Wild Edible Mushrooms from the Batak Mountain, Bulgaria. Oxid Commun, **40**, 993 (2017).
12. A.-L. ZOCHER, D. KRAEMER, G. MERSCHEL, M. BAU: Distribution of Major and Trace Elements in the Bolete Mushroom *Suillus luteus* and the Bioavailability of Rare Earth Elements. Chem Geol, **483**, 491 (2018).

13. B. KUZIEMSKA, A. WYSOKIŃSKI, D. JAREMKO, K. PAKUŁA, M. POPEK, M. KOŻUCHOWSKA: The Content of Copper, Zinc, and Nickel in the Selected Species of Edible Mushrooms. Environmental Protection and Natural Resources, **30**, 7 (2019).
14. J. FALANDYSZ, A. SAPKOTA, A. DRYŻAŁOWSKA, M. MĘDYK, X. FENG: Analysis of Some Metallic Elements and Metalloids Composition and Relationships in Parasol Mushroom *Macrolepiota procera*. Environ Sci Pollut R, **24**, 15528 (2017).
15. L. DOSPATLIEV, M. IVANOVA: Determination of Heavy Metals in Mushroom Samples by Atomic Absorption Spectrometry. Bulg Chem Commun, **49**, 5 (2017).
16. N. PROSKURA, J. PODLASIŃSKA, L. SKOPICZ-RADKIEWICZ: Chemical Composition and Bioaccumulation Ability of *Boletus badius* (Fr.) Fr. Collected in Western Poland. Chemosphere, **168**, 106 (2017).
17. S. MAREK, P. RZYMSKI, P. NIEDZIELSKI, A. BUDKA, M. GAŞECKA, P. KALAČ, A. JASIŃSKA, S. BUDZYŃSKA, L. KOZAK, M. MLECZEK: Comparison of Multielemental Composition of Polish and Chinese Mushrooms (Ganoderma spp.). Eur Food Res Technol, **243**, 1555 (2017).
18. A. ZOCHER, D. KRAEMER, G. MERSCHEL, M. BAU: Distribution of Major and Trace Elements in the Bolete Mushrooms *Suillus luteus* and the Bioavailability of Rare Earth Elements. Chemical Geology, **483**, 491 (2018).
19. P. RZYMSKI, P. KLIMASZYK: Is the Yellow Knight Mushroom Edible or Not? A Systematic Review and Critical Viewpoints on the Toxicity of *Tricholoma equestre*. Compr Rev Food Sci F, **17**, 1309 (2018).
20. I SÖNMEZ, H. KALKAN, H. DEMIR, R. KÜLCÜ, O. YALDIZ, M. KAPLAN: The Effects of Some Agricultural Wastes Composts (Prunning Waste-spent Mushroom Compost) on Lettuce Growth (*Lactuca sativa* L.). Int J Agric Life Sci, **3**, 9 (2019).
21. M. IVANOVA, L. DOSPATLIEV, P. PAPAZOV: Application of ICP-OES Method of Determination of K, P, Mg, Na and Ca in Nine Wild Edible Mushrooms with A Chemometric Approach. Cr Acad Bulg Sci, **72**, 182 (2019).
22. K. TURKDOGAN, F. KILICEL, K. KARA, I. TUNCER, I. UYGAN: Heavy Metals in Soil, Vegetables and Fruits in the Endemic Upper Gastrointestinal Cancer Region of Turkey. Environ Toxicol Phar, **13**, 175 (2003).
23. S. SHAPIRO, M. WILK: An Analysis of Variance Test for Normality (*Complete Samples*), Biometrika, **52**, 591 (1965).
24. D. GUJARATI: Basic Econometrics. McGraw-Hill, Singapura, 2003.
25. https://www3.nd.edu/˜wevans1/econ30331/Durbin_Watson_tables.pdf.
26. https://www.statisticssolutions.com/wp-content/uploads/wp-post-to-pdf-enhanced-cache/1/assumptions-of-multiple-linear-regression.pdf.
27. WHO (World Health Organization): Evaluation of Certain Foods Additives and Contaminants (Twenty-Six Report of the Joint FAO/WHO Expert Committee on Food Additives). WHO Library Cataloguing-in-Publication Data, WHO, Geneva, Switzerland, 1982.
28. http://www.stat.purdue.edu/~jtroisi/STAT350Spring2015/tables/FTable.pdf.

Received 2 May 2019
Revised 18 May 2019

Oxidation Communications 42, No 2, 194–208 (*2019*)

Tribological interactions on metal surfaces

IMPROVING THE TRIBOLOGICAL CHARACTERISTICS OF HELICAL DRILLS FROM HIGH SPEED STEEL BY MEANS OF A CONTACTLESS LOCAL ELECTRICAL DEPOSITION WITH COMPOSITE CARBIDE ELECTRODES BASED ON TiC AND TiN

T. PENYASHKI*, G. KOSTADINOV, E. DIMITROVA, I. MORTEV

Institute of Soil Sciences, Agro-technologies and Plant Protection 'N. Pushkarov',
3 Shose Bankya, Sofia, Bulgaria
E-mail: *tpeniashki@abv.bg*

ABSTRACT

In this work was conducted a study of the wear of drills from high-speed steel HS-5-2 at cutting of carbon steel 45 (with 0.45% C). The tools are coated with new non-tungsten carbide composite materials based on TiC, TiN and TiCN. The coatings are applied by contactless Local electro spark deposition (LESD). It has been found the complex influence of the electrical parameters of the deposition process and the morphology and composition of the coatings onto the nature of the amendment of the wear of the drills, and on the contact processes during cutting. The use of the new non-tungsten electrodes results in an increase the durability of the coated drills to 1.9–2.5 times as compared the non-coated ones and up to 1.4 times than that of the coated with electrodes based of tungsten carbide. The technological conditions in which is obtained a minimum wear of the layered drills are determined. The wear analysis shows that the LESD can successfully be used for increasing wear resistance of drills, but in order to obtain maximum a durable and reliable tribological effectiveness is needed preliminary optimisation of parameters of the regime and materials for deposition according to the specific cutting conditions.

Keywords: coatings, electrode materials, non-tungsten, wear, roughness, microhardness, phase composition.

AIMS AND BACKGROUND

Electrical spark deposition (ESD) is a simple, easy, cheap and universal process for locally deposition of single and multilayer coatings from any and on all kinds of

---

[*] For correspondence.

conductive materials with low operation cost. Along with its other triboapplications, surface modification and application of wear-resistant coatings on friction-resistant metal surfaces, the electrical spark deposition creates prerequisites for increasing the wear resistance of the cutting tools. The interest in using LESD for metal cutting tools is motivated by the fact that the popular and proven physical vapour deposition PVD and chemical vapour deposition CVD methods and coatings of TiN, AlN, TiCN, CrN, TiAlN, TiC are of higher quality than electrospark deposition. Nevertheless, PVD and CVD methods are costly, with expensive equipment and infrastructure that require considerable investment, while ESD is a cheap, affordable and wide-ranging process, and along with many other applications, could also be used to strengthen cutting tools.

The experimental data in the literature and existing theoretical developments on the issue of ESD tools are in most cases defragged and have multidirectional and unsystematic character. In the works of most researchers, only individual data are given mainly about the effect of coatings, but the phenomena occurring during the cutting process and the wear of the tools are not completely revealed. Some authors reported absence of effect or minimum one, and others[1–14] for 50–400% increase in tool life. In Ref. 11 was reported for five-times increase tool life of drill bits, and in Ref. 12 – 20-times increase in tool life of the layered tools.

Furthermore, some authors indicate that the durability of the instruments with tungsten carbide coatings[4–6,10,12] is higher than that of the ESD with other electrodes, and others[1–3,8,9,12–14] – that the tool life of coated with electrodes T15K6 and those based on TiN, TiCN, etc. is higher than that of the layered with tungsten carbide electrodes. This is mainly related to the lack of sufficient knowledge about the process of friction and wear mechanism of layered instruments. The above differences are due to the fact that at the studies of wear and durability is not taken into account the simultaneous influence of all the technological factors influencing the wear process: materials, modes and conditions for electrospark deposition, geometric parameters of the cutting tool, cutting mode parameters, the kind of the kinematics cutting scheme and the properties of the processed material, which define the different specificities of the contact processes and phenomena between the chip and the coated surface.

For achieving an improved tool life, it is necessary to optimise the composition of electrode materials and process parameters for ESD of the tools, taking into account the mode and cutting conditions. However, it is often necessary also to optimise the machining conditions at cutting with coated tools to achieve an enhanced tool life. In the case of ESD for laminating electrodes, hard alloys based on tungsten carbide – WC-Co are most often used. This often results in contradictory and insufficiently satisfactory results.

In this regard, the aim of this work is to investigate the complex influence of the composition of hard alloy electrode materials based on TiC, TiN and TiCN and the parameters of the regimes for their deposition on the wear of the coated instruments, and experimentally to evaluate the efficiency and possibilities of using non-tungsten solid alloys for ESD on cutting tools and for obtaining coatings with increased hardness, wear resistance and enhanced serviceability compared to existing ones.

EXPERIMENTAL

This study examines the complex influence of electrical parameters of the ESD process, the type of electrode material and the qualitative characteristics, composition, and structure of the resulting coatings on the wear properties of drills with diameter 6 mm made from high-speed steel – HSs-6-5-2- (5.7–6.7% W, 4.7–5.2% Mo, 4.7–5.2% Co, 1.7–2.2% V, 0.82–0.92% C). The variant of the classical electro-spark deposition with a vibrating electrode – contactless Local Electro-Spark Deposition (LESD) (Ref. 15) was used in this work. Deposition was performed on a machine type ‘Elfa 541’ (Ref. 16) (Fig. 1) with single pulse energy up to 0.02 J. The application of the coatings was carried out with cylindrical rotating electrode at a controlled rate up to 1500 rpm with a diameter of 1–1.5 mm, established in the laminating head. At the deposition of the coating work piece was moved with a controlled rate of axes *X* and *Y*. Automatic regulator of inter-electrode distance maintains the necessary gap in which the plasma spark discharges run and it ensures high stability of the process.

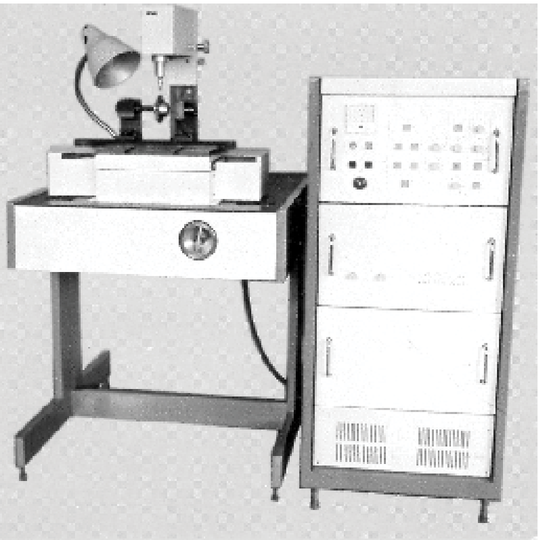

Fig. 1. Machine for contactless local electro-spark deposition LESD type ELFA 541 with semi-automatic control

The resulting coatings are of high density, uniformity, repeatability of the quality characteristics and low roughness, which in most cases does not require further processing. The micro geometry and topography of the coatings defining the actual area of the discrete friction contact are suitable for application areas with high demands on accuracy and roughness. This ensures of LESD certain advantages that give it priority over the vibration methods for stratification of all tools and parts with high requirements on the quality of the work surface, for example, obtaining of thin, dense and smooth coatings on the cutting edges of tools and dies, punches, formers[4,7,15,16].

During the experiments the following primary adjustable parameters of the regime for LESD were used:

– Pulse current amplitude – $I = 8–16$ A;

– System voltage (circuit voltage) – $U = 90$ V;

– Pulse duration – $T_i = 3, 5, 8, 12, 20$ μs;

– Capacity – $C = 0.2, 0.5, 0.7, 1$ μF;

– Coefficient of filling of the pulses – $\tau = 0.1$ and 0.2, $\tau = T_i/T$, where $T = T_i + T_\text{p}$ is the period of the pulse, and T_p – pause between the pulses; $1/T = f$ – pulse frequency;

– Number of passages of the electrode – $n = 2$.

The application of coatings was carried out with two passes of the electrode.

– Speed of deposition (coverage rate) – $V = 0.6$ mm/s.

Electrode materials. Non-tungsten hard metal composite electrode materials with bonding metals Ni, Cr, Mo and various technological additives such as Cu, Al_2O_3, B, etc., with the following designations were selected and used:

TNM10 – TiC + 10% Ni + Mo
TN10 – TiN + 10% Ni + Cr
KNT16 – TiCN + 16% Ni+Mo
TNM20 – TiN + 20% Ni + Cr
TC – TiC + 14% Ni, Mo + 1% Cu, B, Al_2O_3
TN – TiN + 14% Ni, Cr + 1% Cu, B, Al_2O_3
TC–TN – TiC + TiN + 12% Ni, Mo, Cr + 1% Cu, B, Al_2O_3

Coatings of composite electrode material with indication WK9 and composition 2.8% TaC + 9% Co + WC studied and developed earlier[16–18] were used as reference for comparison with the resulting coatings from the non-tungsten electrodes.

Layering electrodes with a diameter of 1–1.5 mm were obtained by electrically discharge cutting from monolithic plates, prepared by the methods of powder metallurgy.

The coating was deposit to the front surface on the major cutting edge (Fig. 2*a*) and on cutting tape on the back surface (Fig. 2*b*) with two passes of hardfacing electrodes.

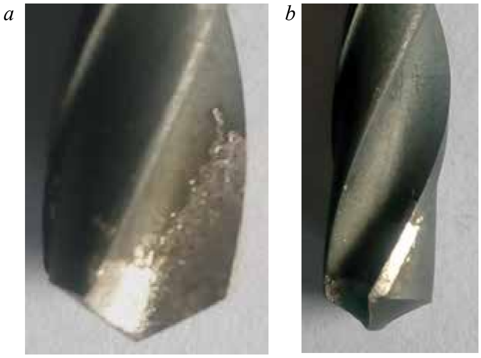

Fig. 2. Scheme for deposition of coatings

Cutting tests conditions. Machine: universal column drilling machine trademark PK203;

– Material processed bands of Steel 45 (0.45% C) with dimensions 500 × 100 × 20, HB190;

– Lubricant-coolant: 5% solution of boryol in water;

– Cutting mode: rotation speed – 2000 min^{-1}; feed *f* – 0.16 mm/rpm;

– Drilled are blind holes with a depth of 18 mm.

Methods of measurements. Wear – the size of the flank wear land width on the back surface – VB was measured by digital microscope VT300 (Fig. 3), with accuracy of reporting 0.01 mm according to the wear scheme (Fig. 4).

Fig. 3. Digital microscope VT-300

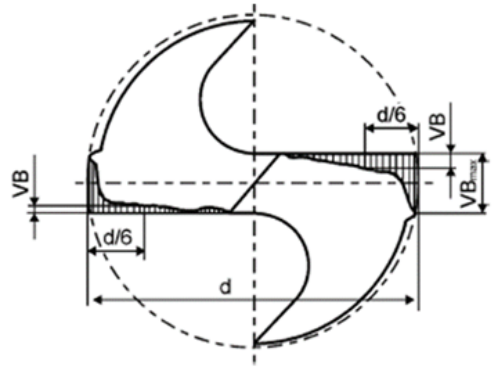

Fig. 4. Flanks wear land width on the back surface -VB

At regular time intervals was measured wear of tools VB and built curves 'Time-wear' – VB = $f(t)$. Five parallel experiments were carried out. The results obtained were processed by determining the standard deviation and the confidence interval. Sharp separation values were rejected by the method of Grubbs.

The surface roughness R_a (μm), the thickness δ (μm) and microhardness HV of the resulting coatings were measured by using a profilometer AR-132B (Fig. 5), a Pocket Leptoskop 2021 Fe (Fig. 6) and a microhardometer Al 150A (Fig. 7). For complex evaluation of the qualities of the tools was adopted tool wear and tool life. For studying the wear on cutting tools were carried out studies on the influence of cutting time t on the parameters of wear hi. The average width of the wear on the back surface – VB – according to Fig. 4 is measured through regular intervals. Usually was worked up to the wear VB = 0.3 mm, but in some cases, this value may be smaller or larger.

Fig. 5. Profilometer -AR-132B

Fig. 6. Pocket Leptoskop 2021 Fe

Fig. 7. Micro hardometer Al 150A

RESULTS AND DISCUSSION

Three modes for LESD of the samples for the cutting tests were selected based on the results obtained from the preliminary studies of the roughness, thickness, structure and microhardness of the coatings[16–19]. Homogeneous, dense, smooth and adherent coating layers with good repeatability of the qualitative characteristics have been obtained during LESD experiments. The values of the electrical parameters of LESD modes – current I, the capacity C, duty cycle τ, and the duration of the pulses T_i, as well as the coating parameters values – roughness R_a, thickness δ, and microhardness HV, according to the LESD mode parameters, are shown in Table 1. With each of the investigated electrodes with the above three modes, drills were deposited and their wear at cutting was examined.

Table 1. Coating parameters obtained at the 3 selected LESD modes

No	Electrode	1. I = 14.4 A,T_i = 8 μs, C = 0.47 μF, τ = 0.2			Coef. hardening	2. I = 14.4 A, T_i = 12 μs, C = 0.68 μF, τ = 0.2			Coeff. hardening	3. I = 16A, T_i = 12 μs, C = 1 μF, τ = 0.1			Coeff. hardening
		R_a (μm)	δ (μm)	HV (GPa)	–	R_a (μm)	δ (μm)	HV (GPa)	–	R_a (μm)	δ (μm)	HV (GPa)	–
1	WK9	1.26	5.9	13.40	1.5 3	1.38	6.9	13.40	1.52	1.55	8.3	14.00	1.59
2	TNM20	1.08	4.7	11.79	1.34	1.19	5.7	12.53	1.42	1.33	6.2	13.45	1.55
3	TNM10	0.82	3.9	11.80	1.34	0.97	4.9	12.89	1.46	1.09	5.5	13.55	1.54
4	KNT16	1.04	4.9	12.76	1.45	1.18	5.5	11.84	1.34	1.28	6.9	13.79	1.58
5	TN10	0.78	3.9	11.37	1.29	1.03	4.9	13.06	1.48	1.15	5.3	13.81	1.58
6	TC	1.02	4.6	12.19	1.38	1.09	5.3	13.72	1.56	1.25	5.8	12.90	1.47
7	TN	0.94	4.5	11.37	1.29	1.02	5.3	13.06	1.48	1.19	5.7	13.81	1.58
8	TC-TN	1.02	5.4	12.90	1.47	1.05	5.5	13.50	1.53	1.22	5.8	14.28	1.62
9	substrate	0.65		8.80	1.00	0.65		8.80	1	0.65		8.80	1.00

The minimum and maximum values (borders) of the thickness δ, of surface roughness R_a, and microhardness HV of coatings, obtained from the studied electrodes at the different used values of parameters of regimens for ESD is shown in Table 2. From the results obtained it is found that the specific values of the roughness and the thickness of the coatings under the same other conditions are different for the different electrodes. The lowest values of R_a and δ are obtained for the coatings deposited with the electrodes TNM10 and TN10, and the highest – at LESD with electrode TNM20, respectively, we can expect that they have the greatest coefficients of friction.

It is obvious that the increase in the quantity of solder metals in the composition of the electrode materials in the direction TNM10 – TC-TNM20 leads to an increase of the roughness R_a and the thickness δ of the obtained coatings and micro-hardness slightly decreased.

Table 2. Range of variation of coating parameters

Electrode	Coatings			
	R_a (μm)	δ (μm)	HV (GPa) (on average)	coefficient of hardening
WK9	0.95–1.6	4.50–8	13.6	1.58
TNM10	0.60–1.19	3.55.5	13.3	1.54
TC	0.70–1.3	4.00–6	13.0	1.51
TNM20	0.85–1.3	3.00–6.5	12.7	1.48
TN10	0.65–1.2	2.50–5	13.2	1.53
TN	0.63–1.25	2.55–5	13.0	1.51
KNT16	0.70–1.25	3.55–8	12.5	1.45
TC-TN	0.80–1.35	3.50–6	13.35	1.55
Substrate	0.63		8.6	1.00

The microhardness of the coatings is improved compared with the substrate and varies in too broad a range. There is a tendency to increase with an increase in pulse energy. At TC, TC-TN and TN electrodes, the HV values are lower than those obtained with an electrode THM10, which is probably due to the higher content of soldering metals in the composition of these electrodes.

Figure 8 shows the variation of flank wear over time of uncoated and coated drills with studied electrodes at cutting speed $V = 38$ m/min and feed $f = 0.16$ mm/rpm. The tool life is conventionally defined in terms of flank wear width. As per the accepted definition the tools life equals the times until flank wear reaches a value of 0.3 mm. It is can see that at all studied cutting data the nature of wear of the LESD tools is similar to that of uncoated ones. The differences are in the lower values of the parameters characterising the wear.

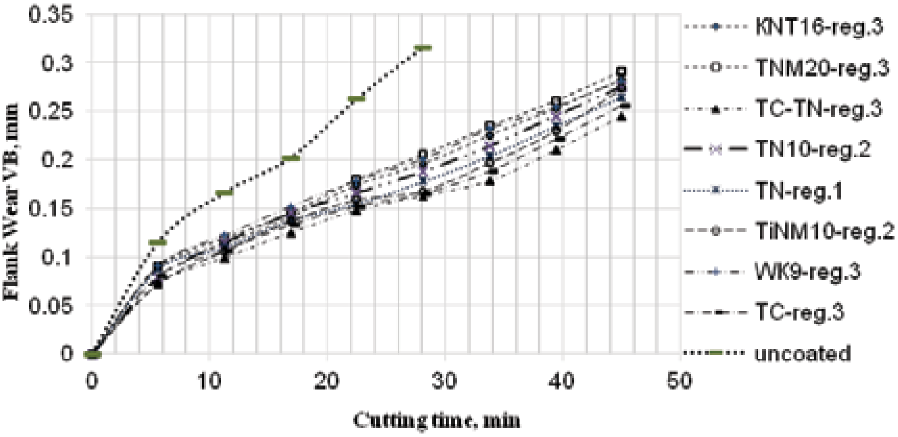

Fig. 8. Development of wear of uncoated and coated drills at regimes 1, 2 and 3 in time, cutting speed *V* = 38 m/min, feed *f* = 0.16 mm/rpm

From the results obtained, it is visible that the coated with non-tungsten electrode drills have a lower wear than that of the non-coated ones. From the curves obtained, it has been found that the applied coatings reduce tool wear on the rear surfaces. The comparative evaluation of the wear of drills showed that the lowest wear have the drills with coatings from TC-TN electrode deposited at regime 3 (Table 1). At criterion of wear VB = 0.2 mm, the tool life of the layered with this electrode tools are up to more than 2.5 times higher than that of uncoated ones and their service life increased by 20–30% compared to coatings from WC based electrodes.

Apparently, the combination of titanium carbide and titanium nitride in the composition of the electrodes is more advantageous in terms of the wear. In LESD with this electrode, the coating is enriched simultaneously with carbides, nitrides and carbonitrides, which give it a higher wear resistance than only TiC or only TiN.

The wear of the coated drills varies non-monotonically depending on the ratio of the components of the bonding metals in the composition of electrode in direction – TNM20-TC-TNM10 (Fig. 8). In the present case, the main phases of the coating are the solid component titanium carbide TiC (with a microhardness of 32 GPa) and a soft component Ni+Mo. The tools deposited with electrodes with a smaller amount of bonding metals show lower wear than those deposited with the electrodes TNM20 – the apparently higher content of soldering metals has a negative impact on the wear.

For the compositions with predominant content of solid phase TiC > 90%, wear will be higher because of the high brittleness of this phase, and for compositions with predominant content of bonding components – in this case TNM20, the wear is greater because of the lower hardness and lower wear resistance of this phase. Since the differences in the wear of coated drills with electrodes TNM10, TC and TNM20 reaches only up to 15–20%, it can be considered that the most suitable content of plasticising phases in the composition of these electrodes varies within the range 10–15%. When

Ni + Mo are about 10–15% achieves a ratio between the hard and soft components in the coating, whereby minimum wear of the drills was obtained. The above conclusion however is not valid for the TC-TN electrode, where wear is lowest.

The wear of the tools with coatings from electrodes TNM20, KNT16 and TN10 is comparable to that of the layered with electrode WK9. When comparing the influence of the type of the electrodes is established that the differences in the tool life can reach to 30%. The results obtained show that the influence of the electrode material is also related to the LESD mode. Figure 9 shows the wear of drills deposited under the three selected modes with electrode TNM10. In the regime with higher energy, the wear of the tools is lower. The classical surface microgeometrycal parameters (R_a, R_z, R_{max}, t_p, S_m, etc.) in this case do not reflect the actual situation of the friction contact. Coatings with higher values of R_a, R_z, R_{max} have higher wear resistance than those with low roughness. The lower wear of these coatings is apparently due to the higher amount of carbides and ultra-dispersion phases that ‘offset’ the negative impact of roughness on wear.

Comparison of the influence of LESD modes (Figs 8 and 9, and Table 1) shows that with the increase of pulse energy the wear decreases – the lowest wear of the samples with the highest impulse energy regime – in this case mode 3, which justifies the need for further increase of the energy of the impulses.

Figures 10 and 11 show the variance of the dispersion and the confidence interval of the non-coated and deposited in the 3 modes of the THMM10 electrode drills as a function of the cutting time.

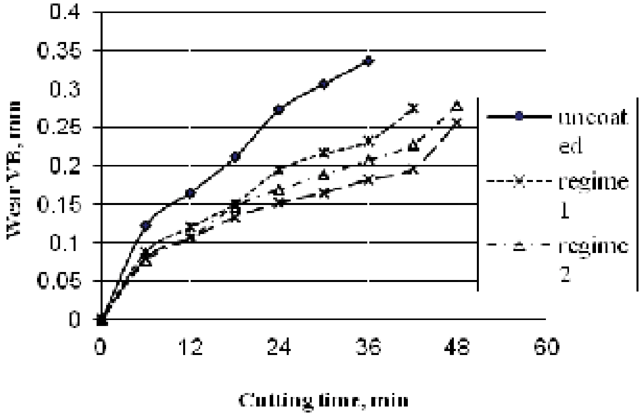

Fig. 9. Wear of coated drills with electrode TNM10 at regimes 1, 2 and 3 in time

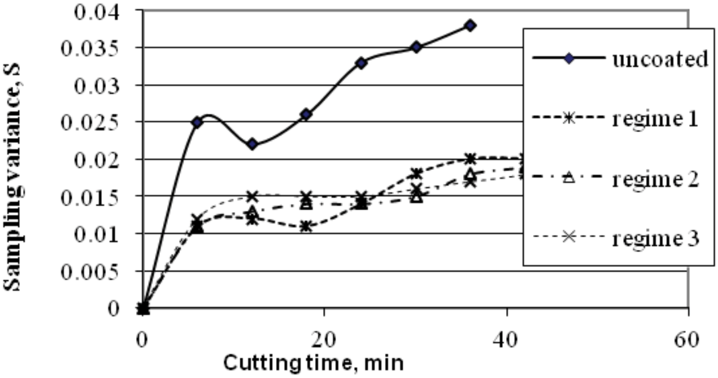

Fig. 10. Changes in sampling variance of wear in time

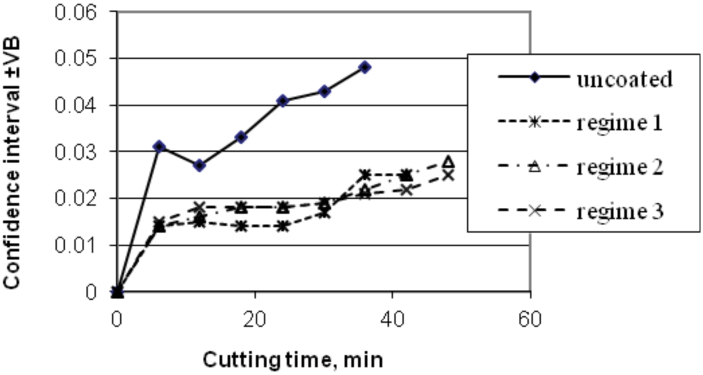

Fig. 11. Changes in confidence interval of wear in time

From the above figures it can be seen that the dissipation of wear and the confidence interval after LESD is significantly reduced. Therefore, LESD with no tungsten electrodes not only increases the durability of the drills, but also increases their reliability.

Table 3 and Fig. 12 show the durability of the coated drills at different wear criterion. Figure 13 shows the effect of LESD under different criteria for wear of coated and non-coated drills. The effect is defined as the ratio of the durability of the coated to the durability of the uncovered drill. From the results of the comparative wear tests (Table 3, Figs 12 and 13) is established that the effect of LESD is different for different wear criteria. Differences occur at the beginning of the cutting process. At the beginning of the work the differences in tool life are smaller, and the differences in the durability of the tools coated with different electrodes are smaller too.

Table 3. Durability (min) at different wear criteria

VB (mm)	Uncoated	TNM20	TNM10	TC	KNT16	TN	TN10	TC-TN	WK9
0.10	5	7.5	9.5	9.3	8.8	9.4	9.3	11	7.6
0.15	9.2	17	21.4	22.5	18.5	22	20.4	24	17
0.20	16.5	28	34	35.6	30	33.6	32	38	29
0.25	21	37.2	41.5	43.5	39.6	42.4	40.8	46	39.6

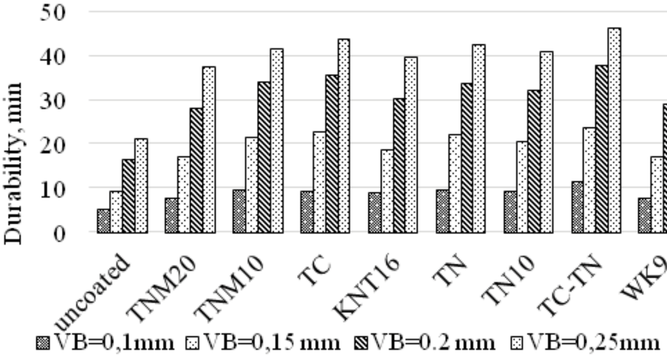

Fig. 12. Durability, min at different wear criteria

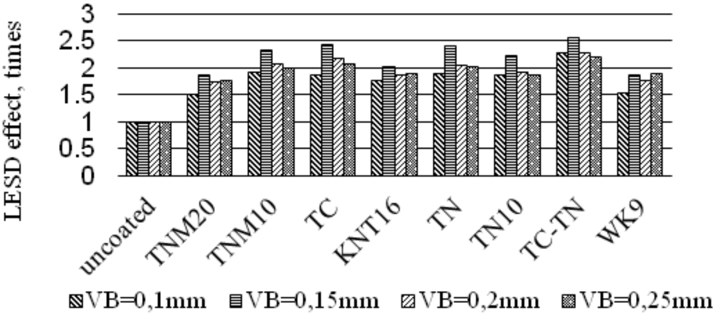

Fig. 13. Effect of LESD at different criteria for wear

With an increase in the time of cutting these differences increase, reaching a maximum value within the range VB = 0.15 mm (Figs 12 and 13, Table 3). Under the 0.2 mm criterion, the effect diminishes slightly and then remains relatively constant. When criterion of wear is 0.25 mm, the coated drills are with – 1.9–2.2 times higher durability than those of the uncoated samples, and to1.2 times higher than the deposited with electrode WK9 drills. At criterion of wear 0.15 and 0.2 mm the deposited tools have 2.6 times higher tool live than those of uncoated drills, and up to 1.4 times higher than the deposited with electrode WK9 drills. Coated tools wear takes place in two stages. The first coating is destroyed due to abrasion and delamination from the substrate. In the second phase, the remaining uncoated base is wear out. The layer of background material left without coverage for longer keeps their working capacity.

At all tests the wear of bare tools develops a higher rate compared to coated tools. Increasing the cutting time leads to gradual wiping of the coating and, as a result, the effect decreases. From here it can be concluded that coatings slow down the development of wear over time, prolonging tool life. The LESD effect changes over time, with the highest values being observed in the first part of the wear curve – after the initial lapping of friction surfaces. The main reason for the reduced wear, in this case, are higher diffusion resistance, hardness and chemical resistance of the TiC and TiN in the coating and subsurface layer of the tool steel. The results obtained show that the efficiency of the use of LESD coatings from electrodes based on TiC and TiN reduce the wear intensity, slow down its development over time, and can be successfully used to increase the durability of cutting tools from high speed steel. Through the LESD with composite coatings based on TiC and TiN, the functional characteristics of the cutting tools are improved.

CONCLUSIONS

The results obtained in this paper show that the non-tungsten carbide electrodes can be effectively used for LESD of tools from high-speed steels. The efficiency of the use of electrodes based on TiC and TiN is associated both to the composition of the electrode material and to the energy of the LESD modes.

The complex influence of the electrical parameters of the deposition process and the electrode materials (respectively the morphology and composition of the coatings) onto the wear and the contact processes, was investigated. The possibility of creating coatings of tungsten-free hard alloys at LESD high-speed steel tools is shown. It has been established that new coatings improve 20–40% the performance of the surface layer compared to tungsten carbide electrodes and to 2.5-fold higher than that of non-coated.

It has been found the impact of different electrode materials on the wear of layered tools. The lowest wear showed the coatings of multicomponent electrodes based on TiC–TiN.

Through the LESD with composite coatings based on TiC and TiN, the functional characteristics of the cutting tools are improved. Their improved quality compared to tungsten carbide-based electrodes coatings consists in increasing the continuity of coatings, reducing porosity, forming a lightweight coating with lower roughness and lower wear.

Coatings reduce the wear intensity, slow down its development over time, and can be successfully used to increase the durability of cutting tools from high speed steel.

The results of the investigations made it possible to optimise the surface hardening regimes.

ACKNOWLEDGEMENTS

The present work is based on researches that are funded from the Bulgarian National Science Fund of the Ministry of Education and Science under the project ‘Research and Development of New Wear-Resistant Coatings Using Compositional and Nano Materials’.

REFERENCES

1. A. E. GITLEVICH, V. V. MIKHAĬLOV et al.: Electrospark Alloyng of Metal Surfaces. Chisinau, Stinitsa. **198**, (1985) (in Russian).
2. G. V. SAMSONOV, A. D. VERKHOTUROV, G. A. BOVKUN, V. S. SYCHEV: Electrospark Alloyng of Metal Surfaces. Scientific Opinion, Kiev, 1976. 220 p. (in Russian).
3. A. D. VERKHOTUROV, I. M. MUHA: Electro-spark Alloying Technology for Metal Surfaces. Technika, Kiev, 1982. 182 p. (in Russian).
4. V. N. GADALOV, D. N. ROMANENKO, I. M. GORYAKIN, Yu. P. KAMYSHNIKOV, V. I. SHKODKIN: Local Selective Application of Electrophysical Coatings on Metalworking Tools, Strengthening Technologies and Coatings. **4**, 33 (2008) (in Russian).
5. V. N. GADALOV, R. E. ABASHKIN, Yu. V. BOLDYREV, E. F. BALABAEVA, A. I. LYTKIN: Cutting-tool Wear and Hardening of High-speed Steel by Local Electrospark Coating Application. Russian Engineering Research, **29** (4), 419 (2009).
6. V. N. GADALOV, Yu. V. BOLDYREV: Hardening of the Cutting Tool by the Method of Local Electrospark Deposition. **Stin.??? 9**, 18 (2006) (in Russian).
7. T. G. PENYASHKI, G. D. KOSTADINOV: Enhancing Durability and Resources Agricultural Machinery Using Electrospark Hardening. Agricultural Engineering (Bulgaria), (4-6), 48 (2013) (in Bulgarian).
8. T. PENYASHKI: Investigation of the Wear of Steels with Coating Laid by Local Electric Spark Deposition, J Balk Tribol Assoc, **7** (2), 66 (2000).
9. A. V. RIBALKO, O.A. SAHIN: Modern Representation of the Behavior of Electrospark Alloying of Steel by Hard Alloy. Surf Coat Technol, **201**, 1724 (2006).
10. A. A. BURKOV, S. A. PYACHIN: Investigation of WC-Co Electrospark Coatings with Various Carbon Contents. J Mater Eng Perform, **23**, 2034 (2014).
11. K. R. C. SOMA RAJU, NADIMUL HAQUE FAISAL, D. SRINIVASA RAO, S. V. JOSHI, G. SUNDARARAJAN: Electro-spark Coatings for Enhanced Performance of Twist Drills. Surf Coat Technol, **202**, 1636 (2008).
12. E. ALLEN BROWN, GARY L. SHELDON, ABDEL E. BAYOUMI; A Parametric Study of Improving Tool Life by Electrospark Deposition.Wear. **138** (1–2), 137 (1990).
13. A. D. VERKHOTUROV, I. A. PODCHERNYAEVA, L. F. PRYADKO, F. F. EGOROV: Electrode Materials for Electrical Spark Alloying. Nauka, Moscow, 1988, p. 224 (in Russian).
14. A. D. VERKHOTUROV, S. V. NIKOLENKO: Development and Creation of Electrical Materials for Electric-Spark Alloying. Strengthening Technologies and Coatings, **2**, (2010) (in Russian).
15. B. ANTONOV: Device for Local Electric-spark Layering of Metals and Alloys by Means of Rotating Electrode. US Patent No 3832514, 1974. www.google.ch/patents/US3832514.
16. T. PENYASHKI, G. KOSTADINOV, I. MORTEV, E. DIMITROVA: Microstructures and Wear Properties of WC, TiN, and TiC Based Cermet Coatings Deposited on 210Cr12 and 45 Carbon Steel by Contactles Electrospark Process. Trib J BULTRIB, (6), 154 (2016).

17. T. PENYASHKI, G. KOSTADINOV, I. MORTEV, E. DIMITROVA: Improving the Surface Properties of Steel 210Cr12 by Non-contact Electrical Spark Deposition with Electrodes Based of WC and TiC. J Balk Trib Assoc, **23** (1-I), 69 (2017).
18. G. A. BOVKUN, Z. I. VLADKOVA, V. MOLYAR, T. PENYASHKI, Yu. G. TKACHENKO: Research Hardening of Steels at a Local Electrospark Deposition of Metal Carbides. Surface Engineering and Applied Electrochemistry, (1), 10 (1988) (in Russian).
19. T. PENYASHKI, G. KOSTADINOV, M. KANDEVA: Examination of the Wear of Non-tungsten Electro-spark Coatings on High Speed Steel. Agricultural Engineering, Research Papers, **49**, 1 (2017).

Received 4 February 2019
Revised 8 March 2019

Oxidation Communications 42, No 2, 209–229 (2019)

Technological aspects of oxidation processes, computer application

ECO-FRIENDLY PRODUCTION OF METAL NANOPARTICLES IMMOBILISED ON ORGANIC MONOLITHS FOR PEPSIN EXTRACTION

EMAN ALZAHRANI*, ASHWAQ T. ALKHUDAIDY

Chemistry Department, Faculty of Science, Taif University, Taif, Kingdom of Saudi Arabia
E-mail: *em-s-z@hotmail.com; ashwaq.t.kh@gmail.com*

ABSTRACT

Polymer monoliths modified by using nanoparticles (NPs) integrate high NP specific surface area with different monolith surface chemistry and high porosity. As a result, they have extensive applications within different fields, whereas nanomaterial-functionalised porous polymer monoliths have elicited considerable interest from investigators. This study is aimed at fabricating organic polymer-based monoliths from polybutyl methacrylate-*co*-ethylenedimethacrylate (BuMA-*co*-EDMA) monoliths prior to immobilisation of gold or silver metal on the pore surface of the monoliths using extracts of lemon peels. This was intended to denote a sustainable technique of immobilising nanoparticles that are advantageous over physical and chemical techniques because it is safe in terms of handling, readily available, environmentally friendly, and cheap. Two different methods were used in the study to effectively immobilise nanoparticles on monolithic components. The outcomes showed that soaking the monolith rod in the prepared nano solution directly and placing it within ovens at temperatures of 80°C constituted the most effective method. Characterisation of the fabricated monolith was undertaken using SEM/EDX analysis, UV-vis. spectra analysis, and visual observation. The SEM analysis showed that nanoparticles were extensively immobilised on the surface polymers. Another peak was attained through EDX analysis, thus confirming the Au atom existence at 2.83% alongside another peak that proved the Ag atom existence at 1.92%. The fabricated components were used as sorbents for purifying protein. The ideal performance was achieved using Gold nanoparticles (GNPs) immobilised organic monolith that attained a greater pepsin extraction recovery compared to Silver nanoparticles (SNPs) immobilised organic monoliths alongside bare organic-based monolith.

Keywords: polymer monoliths, immobilisation, metal nanoparticles, pepsin purification.

---

[*] For correspondence.

AIMS AND BACKGROUND

Monolithic static phases within electrochromatography and chromatography began eliciting the interest of investigators during the 1930s (Refs 1–3). Such components became popular as they were created from one piece of porous component that feature large flows via pores allowing separations at high rates of flow attained at low backpressures. Monoliths could be derived from organic[2], inorganic[4,5], and hybrid organic-inorganic materials[6–8].

Organic monoliths are characterised by chemical stabilities at an extensive pH range levels. Preparing organic monoliths can be considered simple. They could be produced through one-step polymerisation reaction or a common protocol could be utilised for obtaining parent polymers, which is chemically improved without considerably changing morphologies[8,9]. Preparation of monolithic columns has been undertaken directly within the confines of polypropylene tubes[9], poly(ether-ether-ketone) (PEEK) (Refs 10 and 11), fused silica lined stainless steel[12–14], fused silica[1,2,15], and stainless steel[16].

Characterisation of NPs is based on the high surface-to-volume ratio[17]; therefore, they may also be utilised for increasing the polymeric monolithic columns surface area[18]. Additionally, nano-architectures can be used for introducing more surface functionalities to columns of polymeric monoliths[8,18,19]. Moreover, monolithic adsorbent electrical conductivity, chemical and thermal stabilities, and structural rigidity are easily altered using NPs to increase molecular interactions and other properties[20–22]. Besides, nanoparticles can extend the specific monolith adsorbent surface area for increase of test analyst retention that results in overall reactivity and enhanced selectivity within the adsorbent[22,23].

Improvement of polymers has the potential of resulting in considerable increments in performance. Improved monoliths are characterised by high column effectiveness, good stability, and large surface area. Addition of nanomaterials to monoliths offers proper mechanical stability. Different nanoparticles have been included into polymeric monoliths to regulate monolithic column selectivity and retention characteristics, and in turn modify separation of tiny molecules. The distinct surface properties of nanoparticles alongside their huge surface-to-volume ratio enable the preparation of static phases with unique retentive power, and later increased separation selectivity to achiral and chiral solutes[24–26]. Currently, various methods are employed for modifying nanoparticle monoliths they include attachment of nanoparticles to preformed monolith surfaces, copolymerising functionalised monomer nanoparticles, and embedding nanoparticles within the monolithic matrices. Even though copolymerisation and embedding constitute direct and simplest methods, they lead to spread of nanoparticles in the entire monolithic matrix and thus most are inaccessible on the pore surfaces for desired interactions[27–29].

It is common knowledge that green chemistry is advantageous compared to physical and chemical techniques because it is safe in terms of handling, readily available, environmentally friendly, and cheap[30]. The objective for the investigation explored within the paper sought to fabricate organic polymer-based monolith through a poly (BuMA-*co*-EDMA) monolith prior to NPs immobilisation (gold and silver) on the monolith surface using extracts of lemon peel as the green technique. Two simple techniques were used to attain the most efficient technique of immobilising nanoparticles on the monolithic material surface: The initial technique involved addition of monolithic rods to nanoparticle solutions whereas the second technique was undertaken through mixing of a reduction reagent (extracts of lemon peel) with sources of iron ($HAuCl_4$ or $AgNO_3$ solution) prior to adding monolithic rods and putting it within an 80°C oven. Different chemical analytical tools such as UV-vis., EDX, and SEM, were utilised within the study to locate variations on surfaces of polymer monoliths prior to and after nanoparticle immobilisation. Organic monoliths prepared within home-made spin columns were utilised for purifying proteins. Monolithic spin columns that constitute a recent inclusion to SPE products were selected as they can increase the speed of sample preparation and accommodation of negligible specimen volumes. While few studies have cited the application of the method, the outcomes thus far can be considered promising[31].

EXPERIMENTAL

CHEMICALS AND MATERIALS

Chloroauric acid 99.9% ($HAuCl_4$ $3H_2O$), silver nitrate 99.8% ($AgNO_3$), butyl methacrylate 99% (BuMA), ethylene dimethacrylate 98% (EDMA), benzophenone, pepsin from gastric mucosa, and Whatman filter paper (pore size 25 μm and diameter 15 cm) were purchased from Sigma Aldrich (Poole, UK). Acetone, trifluoroacetic acid (TFA), acetonitrile (ACN), 1-decanol, methanol, isopropanol and ammonium acetate buffer were purchased from Fisher Scientific (Loughborough, UK). Disposable plastic syringes (1 ml) were purchased from Scientific Laboratory Supplies (Nottingham, UK). Blu-tack was purchased from Bookstore (Taif, KSA). Lemon was collected from a local market (Taif, KSA) and distilled water was used for the preparation purpose.

INSTRUMENTATION

A hot-plate stirrer from VWR International LLC (Welwyn Garden City, UK), a UV-vis. spectrophotometer from Thermo Scientific™ GENESYS 10S (Toronto, Canada). The oven came from F.LLI GALLI Company (Milano, Italy). Energy dispersive X-ray (EDX) analysis was performed using an INCA 350 EDX system from Oxford Instruments (Abingdon, UK), and centrifuge was from Lab Essentials, Inc. (Monroe, Georgia, US). A sonicator from Ultrawave Sonicator U 300HD (Cardiff, UK) and UV lamp (365 nm) from Spectronic Analytical Instruments (Leeds, UK) were used. The UV-vis. spectrophotometer was from Thermo Scientific GENESYS 10S (Toronto, Canada). A scanning electron microscope (SEM) Cambridge S360 from Cambridge

Instruments (Cambridge, UK) was used. High-resolution atomic force microscopy (AFM) was used to test morphological features and to produce a topological map (Veeco-di Innova Model-2009-AFM-USA). HPLC analysis was carried out using a Perkin Elmer LC200 series binary pump, a Symmetry C_8 column, 4.6 × 250 mm packed with silica particles (size 5 µm) from Thermo Fisher Scientific (Loughborough, UK) and a Perkin Elmer 785A UV/Visible Detector from Perkin Elmer (California, USA).

FABRICATION OF MONOLITHIC MATERIALS

Preparation of polymer-driven monolith in homemade spin columns in room temperature under ultraviolet radiation was achieved through the photo-initiated free radical polymerisation. The preparation of polymer-based monoliths was undertaken through the process highlighted in the previous work[32] alongside some improvements. The polymerisation mix featured the porogenic solvent system (1450 µl of 1-decanol and 4550 µl of isopropanol), the free radical photoinitiator (0.1 g of benzophenone), a crosslinker (1600 µl of EDMA), and a monovinyl monomer (2400 µl of BuMA). Sonication of the polymerisation mixture was undertaken for 5 min to dissolve the initiators and generate a homogeneous solution through a sonicator. A 0.25 ml Eppendorf tube was filled with the polymerisation mix and placed below the ultraviolet lamp at 365 nm in room temperature. After the polymerisation reactions, the monolithic components were washed in distilled water and methanol in the ratio of 50:50.

IMMOBILISATION OF NPS ON THE MONOLITH

Two diverse techniques were utilised within the study to locate the optimum method for nanoparticle immobilisation on the polymer monolith surface. The two methods mainly involved soaking monolithic rods (1 cm) within nanoparticle solutions and placing them in 80°C oven. A green chemistry technique to preparing NPs was used with extracts of lemon peel, as stated earlier[33] alongside minor modifications: 20 g of lemon peel were added to 100 ml of deionised water prior to boiling the mixture for 30 min at 80˚C. The solution underwent filtration with Whatman paper then added to 2 mM ion source solutions in the ratio of 2:1 at room temperatures (25 ± 3˚C) and preserved within a dark room for 1 day.

Method one. A solution of nanoparticle, prepared 24 h in advance, was put a test tubes. Then, 1 cm monolithic rod was incorporated to the suspension. Finally, the test tubes were placed in oven at temperatures of 80°C for a 5-day period.

Method two. A mix of reducing reagent suspension (peels of lemon extract) alongside solution of $AgNO_3$ or $HAuCl_4$ in the ratio of 1:2 was put in test tubes. Afterwards, a monolithic rod of 1 cm was incorporated to the suspension. Finally, the test tubes were placed in oven at temperatures of 80°C for a 5-day period.

MONOLITHIC MATERIAL CHARACTERISATION

Visual observation and UV-vis. spectra analysis. The ion reduction into nanoparticles is mainly accompanied by a visible change in colour and NPs formation[34]. In view of this, the colour was observed to determine NP formation. The absorption of the resultant solutions was tracked through UV-vis. spectrophotometrically on the ranges of 350–800 nm at 1 nm in terms of resolution.

SEM-EDX-AFM analysis. The morphologies for dried monoliths were classified through scanning electron microscopy (SEM). Images were realised with an increasing voltage of 20 kV alongside a probe current of 100 pA under high vacuum modes. The chemical composition of the monolithic components prior to and after the modification of the monolith surface was analysed using Energy dispersive X-ray (EDX). High-resolution atomic force microscopy (AFM) was employed for testing the topological and morphological characteristics (Veeco-di Innova Model-2009-AFM-USA). Tapping non-contacting modes were utilised. For accurate mapping of surface topologies, AFM-raw data was placed onto the Origin-Lab version 6-USA program to produce accurate visualisations of the 3D surfaces of the samples under study.

PROTEIN EXTRACTION

The organic monoliths were put in Eppendorf tubes (0.5 ml) as home-spin columns. The monolith preparation in spin was undertaken using Nakamoto et al.[35] method with some few modifications. Scheme 1 recaps the steps used for loading monolithic components within the homemade spin columns.

Scheme 1
Steps of loading monolithic materials in home-made spin column using a centrifuge

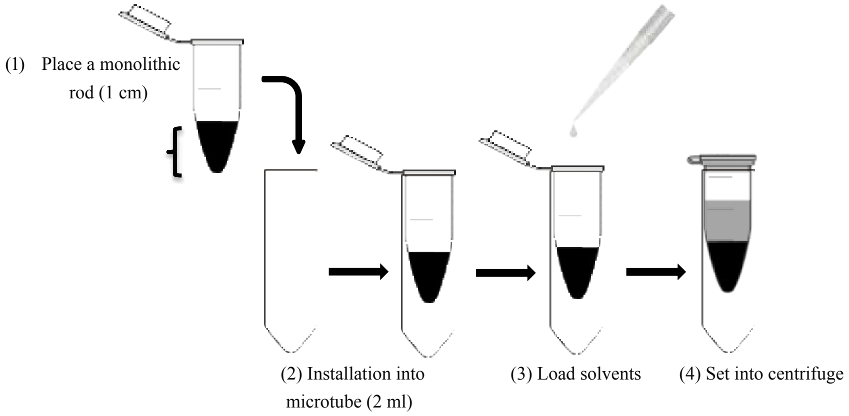

After the stationary phase, organic monolithic underwent fabrication and its performance verified with pepsin. The protein (60 µM) was immersed in a buffer suspension of 10 mM ammonium acetate (pH 9.3). All experiments were conducted at ambient temperature of about 23ºC. Separation of the protein specimen and the solutions was done using the centrifuge at velocities of 200 rpm at a duration of 2 min for all steps save for the use of the specimen step that took 5 min. To compute the extraction efficiency of all proteins, individual extraction of the proteins was undertaken. The organic polymeric monoliths underwent activation with 20 µl of acetonitrile (ACN), whereas the solvent was dismissed. Later, it was equilibrated using 200 µl of 10 mM ammonium acetate buffer suspension (pH 9.3), which was rejected. 300 µl made of the protein specimen was loaded and, the elution conducted using 150 µl 20% ACN with 0.1% trifluoroacetic acid (TFA), centrifuged, and then gathered in Eppendorf tubes (1.5 ml). Scheme 2 summarises the steps that feature in the purification of protein using the fabricated immobilised organic monolith metal NPs.

Scheme 2
Summary of the handling procedures for protein purification with assist of centrifuge

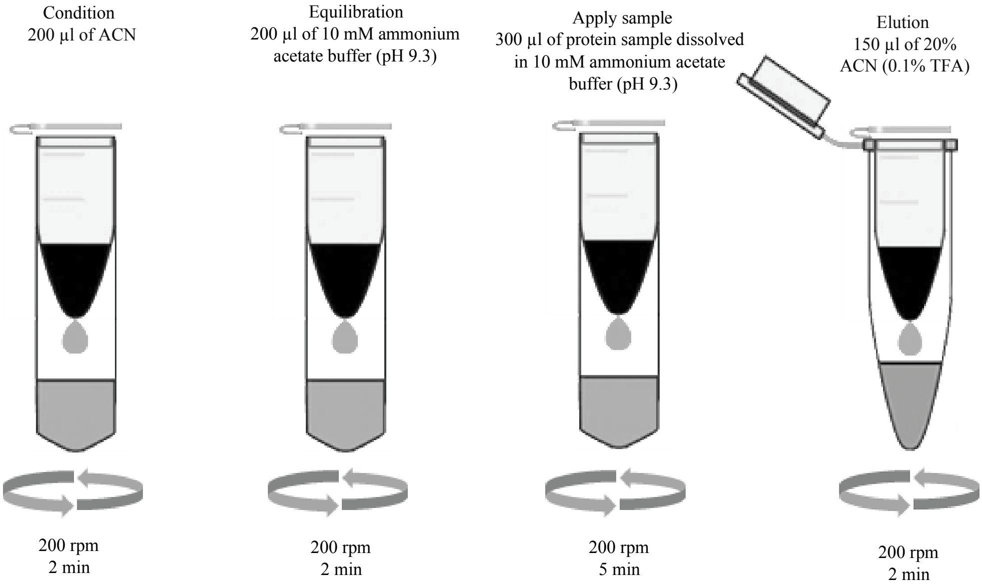

A specimen of the eluent was placed directly into the HPLC-UV detector to determine the proteins peak point and contrast them to the peak points of protein standard suspensions to compute the extraction efficiency. The mobile stage constituted acetonitrile-water (50:50) within the existence of 0.1% trifluoroacetic acid (TFA) in isocratic conditions. The wavelength of the detection was modified to 210 nm, whereas the injection volume was 20 ml (Ref. 36). To assess the efficiency of protein extraction, the extraction recovery (ER) was computed with equation (1) (Refs 37–39) that was considered the overall protein percentage obtained from the eluent:

$$\mathrm{ER} = \left[\frac{C_{\mathrm{elu}} \times V_{\mathrm{elu}}}{C_0 \times V_0}\right] \times 100, \qquad (1)$$

where C_{elu} and C_0 were derived from the peak point using the solid phase extraction and in the absence of purification, and V_{elu} and V_0 constitute the eluent volumes and solution of the sample.

RESULTS AND DISCUSSION

NPs immobilisation on organic polymer monoliths. Polymer monoliths improved using nanoparticles (NPs) integrate high specific NP surface area properties with the monoliths different surface chemistry and high porosity. In view of this, they have discovered extensive use in different fields that include sample treatment, electrocatalysis, and chromatography. Notably, nanomaterial-functionalised porous polymer monoliths have drawn significant attention from investigators[40,41]. In the current study, a methacrylate-based monolith (BuMA-*co*-EDMA) was selected for the organic polymer-based monolith because this was extensively used[42].

Monolithic rods underwent coating with nanoparticles two different approaches. The first featured the insertion of organic monolithic rods within NP solutions prior to placement within an 80°C oven. The second involved a mix of reducing reagents (peels of lemon extraction) using $AgNO_3$ suspension as the source of silver or $HAuCl_4$ suspension as the source of gold followed by addition of monolithic rods prior to placement in test tube in an 80°C oven. Any change in the solutions colour was observed with naked eyes, as illustrated in Fig. 1. The nanoparticle suspension solution that was SNPs suspension solution (Fig. 1*a*), or GNPs suspension solution (Fig. 1*b*), was put in test tubes that had the organic monolithic rods. As illustrated, the solution of NPs had a dark colour. After 5 days, the colour intensity of the solution decreased because of the organic monolithic rod nanoparticle coating, whereas the organic monolithic rod colour shifted to dark colour. In the second technique, the source of ion that assumed the form of $AgNO_3$ solution (Fig.1*c*), or a $HAuCl_4$ solution (Fig. 1*d*), was mixed using reducing reagent (peels of lemon extract) and put in test tubes, which contained organic monolithic rods. The solution of ion source changed to a darker colour because of metallic NP formation. The colour intensity then reduced as the metallic nanoparticle coated the monolithic components.

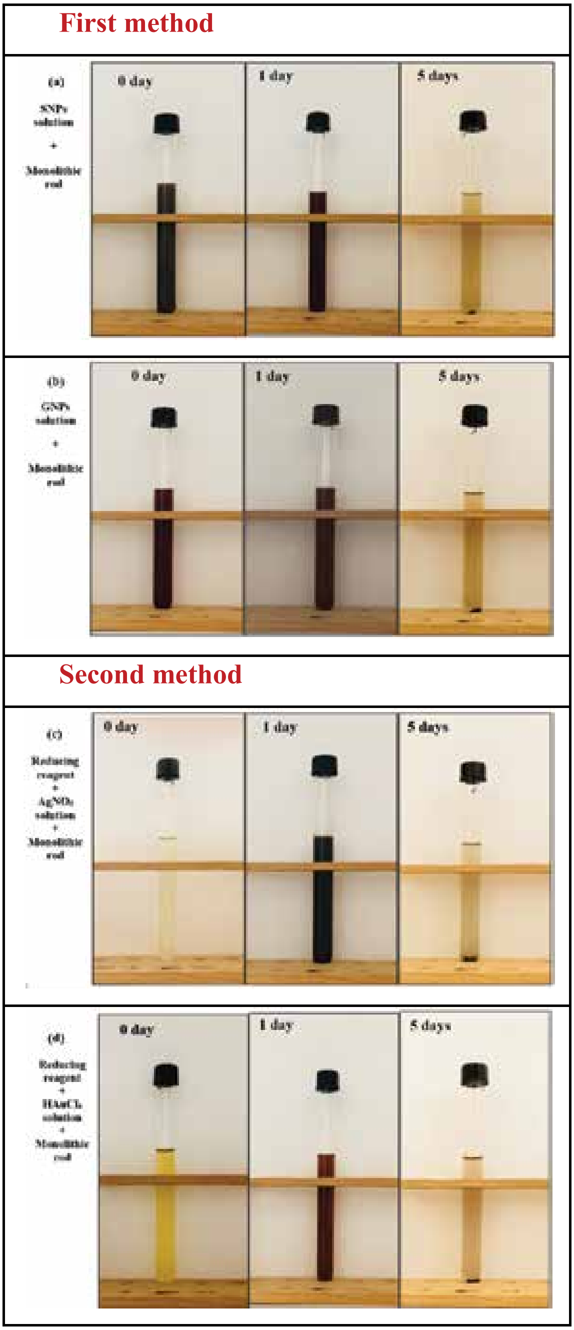

Fig. 1. Coating of organic monolithic rods with NPs using the first and second methods (the first method involved placing the monolithic rod in SNPs suspension – *a* and GNPs suspension – *b*, while the second method involved placing the monolithic rod in a mixture of ion source solution ($AgNO_3$ solution – *c* or $HAuCl_4$ solution – *d*) and reducing reagent (lemon peel extract)

The NP solution absorption spectra were recorded to determine the NP immobilisation progress on the organic monolithic component over 350–800 nm range. Figure 2*a* illustrates the SNPs UV-vis. spectra solution prior to and following NP immobilisation on the organic monolithic component. The SNPs solution featured the absorbance peak of about 2.0 a.u., the organic monolithic rods were incorporated to the solution and measurement of the mixture absorbance was taken one day later. The results showed that there was decrease in the absorbance peak with a shift of 1.3 a.u. After incubation of the organic monolithic rod within the SNP solution for a 5-day period, no additional absorbance was witnessed as the SNPs had shifted to the organic material surface. Figure 2*b* illustrates the UV spectrum of the GNPs suspension whereas the peak of absorbance peak was at 1.8 a.u. The peak of absorbance reduced to 1.47 a.u. and finally vanished after five-day incubation period with the organic monolithic rods.

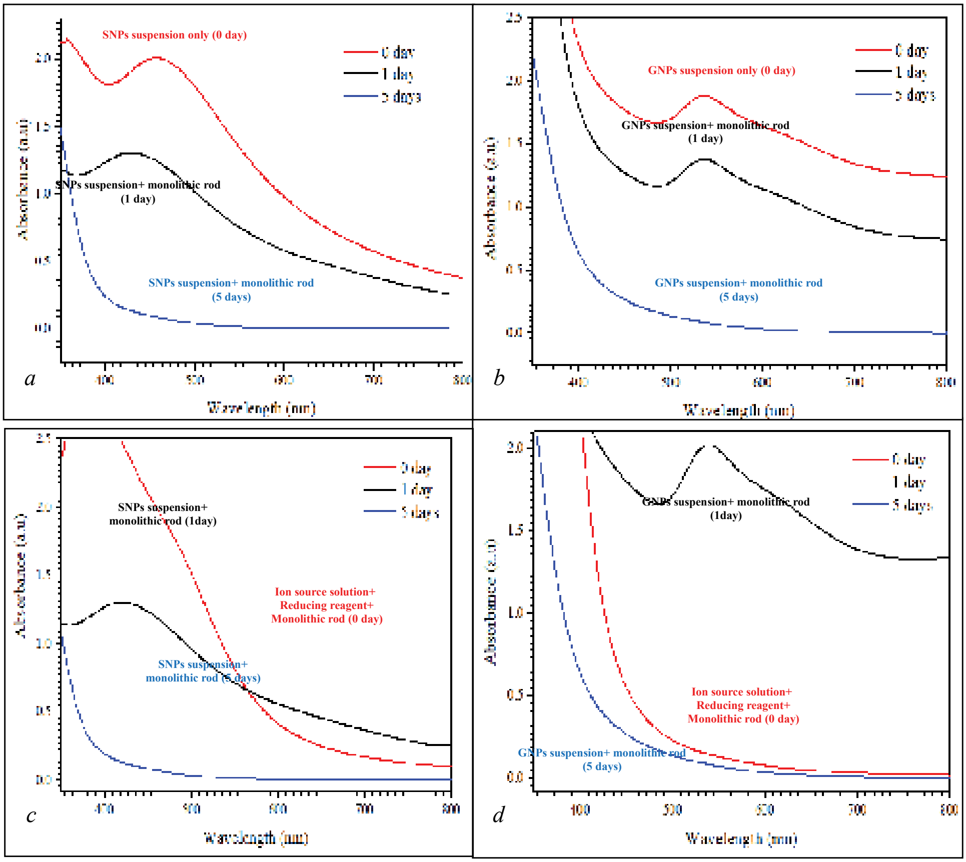

Fig. 2. UV-vis. absorption spectra of solution prepared using first and second methods (the first method involved placing the monolithic rod in SNPs suspension – *a* and GNPs suspension – *b*, while the second method involved placing the monolithic rod in a mixture of ion source solution ($AgNO_3$ solution – *c* or $HAuCl_4$ solution – *d*) and reducing reagent (lemon peel extract)

Figures 2*c* and *d* illustrate the solutions spectra after implementation of the second technique. The results show the absence of absorbance peak for the mixture consists of reducing reagent and the solution of ion source. The progress characterising the formation of nanoparticles was checked in 1 day mixing the sources of ion with the reducing reagents in organic monolithic rod presence. The UV-vis. spectra indicated the absence of absorption bands due to the NP transverse plasmon resonance. After 5 days, there were no peaks for the formed nanoparticle solution, showing the completion of NPs immobilisation process on polymer monoliths.

Figure 3 illustrates the organic monolithic rod surface colour prior to and following NP immobilisation through the first and second techniques. The bare organic-oriented monolith was white. Following NP immobilisation on the monolithic component surface, it changed to a dark colour because of high NP concentration, homogeneous NP distribution, alongside non-cracking. This proved that the nanoparticles had moved to the organic monolithic material surface.

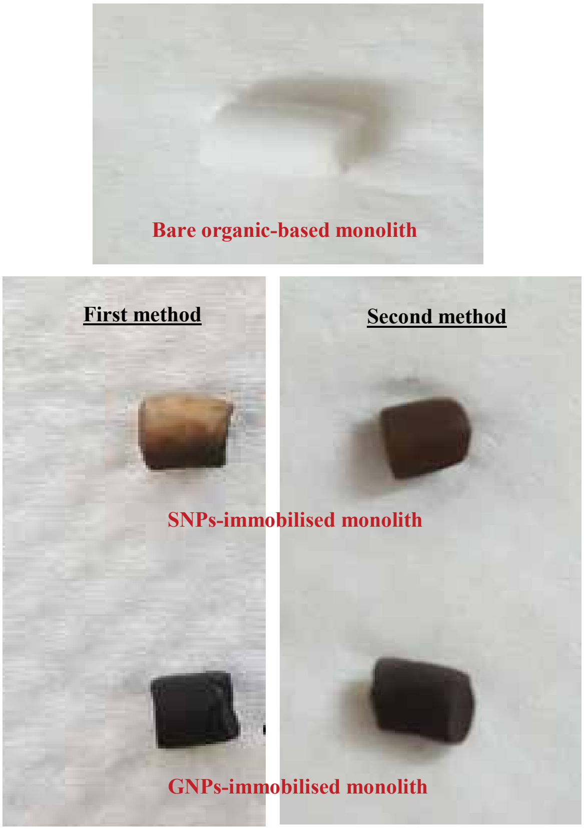

Fig. 3. Colour changes of monolith before and after the process of immobilisation of NPs using first and second methods

It was imperative to confirm homogeneity on the overall fabricated monolithic component surface area; in view of this, the fabricated organic monolithic rod was separated into three pieces (bottom, middle, top). Figure 4 illustrates the images of the organic monolith cross-section following the introduction of the NPs using methods one and two. The results showed that GNP immobilisation on the organic monolithic components was better compared to that of SNPs because the internal part of the SNP-immobilised monolith showed lighter colour, while the GNPs-immobilised monolith colour was homogenous and darker. Besides, the second technique seemed to efficiently facilitate NP immobilisation to the organic monolith surface because the monolithic cross section colour (bottom, middle, and top) was homogeneous and darker as opposed to the monolithic components prepared using the first technique.

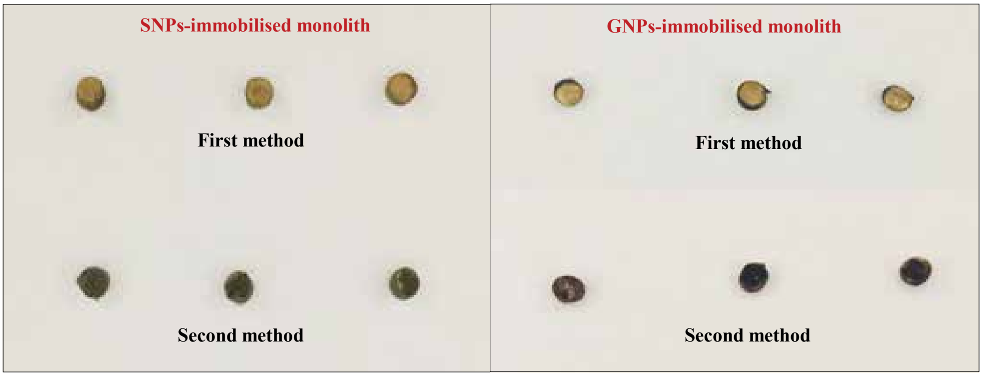

Fig. 4. Organic monolithic rod that was divided into three cross-sections (top, middle, and bottom) after immobilisation with NPs

Characterisations of fabricated materials. The polymeric monoliths morphologies were examined through SEM analysis, as illustrated in Fig. 5. In general, the surface of all specimens were crack-free, smooth, and uniform, and the porous structure resembled that seen in previous studies[43,44]. In addition, it was found that the SEM of bare organic-based monoliths a suitable pore structure was detected that showed a homogeneous interrelated macro-porous network with open pores. The SEM of SNPs-immobilised monolith alongside GNPs-immobilised monolith proved the suitable pore surface coverage with nanoparticles that the nanoparticles had spherical shapes. Similar results were obtained in Refs 45–48. Additionally, the results showed that there were variations in the fabricated monolithic material morphologies coated using NPs irrespective of whether the second or first method was used.

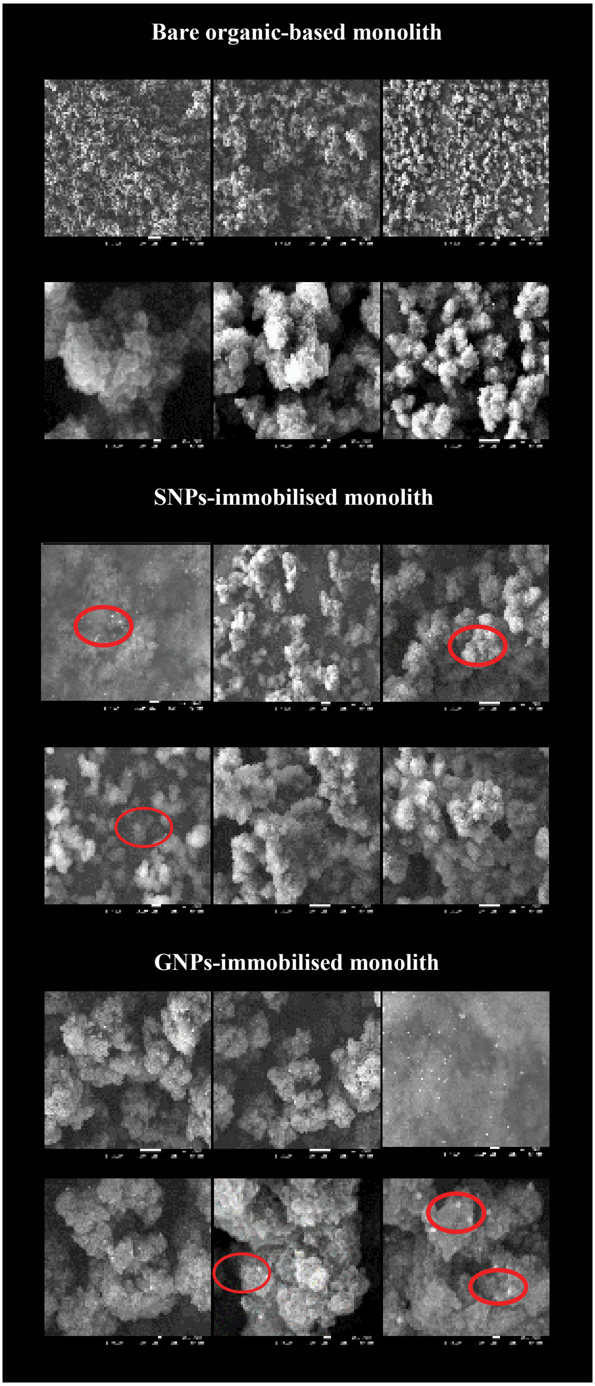

Fig. 5. Scanning electron micrographs showing the surface morphology of bare organic monolith, SNPs-immobilised monolith, and GNPs-immobilised monolith

EDX analysis was used for investigating the fabricated monolithic materials chemical composition illustrated in Fig. 6. The results indicated that the major elements of bare organic-based monoliths included oxygen (O) and carbon (C). After the immobilisation of SNPs on the organic monolith surface with the second or first method, besides oxygen and carbon, a new optimum point in Ag was identified, as illustrated by the increasing Ag peak intensity. In the scenario for the first technique, oxygen and carbon peaks were identified with Au pattern showing a new peak. Regarding the second technique, there was increased Au peak intensity.

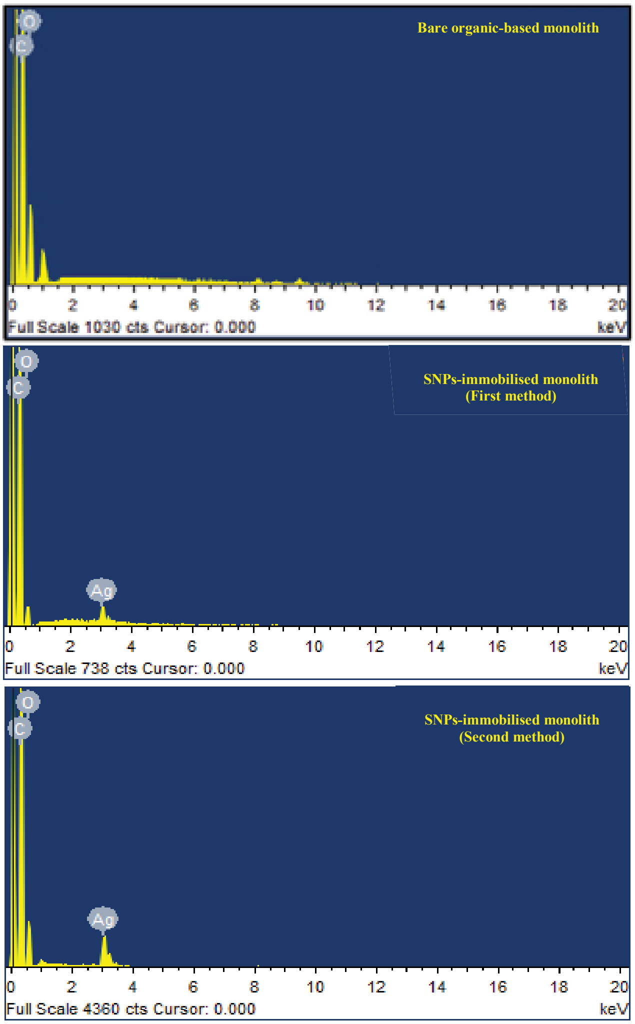

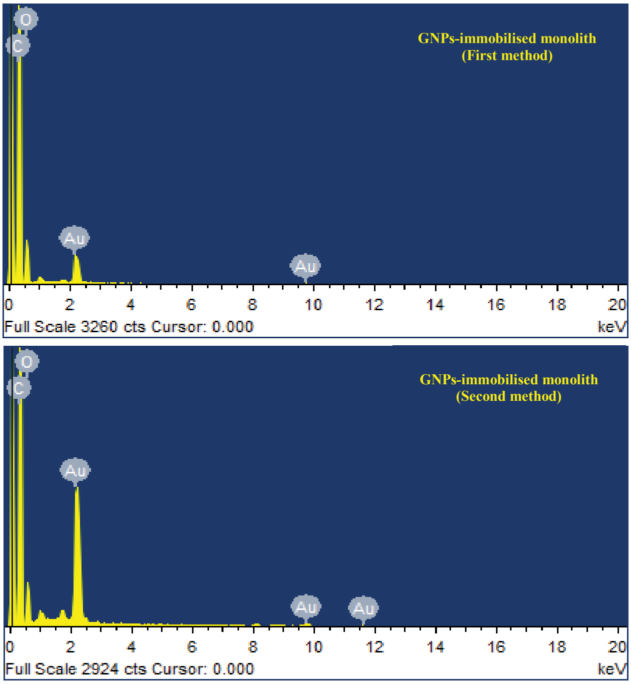

Fig. 6. EDX images of the bare organic-based monolith, SNPs-immobilised monolith, and GNPs-immobilised monolith using first and second methods

Table 1 recaps the data relating to the fabricated material chemical composition, which were studied through EDX analysis. The bare organic-based monolith comprised of 37.99% O and 62.01% C. After employing the first technique for SNPs immobilisation, carbon was 85.28%, oxygen was 13.49%, whereas silver was 1.23%. After applying the second technique for organic monolith immobilisation, the SNP organic monoliths, silver was 1.92%, oxygen was 24.35%, and carbon was 73.73%. Employing the first technique for GNP immobilisation on the organic monolithic material surface led to 19.64% oxygen, 79.58% carbon alongside a new peak in gold pattern that had gold atom 0.78%. In contrast, applying the second technique for GNP immobilisation on the organic monolith material surface resulted in new gold pattern peak with gold atom 2.83%, 13.60% oxygen and 83.57% carbon. The EDX analysis results show that the second technique constituted the most efficient technique for NP immobilisation on the organic monolithic material surface.

Table 1. Composition components of bare organic monolith, SNPs-immobilised monolith, and GNPs-immobilised monolith

Element	Bare organic-based monolith	SNPs-immobilised monolith		GNPs-immobilised monolith	
		first method	second method	first method	second method
C	68.49	85.28	73.73	79.58	83.57
O	31.51	13.49	24.35	19.64	13.60
Ag	0.00	1.23	1.92	0.00	0.00
Au	0.00	0.00	0.00	0.78	2.83
Totals	100.00	100.00	100.00	100.00	100.00

The surface characteristics of coated metallic NPs were examined through AFM, because AFM investigation offers quantitative and qualitative information regarding the scanned particles height. Table 2 provides 3D AFM images for fabricated polymer monoliths prior to and following immobilisation as derived through the AFM method.

Table 2. Particle size of organic monolith before and after immobilisation of NPs using AFM technique

Type of monolith	3D-AFM-micrograph	Roughness (nm)
Bare organic monolith	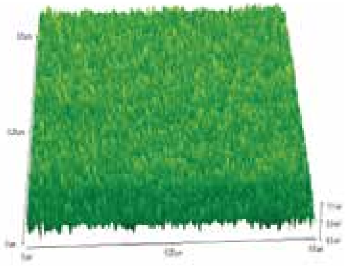	17–36
SNPs-immobilised monolith	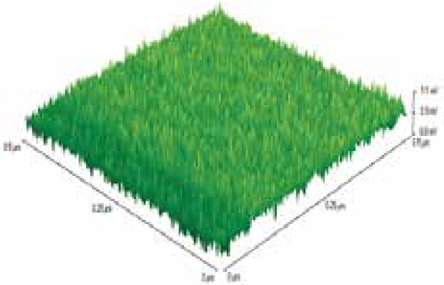	19–38
GNPs-immobilised monolith		21–43

The bare monolith flat surface was uniform and smooth whereas the roughness of the surface ranged between 17 and 36 nm. The 3D AFM image of the SNPs immobilisation revealed that the roughness of the surface increased slightly to 19–38 nm while, after GNP immobilisation to the monolithic component, the roughness of the surface roughness increased and ranged between 21 and 43 nm. The 3D AFM results proved the NP immobilisation with organic monoliths. Based upon the classification of fabricated components, it could be inferred that the second method efficiently immobilised NP monolithic materials compared to the first technique; in view of this, the second technique was used for NP monolithic materials.

Performance for protein purification. Sample preparation constitutes a crucial step within analytical protocols. Because of their significant surface-to-volume ratio, nanoparticles have in recent years been considered efficient affinity probes for SPE (Ref. 30). Following monolithic material fabrication (GNPs immobilised organic monolith, SNPs immobilised organic monolith, and bare organic monolith), they were utilised as SPE sorbents for pepsin enrichment (the source being gastric mucosa, 66463 Da, $pI = 4.7$).

Monolithic spin columns, a latest inclusion to SPE products, were chosen for this role as they can accelerate sample preparation velocity and accommodate tiny volumes of samples[31]. The extraction of samples followed four steps as illustrated in the procedure within Scheme 2 that featured protein elution, sorbent equilibration and activation, and sample solution loading through Eman Alzahrani method[32] with minor modifications. Firstly, the monolith was activated with 200 µl of ACN, and then equilibrated with 200 µl of 10 mM ammonium acetate buffer solution (pH 9.3), then 300 µl the sample solution were loaded. Finally, the extracted protein was eluted from the fabricated organic polymer monolith using 150 µl of 20% ACN (0.1 % TFA) solution as an eluting solution. All solutions and the protein samples were separated using the centrifuge at speed of 200 rpm within 2 min for all steps except apply sample step takes 5 min.

After preconcentration of the standard protein, the performance of the fabricated polymer monolith was checked using the HPLC-UV detector by comparing the peak area of each protein before and after preconcentration. Figure 7 shows the UV chromatogram for the eluent solution of pepsin, which shows a comparison of the peaks area of pepsin before preconcentration (*a*), and after preconcentration using bare organic monolith (*b*), SNPs-immobilised organic monolith (*c*), and GNPs-immobilised organic monolith (*d*). The standard protein investigated for comparison of the performance of bare organic monolith, immobilised monolith with GNPs and immobilised monolith with SNPs. From the figures, it can be seen that a difference in the peak height of protein with bare monolith compared with the monolith with NPs. As a result, the sensitivity of the analysis was enhanced, when using monolith immobilised with NPs. In addition, the performance of GNPs immobilised monolith was better than that of SNPs immobilised monolith.

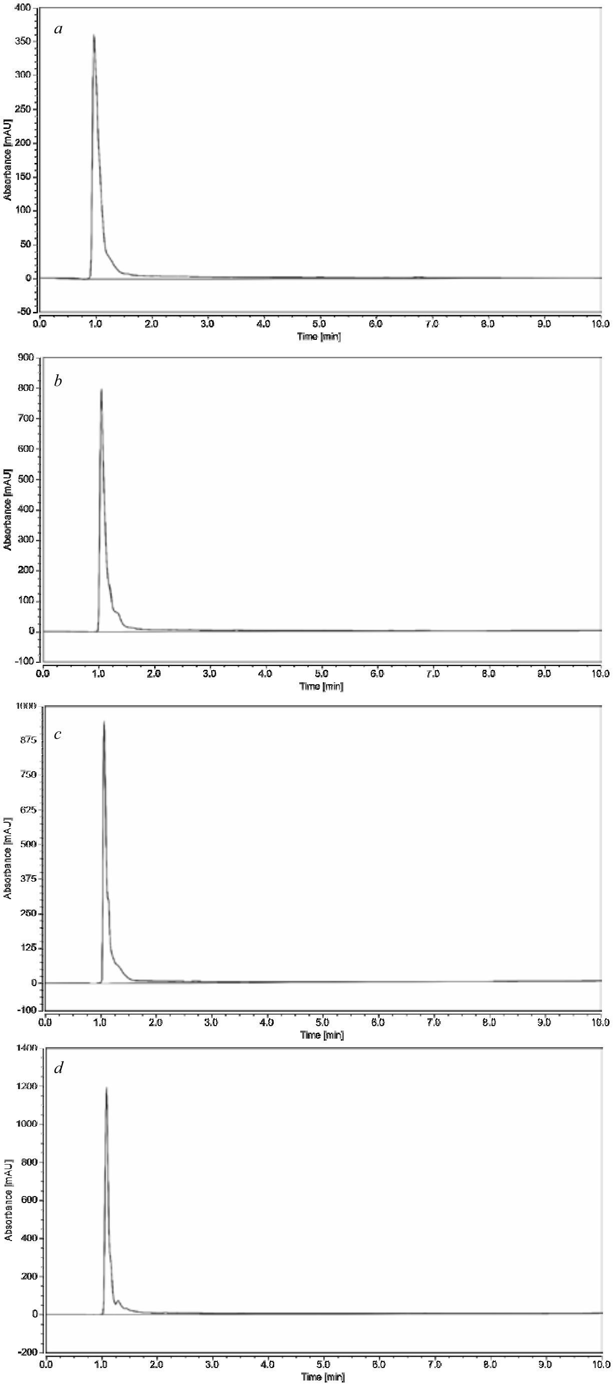

Fig. 7. Difference in the peak areas of pepsin before preconcentration – *a*, and after preconcentration using the bare organic-based monolith – *b*, SNPs-immobilised organic monolith – *c*, and GNPs-immobilised organic monolith – *d*

As can be seen in Fig. 8, the extraction recoveries of the standard protein was calculated and it was found that the extraction recovery of pepsin using bare organic-based monolith was 84.6%, which were less than the extraction recoveries of the same proteins using organic monolith coated with NPs. In addition, it was found that the extraction recovery of pepsin using organic monolith coated with GNPs (99.8%) has higher than the extraction recovery of the same protein using organic monolith coated with SNPs (87.5%), and it is similar to other study published in Refs 46, 49 and 50. The results obtained from this investigation showed that the procedure to preconcentrate pepsin was reproducible since good run-to-run reproducibility was achieved with RSD value was less than 5%.

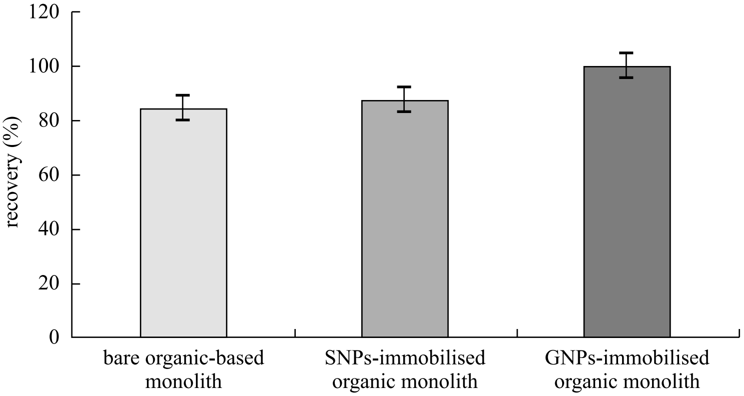

Fig. 8. Comparison of the extraction recovery of pepsin using bare organic-based monolith, SNPs-immobilised organic monolith, and GNPs-immobilised organic monolith

CONCLUSIONS

This project sought to fabricate organic monolithic materials within home-made spin columns for application in extraction of protein samples as the means for accessing the benefits of reduced analysis time, contamination, and specimen handling. The technique tested used green chemistry methods to prepare metal NPs because they were considered environmental-friendly, readily available and safe. Two techniques of NP immobilisation on organic-based monoliths underwent testing during the study, and overall, it was found that the second technique was more efficient compared to the first one for NP immobilisation on monolithic material surfaces. The use of optimised monolithic components in a process of protein extraction was studied. The results showed that organic monoliths modified using NPs had better performance compared to bare organic-based monoliths.

REFERENCES

1. G. GUIOCHON: Monolithic Columns in High-performance Liquid Chromatography. J Chromatogr A, **1168** (1–2), 101 (2007).
2. F. SVEC, C. G. HUBER: Monolithic Materials: Promises, Challenges, Achievements. ACS Publications, 2006.
3. J. WANG et al.: One-pot Preparation of an Organic Polymer Monolith by Thiolene Click Chemistry for Capillary Electrochromatography. J Separ Sci, **40** (15), 3144 (2017).
4. A. KABIR, K. G. FURTON, A. MALIK: Innovations in Sol-Gel Microextraction Phases for Solvent-free Sample Preparation in Analytical Chemistry. TrAC Trends in Analytical Chemistry, **45**, 197 (2013).
5. T. ZHU, K. H. ROW: Preparation and Applications of Hybrid Organic–Inorganic Monoliths: a Review. J Separ Sci, **35** (10–11), 1294 (2012).
6. F. ALVES, P. SCHOLDER, I. NISCHANG: Conceptual Design of Large Surface Area Porous Polymeric Hybrid Media Based on Polyhedral Oligomeric Silsesquioxane Precursors: Preparation, Tailoring of Porous Properties, and Internal Surface Functionalization. ACS Appl Mater Inter, **5** (7), 2517 (2013).
7. F. SVEC: Porous Polymer Monoliths: Amazingly Wide Variety of Techniques Enabling Their Preparation. J Chromatogr A, **1217** (6), 902 (2010).
8. Q. CAO et al.: Polymer Monoliths with Exchangeable Chemistries: Use of Gold Nanoparticles as Intermediate Ligands for Capillary Columns with Varying Surface Functionalities. Anal Chem, **82** (17), 7416 (2010).
9. N. ISHIZUKA et al.: Performance of a Monolithic Silica Column in a Capillary Under Pressure-driven and Electrodriven Conditions. Anal Chem, **72** (6), 1275 (2000).
10. M. IACONO, D. CONNOLLY, A. HEISE: Fabrication of a GMA-co-EDMA Monolith in a 2.0 mm id Polypropylene Housing. Materials, **9** (4), 263 (2016).
11. N. ISHIZUKA et al.: Monolithic Silica Columns for High-efficiency Separations by High-performance Liquid Chromatography. J Chromatogr A, **960** (1-2), 85 (2002).
12. J. C. MASINI: Semi-micro Reversed-phase Liquid Chromatography for the Separation of Alkyl Benzenes and Proteins Exploiting Methacrylate-and Polystyrene-based Monolithic Columns. J Sep Sci, **39** (9), 1648 (2016).
13. C. LV et al.: Covalent Attachment of Polymeric Monolith to Polyether Ether Ketone (PEEK) Tubing. Anal Chim Acta, **932**, 114 (2016).
14. S. SHU et al.: Chemical Anchoring of Lauryl Methacrylate-based Reversed Phase Monolith to 1/16 ″od Polyetheretherketone Tubing. J Chromatogr A, **1242**, 59 (2012).
15. J. C. MASINI: Separation of Proteins by Cation-exchange Sequential Injection Chromatography Using a Polymeric Monolithic Column. Anal Bioanal Chem, **408** (5), 1445 (2016).
16. F. SVEC, Y. LV: Advances and Recent Trends in the Field of Monolithic Columns for Chromatography. Anal Chem, **87** (1), 250 (2014).
17. J. KRENKOVA, F. FORET: Iron Oxide Nanoparticle Coating of Organic Polymer-based Monolithic Columns for Phosphopeptide Enrichment. J Sep Sci, **34** (16-17), 2106 (2011).
18. S. CURRIVAN, P. JANDERA: Post-polymerization Modifications of Polymeric Monolithic Columns: a Review. Chromatography, **1** (1), 24. (2014).
19. A. ZHANG et al.: Screening α-glucosidase Inhibitor from Natural Products by Capillary Electrophoresis with Immobilised Enzyme onto Polymer Monolith Modified by Gold Nanoparticles. Food Chem, **141** (3), 1854 (2013).
20. R. J. GROARKE, D. BRABAZON: Methacrylate Polymer Monoliths for Separation Applications. Materials, **9 (6)**, 446 (2016).
21. Z. WALSH et al.: Photoinitiated Polymerisation of Monolithic Stationary Phases in Polyimide Coated Capillaries Using Visible Region LEDs. Chem Commun, (48), 6504 (2008).

22. Z.-H. WEI et al.: Imprinted Monoliths: Recent Significant Progress in Analysis Field. TrAC Trends in Analytical Chemistry, **86**, 84 (2017).
23. Z. WALSH et al.: Polymerisation and Surface Modification of Methacrylate Monoliths in Polyimide Channels and Polyimide Coated Capillaries Using 660 nm Light Emitting Diodes. J Chromatogr A, **1218** (20), 2954 (2011).
24. M. AHMED et al.: Single-walled Carbon Nanotube-based Polymer Monoliths for the Enantioselective Nano-Liquid Chromatographic Separation of Racemic Pharmaceuticals. J Chromatogr A, **1360**, 100 (2014).
25. E. J. CARRASCO-CORREA et al.: Incorporation of Zeolitic Imidazolate Framework (ZIF-8)-derived Nanoporous Carbons in Methacrylate Polymeric Monoliths for Capillary Electrochromatography. Talanta, **164**, 348 (2017).
26. N. GANEWATTA, Z. El RASSI: Monolithic Capillary Columns Consisting of Poly (Glycidyl Methacrylate-co-Ethylene Glycol Dimethacrylate) and Their Diol Derivatives with Incorporated Hydroxyl Functionalized Multiwalled Carbon Nanotubes for Reversed-phase Capillary Electrochromatography. Analyst, **143** (1), 270 (2018).
27. X. DING, J. YANG, Y. DONG: Advancements in the Preparation of High-performance Liquid Chromatographic Organic Polymer Monoliths for the Separation of Small-molecule Drugs. Journal of Pharmaceutical Analysis, 2018.
28. W. HU et al.: Applications of Nanoparticle-modified Stationary Phases in Capillary Electrochromatography. TrAC Trends in Analytical Chemistry, **61**, 29 (2014).
29. J. KRENKOVA, F. FORET, F. SVEC: Less Common Applications of Monoliths: V. Monolithic Scaffolds Modified with Nanostructures for Chromatographic Separations and Tissue Engineering. J Sep Sci, **35** (10–11), 1266 (2012).
30. S. PONARULSELVAM, et al.: Synthesis of Silver Nanoparticles Using Leaves of *Catharanthus roseus* Linn. G. Don and Their Antiplasmodial Activities. Asian Pac J Trop Med, **2** (7), 574 (2012).
31. D. R. BUNCH, S. WANG: Applications of Monolithic Solid-phase Extraction in Chromatography-based Clinical Chemistry Assays. Anal Bioanal Chem, **405** (10), 3021 (2013).
32. E. S. ALZAHRANI: Investigation of Monolithic Materials for Protein Sample Preparation. University of Hull, 2012.
33. O. S. AYSHA, S. N. NAJIMU: Biosynthesis of Silver Nanoparticles, Using *Citrus limon* (LINN.) Burm. F. Peel Extract and Its Antibacterial Property against Selected Urinary Tract Pathogens. J Bio Sci Opi, **2** (3), 248 (2014).
34. E. ALZAHRANI, K. WELHAM: Optimization Preparation of the Biosynthesis of Silver Nanoparticles Using Watermelon and Study of Itsantibacterial Activity. Int J Basic Appl Sci, **3** (4), 392 (2014).
35. A. NAKAMOTO et al.: Monolithic Silica Spin Column Extraction and Simultaneous Derivatization of Amphetamines and 3,4-Methylenedioxyamphetamines in Human Urine for Gas Chromatographic-Mass Spectrometric Detection. Anal Chim Acta, **661** (1), 42 (2010).
36. E. ALZAHRANI, K. WELHAM: Design and Evaluation of Synthetic Silica-based Monolithic Materials in Shrinkable Tube for Efficient Protein Extraction. Analyst, **136** (20), 4321 (2011).
37. D. NAGARAJU, S.-D. HUANG: Determination of Triazine Herbicides in Aqueous Samples by Dispersive Liquid–Liquid Microextraction with Gas Chromatography–Ion Trap Mass Spectrometry. J Chromatogr A, **1161** (1), 89 (2007).
38. M. REZAEE et al.: Determination of Organic Compounds in Water Using Dispersive Liquid–Liquid Microextraction. J Chromatogr A, **1116** (1), 1 (2006).
39. S. BERIJANI et al.: Dispersive Liquid–Liquid Microextraction Combined with Gas Chromatography-Flame Photometric Detection: Very Simple, Rapid and Sensitive Method for the Determination of Organophosphorus Pesticides in Water. J Chromatogr A, **1123** (1), 1 (2006).
40. S. TONG et al.: Recent Advances of Polymer Monolithic Columns Functionalized with Micro/ Nanomaterials: Synthesis and Application. Chromatographia, **77** (1–2), 5 (2014).
41. J. C. MASINI,. F. SVEK: Porous Monoliths for On-line Sample Preparation: a Review. Anal Chim Acta, 2017.

42. F.-Y. LIN, W.-Y. CHEN, M. T. HEARN: Microcalorimetric Studies on the Interaction Mechanism between Proteins and Hydrophobic Solid Surfaces in Hydrophobic Interaction Chromatography: Effects of Salts, Hydrophobicity of the Sorbent, and Structure of the Protein. Anal Chem, **73** (16), 3875 (2001).
43. S.-H. CHUAG et al.: Accelerated Colourimetric Immunosensing Using Surface-modified Porous Monoliths and Gold Nanoparticles. Sci Technol Adv Mat, **14** (4), 044403 (2013).
44. N. GANEWATTA: Organic Polymer-based Monolithic Stationary Phases with Incorporated Nanostructured Materials for HPLC and CEC. Electrophoresis, **39** (1), 53 (2018).
45. M. VERGARA-BARBERÁN et al.: Solid-phase Extraction Based on Ground Methacrylate Monolith Modified with Gold Nanoparticles for Isolation of Proteins. Analytica Chim Acta, **917**, 37 (2016).
46. D. GRZYWIŃSKI, M. SZUMSKI, B. BUSZEWSKI: Polymer Monoliths with Silver Nanoparticles-Cholesterol Conjugate as Stationary Phases for Capillary Liquid Chromatography. J Chromatogr A, **1526**, 93 (2017).
47. Y. LV et al.: Preparation of Porous Polymer Monoliths Featuring Enhanced Surface Coverage with Gold Nanoparticles. J Chromatogr A, **1261**, 121 (2012).
48. O. SEDLACEK et al.: Silver-coated Monolithic Columns for Separation in Radiopharmaceutical Applications. J Separation Sci, **37** (7), 798 (2014).
49. C. ACQUAH et al.: Nano-doped monolithic Materials for Molecular Separation. Separations, **4** (1), 2 (2017).
50. M. VERGARA-BARBERÁN et al.: Polymeric Sorbents Modified with Gold and Silver Nanoparticles for Solid-phase Extraction of Proteins Followed by MALDI-TOF Analysis. Microchim Acta, **184** (6), 1683 (2017).

Received 30 March 2019
Revised 9 April 2019

Oxidation Communications 42, No 2, 230–236 (2019)

Technological aspects of oxidation processes, computer application

EXPERIMENTAL DETERMINATION OF MASS TRANSFER COEFFICIENT BY RECTIFICATION IN A LABORATORY COLUMN EQUIPPED WITH THREE SIEVE TRAYS

A. GEORGIEVA, ZH. IVANOV*, K. PANAYOTOVA

Department of Chemical Engineering, 'Prof. Dr. Asen Zlatarov' University,
1 Prof. Yakimov Street, 8010 Burgas, Bulgaria
E-mail: *adrianaslavova@yahoo.com*; *zh_ivanov@btu.bg*;
krasi_panayotova@btu.bg

ABSTRACT

One of the main problems with tray rectification units is the kinetic studies of their mass transfer which are complicated due to the difficulties in the determination of the interphase boundary formed by the dispersion of the vapour phase in the liquid on the tray, the mass transfer coefficient, as well as the mixing of the liquid by its movement on the tray and the presence of impurities in the separated mixtures. Many efforts have been devoted to this problem in recent years. The present paper is a contribution in this field. The influence of the kinetic coefficients by rectification of the binary system methanol-water under complete mixing of the liquid phase and regime of ideal shift of the vapour phase was studied. To approximate these idealised models of the motion of the two phases, the experiments were carried out in a specially manufactured small scale laboratory column equipped with three sieve trays.

Keywords: mass transfer coefficient, tray units, determination, laboratory column.

AIMS AND BACKGROUND

On world scale, one of the main processes in chemical and petroleum industries for separation of organic mixtures aiming to obtain the individual components with high purity is the process of rectification. The rectification process is carried out mainly in tray columns and sometimes in packed columns. The mass exchange between the vapour and liquid phases takes place on the arranged at certain distances contact elements (trays). Their role is to ensure the formation of developed interphase boundary between the contacting vapour and liquid phases. The interphase surface is created

---

* For correspondence.

by the bubbling of the vapour through the liquid and has active dynamic character as it changes by shape and size during the process.

In bubbling columns, the mass transfer from the gaseous to the liquid phase is a key parameter of the process. Classically, the gas is released as small bubbles so effective mass transfer takes place between the vapour and liquid phases. To improve the transfer efficiency, it is necessary to control both the interphase boundary and the mass transfer coefficient. Since one of the main problems of the tray rectification units is the kinetic study of the mass exchange, which are complicated due to the difficulties in the determination of the interphase area, the present paper is contribution in this field. The use of the volume mass transfer coefficient for analysis of the processes is hampered by the fact that it is product of the mass transfer coefficient and the specific interphase area. The kinetic coefficients allow analysing and comparing the newly designed units and they are used during their design and control[1–7]. In extreme cases, it is necessary to increase the partial mass transfer coefficient of the limiting phase to intensify the overall process of mass transfer. This is usually achieved by increasing the flow velocity although it is always accompanied by increase of the hydraulic resistances.

EXPERIMENTAL

The process of mass transfer in the vapour-liquid systems is a complex field in chemical engineering, both on industrial and laboratory scale. In the first case, this process is carried out on special equipment where it is very difficult to predict its behaviour with theoretical models only[8–10]. For this reason, it is necessary to estimate the coefficients of mass transfer and the interphase area on laboratory scale. Since the interphase surface in tray columns, which is actually the real geometric surface of the vapour-liquid layer, is dynamic system, it is quite hard to determine. This is why the estimations are made using the specific interphase surface, i.e. the interphase area per unit working volume of the vapour-liquid layer.

The aim of the present work is to determine the values of the mass transfer coefficient in the vapour phase for the model mixture methanol-water using experimental data. For this purpose, experimental data obtained from laboratory equipment including a glass laboratory column with 0.1 m diameter and three sieve trays were used. Each tray has 50 holes with diameter of 0.003 m. All the experimental data were obtained at vapour velocity in the column 0.12–0.36 m/s, under atmospheric pressure and full phlegm[11].

The model suggested for determination of the mass transfer coefficient in the vapour phase involves determination of the ratio between the volume mass transfer coefficient obtained from experimental data and the specific interphase area calculated from the dependence[11–14]:

$$K_{OG} = (K_{OG}\,a)^{\exp}/a,$$

where K_{OG} is the gas-side mass transfer coefficient (m s^{-1}); $K_{OG}a$ – the overal mass transfer coefficient (kmol/m^3 s); a – the specific interfacial mass transfer area (m^2/m^3).

Since the experimental determination of the total volume mass transfer coefficient by vapour phase has dimension kmol/m^3 s, the mass transfer coefficient by vapour phase is calculated with dimension kmol/m^2 s while it should have dimension m/s, it is necessary to multiply the mass transfer coefficient by vapour phase with the expression M_{CM}/ρ_G to adjust to the proper dimension, i.e.:

$$(K_{OG})^{\exp} = \frac{K_{OG} M_{CM}}{\rho_G}, \tag{1}$$

where M_{CM} is the molecular weight (kg/kmol) and ρ_G – the gas density (kg m^{-3}).

The value of the volume mass transfer coefficient, which gives the quantity of substance transferred between the two phases in unit working volume per unit driving force, was determined by the following formula[15]:

$$(K_{OG}\, a)^{\exp} = \frac{u_G N_{OG}}{h_f M}, \tag{2}$$

where u_G is the vapour phase velocity (m/s); N_{OG} – the number of overall vapour phase transfer units; h_f – the froth height (m), where the relationship between the number of transferred units and the local efficiency coefficient is given by the dependence[16]:

$$N_{OG} = -\ln (1 - E_{OG}), \tag{3}$$

where E_{OG} is the Murphree vapour-phase point efficiency.

More than 60 experiments were carried out under conditions of full mixing of the liquid on the tray, i.e. the composition of the flow was constant and equal to the composition of the outgoing flow at complete shift of the vapour phase which suggests that the rate of diffusion of the particles in the flow direction and against it was significantly smaller than the velocity of the flow shift and the local efficiency coefficient can be calculated by the formula[17]:

$$E_{OG} = \frac{y_n - y_{n-1}}{y^* - y_{n-1}}, \tag{4}$$

where y_n is the local vapour phase concentration mole fraction for n-trays (kmol/kmol); y_{n-1} – the local vapour phase concentration mole fraction for $n-1$ trays (kmol/kmol); y^* – the vapour phase concentration mole fraction in liquid with liquid phase concentration (kmol/kmol).

According to the penetration model of Higbie, beside the mass transfer at the boundary layer, substantial influence exerts the refreshment of the surface due to the turbulent pulsations which incessantly bring in fresh portions of fluid from the core to the interphase zone and back. All vortices have the same contact time. The specific interphase area can be determined by the formula[9,18]:

$$a = \frac{u_G N_{OG}}{h_f}\left(\frac{1}{\beta_G} + \frac{m}{\beta_L}\right), \tag{5}$$

where m is the slope of vapour-liquid equilibrium line; β_G – the vapour-phase mass transfer unit; β_L – the liquid-phase mass transfer unit, where the partial coefficients of mass transfer in the vapour and liquid phases at equal contact times can be determined using equations (6) and (7):

$$\beta_G = \left(\frac{4D_G}{\pi\theta_G}\right)^{1/2}, \tag{6}$$

$$\beta_L = \left(\frac{4D_L}{\pi\theta_L}\right)^{1/2}, \tag{7}$$

where D_G is the molecular diffusion coefficients for vapour phase (m^2/s); D_L – the molecular diffusion coefficients for liquid phase (m^2/s); θ_G – the contact time in vapour phase (s); θ_L – the contact time in liquid phase (s).

The contact time characteristic for the period of presence of microscopic quantities of the given phase on the interphase surface as a whole is unknown quantity but can be adequately described by the model suggested by Chen and Chuang. For sieve trays they suggest the following relationship for determination of the contact time for both vapour and liquid phases[19]:

$$\theta_G = h_L/u_G \tag{8}$$

$$\theta_L = \theta_G\, \rho_G/\rho_L. \tag{9}$$

The height of the light liquid is an important parameter because it directly affects the contact time and can be calculated by dependence suggested in the literature[13]:

$$h_L = 0.6\, h_w^{0.5} p^{0.25} ((\rho_G/\rho_L)^{0.5}/b)^{0.25}, \tag{10}$$

where h_L is the clear liquid height (m); h_w – the outlet weir height (m); p – the pitch of holes in sieve tray, (m); b – the weir length per unit bubbling area (m^{-1}).

Using equations (11) and (12), the values of the coefficient of molecular diffusion can be determined which is necessary for the calculation of the partial coefficients of mass transfer for vapour and liquid phases, respectively[20]:

$$D_G = \frac{(4.3 \times 10^{-7})\, T^{2/3}}{p(\upsilon_A^{1/3} + \upsilon_B^{1/3})^2}\left(\frac{1}{M_A} + \frac{1}{M_B}\right)^{1/2} \tag{11}$$

$$D_L = \frac{K\, M_B^{1/2}\, T}{\mu_B\, (\upsilon_A \upsilon_B)}, \tag{12}$$

where μ is the liquid viscosity (Pa s); υ – the molar volumes of pure components (cm^3/mol); T – temperature (°C).

RESULTS AND DISCUSSION

Under conditions of complete mixing of the liquid on the tray according to equation (1), the data obtained were processed as dependence of the mass transfer coefficient in the vapour phase on the *F*-factor of load by vapour phase, as well as on the visual observations on the height of the vapour-liquid layer.

Figure 1 shows the dependence of the mass transfer coefficient in the vapour phase as function of the load factor by vapour phase for the model mixture methanol-water.

It can be seen from the figure that the mass transfer coefficient in the vapour phase increased its value in the range 0.022–0.044 m/s with the increase of vapour velocity in the column, respectively the *F*-factor of load by vapour phase from 0.12–0.38 (kg/m) 0.5 s^{-1}.

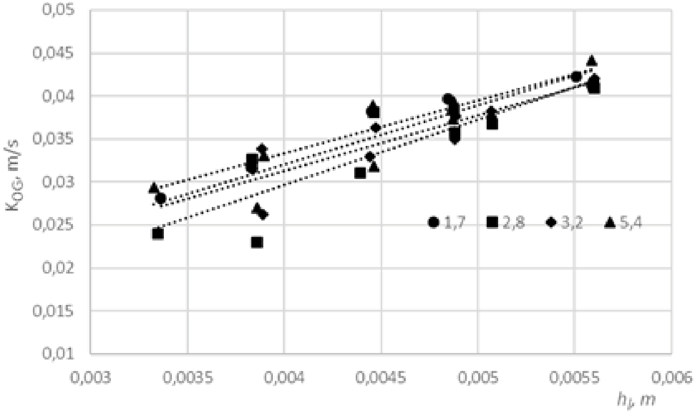

Fig. 1. Mass transfer coefficient in vapour phase as function of the *F*-factor of load by vapour phase

The influence of the height of the vapour-liquid layer is illustrated in Fig. 2.

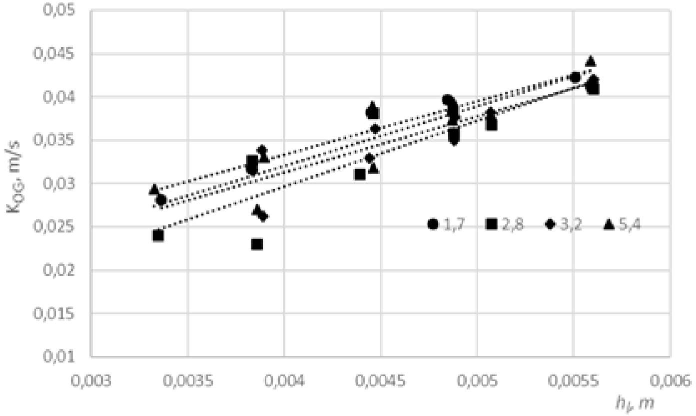

Fig. 2. Mass transfer coefficient in vapour phase as function of the height of the vapour-liquid layer

The increase of the vapour-liquid layer height leads to increase of the value of the specific interphase area for the whole interval of concentrations. At values of the height of the vapour-liquid layer about 0.0055 m, the mass transfer coefficient has the highest values of about 0.0044 m/s.

CONCLUSIONS

For the model mixture methanol-water, under conditions of full mixing of the liquid on the tray and complete shifting of the vapour phase in the height of the two-phase layer and using the method suggested above for determination of the mass transfer coefficient in the vapour phase, the following conclusions can be made:

1. For the vapour phase, the vapour velocity in the column, the *F*-factor of load, the number of transferred units and the volume mass transfer coefficient were determined.
2. For the whole concentration interval studied, the mass transfer coefficient in the vapour phase increases with the value of the *F*-factor of load by the vapour phase, and, respectively, the vapour velocity in the column.
3. For the whole concentration interval, the mass transfer coefficient in the vapour phase increases with the height of the vapour-liquid layer.

REFERENCES

1. S. NEDELCHEV, U. JORDAN: A New Correction Factor for Theoretical Prediction of Mass Transfer Coefficients in Bubble Columns. J Chem Eng Jpn, **39,** 1237 (2006).
2. Zh. TASSEV, P. PETROV, Zh. STEFANOV: Zum Einflus der Flussigkeitseigenschaften auf die Phasengrenzflashe bei Zweiphasenschichten an Kolonnenboden. Chem Ing Tech, **61**, 412 (1989).
3. Zh. STEFANOV, Zh. TASEV: Interfacial Surface of a Ductile Valve Tray with Thugs. Annual Assen Zlatarov University, **XVI**, 165 (1981).
4. J. WANG, Y. LENG, H. SHAO, W. LI, Ch. HUANG: Prediction of Gas-Liquid Interfacial Area in Valve Trays. AIChE J, **00**, 1 (2005).
5. A. BANDYOPADHYAY, M. N. BISWAS: Determination of Interfacial Area in a Tapered Bubble Column. J Chem Techn Biotechn, **86**, 1211 (2011).
6. S. AFERKA, P. MARCHOT, M. CRINE, D. TOYE: Interfacial Area Measurement in a Catalytic Distillation Packing Using High Energy X-ray CT. Chem Eng Sci, **65**, 511 (2010).
7. J. HAIDLA, F.J. REJLA, L. VALENZA, M. KORDAČA, T. MOUCHAA, L. LABÍKA, M. SCHULTESB: Absorption in Wetted-wall Column with Phase Properties Close to Distillation Conditions. Chem Eng Sci, **144**, 126 (2006).
8. P. V. DANCKWERTS: Significance of Liquid-Film Coefficients in Gas Absorption. Ind Eng Chem, **43**, 1460 (1951).
9. R. HIGBIE: The Rate of Absorption of a Pure Gas into a Still Liquid during Short Periods of Exposure. Trans A. I. Ch. E., **31**, 365 (1935).
10. W. G. WHITMAN: The Two-film Theory of Gas Absorption. Chem Metall Eng, **29**, 147 (1923).
11. R. KUTSAROV, I. CHOBANOV: On Mass Transfer Coefficient of Volatile Organic Compounds in Open-air Water Basins at Calm. Oxid Commun, **34** (4), 957 (2011).
12. Zh. IVANOV, A. GEORGIEVA, K. PANAYOTOVA, Determination of Interphase Surface by Rectification Process in a Laboratory Column. Oxid Commun, **41**, 365 (2018).
13. D. RADEV, D. Chr. GENCHEV, Zh. STEFANOV: Investigation of Hydrodynamic and Mass transfer of Sieve Tray by Distillation. Science & Technologies, **I**, 24 (2011).

14. D. RADEV, Zh. STEFANOV, Zh. IVANOV: A New Method to Predict Interfacial Mass Transfer Area in Distillation Column with Sieve Tray. Science & Technologies, **III**, 31 (2013).
15. Zh. STEFANOV, Zh. IVANOV: Correlation between Mass Transfer Coeffcient and Surface Tension in Seive Tray Distillation Laboratory Column. Asian Chem Lett, **14**, 83 (2010).
16. D. KOLEVA, M. KARAIVANOVA, Zh. STEFANOV, Ch. GENCHEV: Modeling Efficiency of Distillation Laboratory Column. Science & Technologies, **III**, 115 (2013).
17. M. KARAIVANOVA, A. GEORGIEVA, D. KOLEVA, Effect of Physicochemical Propertes of the Separated Mixtures on the Local Efficiency by Rectification. Science & Technologies, **II**, 26 (2012).
18. M. KARAIVANOVA, A. GEORGIEVA, Zh. STEFANOV: Phase Resistances in Rectification. Proceedings of University of Ruse, **51**, 186 (2012).
19. G. X. CHEN, K. T. CHUANG, Prediction of Point Efficiency for Sieve Trays in Distillation. Ind Eng Chem Res, **32**, 701 (1993).
20. Zh. TASEV, D. MITEV, R. KUCAROV, Zh. STEFANOV, D. VARBANOV, Hr. GENCHEV, R. RASHEV: Course Guide for Processes and Apparatus in the Chemical Industry. VHTI-Burgas, 1986.

Received 26 February 2019
Revised 9 March 2019

Oxidation Communications 42, No 2, 237–248 (2019)

Technological aspects of oxidation processes, computer application

HIGH SPEED AND LOW COMPLEXITY SEGMENTED FINITE IMPULSE RESPONSE (FIR) FILTER DESIGN USING VARIABLE SIZE PARTITIONING RADIX-2^r BASED MCM

L. MOHANA KANNAN[a]*, D. DEEPA[b]

[a]*Anna University, Chennai, Tamil Nadu, India*
E-mail: *mohancalls2018@gmail.com*
[b]*Bannari Amman Institute of Technology, Sathyamangalam, Tamil Nadu, India*

ABSTRACT

This paper proposes a high speed and low complexity Segmented finite impulse response (FIR) filter using Variable size partitioning and Radix-2^r based MCM (VPRM). These variable size partitioning is classified into minimum size, optimum size and maximum size. The reason behind this partitioning approach is complexity reduction. For further reducing the computational complexity, the N bit input is segmented into N/2 bit inputs and then it is applied to Radix-2^r based MCM for partial product formation. These are obtained by performing the common sub sharing technique among the adjacent coefficients. The final output is the sum of shifted and zero appended output obtained from Partial product addition (PPA) block. The proposed Segmented FIR filter is designed and simulated in Xilinx ISE 14.2. The proposed Segmented FIR filter reduces the memory usage by 27.2, 25.96, 25.66, and 34.09% and energy consumption by 76.39, 75.74, 69.94, and 40.82% when compared with previous FIR filter designs such as FIR filter, FIR IPC, FIR IPC with pipelined CSA and FIR with Radix-2^r based MCM.

Keywords: MCM, Variable size partioning, Radix-2^r, PPA.

AIMS AND BACKGROUND

Filter design satisfies a set of requirements such as frequency function, phase shift or group delay, impulse response, causality, stability, locality, computational complexity and implementation in particular hardware or software. The commonly used digital filters in DSP systems are Infinite impulse response (IIR) and Finite impulse response (FIR) filters[1]. In this, FIR filter is stable and IIR filter is unstable. FIR filter depends only on Input where as IIR filter depends upon both Input and Output. FIR filter consists of only zeroes and IIR filter consists of both poles and zeroes[2]. IIR is a

---

[*] For correspondence.

property applying to many linear Time-Invariant systems. IIR filters usually require fewer coefficients to execute similar filtering operations but it has the disadvantage of nonlinear phase response. Because of this disadvantage of IIR filter, FIR filter is most commonly preferred. FIR filters have the advantages of Bounded-Input-Bounded-Output stability, phase linearity and low coefficient sensitivity[3]. Digital FIR filters are widely used in communication, biomedical, image area and audio signal processing applications for eliminating spectral leakage, reducing channel width and eliminating interference. Since many design problems can be cast as optimisation problems, classical numerical analysis and optimisation techniques have been successfully applied to achieve optimum designs[4]. The main aim of designing FIR filter is to minimise power consumption[5]. Power consumption can be minimised by reducing hardware complexity. The design methods of FIR filter are window method, frequency sampling method and optimum filter design[6]. Due to efficiency and simplicity of the FIR filter window method is used.

The output function of FIR filter can be expressed as follows:

$$y[n] = \sum_{k=0}^{N-1} h[k]\, x[n-k]$$

where $x[k]$ is the input of the FIR filter; $h[k]$ – the coefficient of FIR filter frequency response, and $y[n]$ – the output of the FIR filter.

FIR filter is also known as feedforward or non-recursive or transversal. FIR filters do not require feedback. FIR filter is usually implemented by using a series of delays, multipliers, and adders to create the filter output. The complexity of the FIR filter is dominated by the adders and coefficient multipliers. A delay element is a circuit that produces an output waveform similar to its input waveform, only delayed by a certain amount of time. Adder is a digital circuit that performs the XOR operation and adders serve as the basic components in the implementation of a FIR filter. A multiplier is an electronic circuit used in digital filters to multiply the binary numbers. Selecting multiplier with low power consumption leads to an efficient architecture. Accuracy in filter designing is based on the multiplication and accumulation of filter coefficients. Some applications, the FIR filter circuit must be able to operate at high sample rates[7]. Due to the property of linear phase, the signals of all frequencies are delayed by the same amount of time, thereby eliminating the possibility of phase distortion.

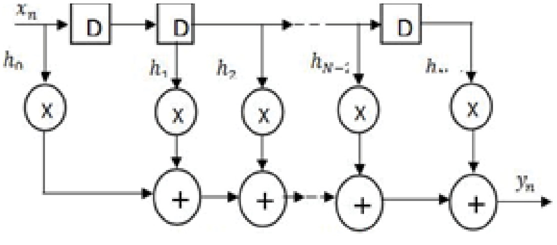

Fig. 1. Direct form FIR filter

A direct form FIR filter structure uses a delay element as shown in Fig. 1. We need N multipliers for an $(N–1)$-th order for FIR filter implementation. The advantage of using this method is to design a linear phase response and reduce the computational complexity.

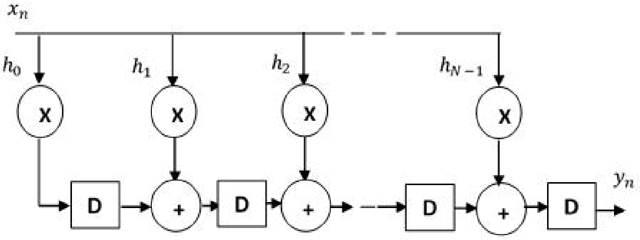

Fig. 2. Transposed form FIR filter

The transpose form FIR filter is to implement realisation of Finite impulse response (FIR) filter. The data flow graph (DFG) of transpose form FIR filter for N terms of length is shown in Fig. 2. The output of the filter can be expressed in mathematical form as follows:

$$y(n) = \sum_{i=0}^{N} h(i)\, x(n - i).$$

Aggarwal et al. proposed the design of digital FIR filter using evolutionary and swarm optimisation techniques. The advantage of this method is less execution time to achieve the optimum solution and the disadvantage is computational complexity due to fitness function evolution[1]. Ahmad proposed Rotation-based lattice ladder FIR filter based on circular buffer techniques. This technique increased the performance level up to 68.75% but it has the limitation of more execution time[8].

Judhisthir Dash et al. proposed the design of liner phase multi-band stop filter based on particle swarm optimisation. The merits of this method are the fitness function can be non-differentiable and the limitation is there is no general convergence theory applicable to practical and multidimensional problem[5]. Atul Kumar Dwivedi et al. proposed the design of FIR filter based on artificial bee colony algorithm. This method minimises the ripples and power loss. The disadvantage is Multiple sequence alignment (MSA) problem can be occurred between the sequences[9].

Aravind Illa et al. proposed the design of multiplier less FIR filter with fractional delay. The advantages of this method are reduction of implementation complexity and power dissipation. The limitation of this method is consuming more power and area of the filter[6]. Aimin Jiang et al. proposed the FIR filter design based on Iterative Second order cone programming (SOCP). The advantages of this method are providing better solution and applied to any optimisation task. The disadvantage is minimising the linear function over the interaction of an affine set[4].

Aimin Jiang et al. proposed sparse low pass FIR filters with optimised filter length. The advantages of this method are capable of automatically determining an appropriate filter order while improving the sparsity of a FIR filter. The limitation of this method is only focus on reducing the number of nonzero-coefficients[10]. Rajib Kar et al. proposed band stop FIR filter design based on Particle swarm optimisation algorithm. The advantages of this method are easy to implement and it needs fewer parameters. The disadvantages are its repeated searching process and it is limited to minimum error condition[11].

Jiajun Liang et al. proposed FIR filter design based on Multi Objective Cuckoo Search Algorithm. The advantage of this method is its ability to escape from local minimum error. The major drawback is that the initialisation process is based on forward selection to solve the problem of attributes reduction[12]. Yin Liu et al. proposed the FIR filter architecture based on stochastic logic. The advantage is minimum peak error value and limitation – the system is unstable regardless of the initialisation[7].

Vasundhara et al. proposed the design of FIR filter based on hybrid adaptive differential evolution with particle swarm optimisation. This method helps to reduce the design time and provided better magnitude response. The disadvantage is it does not automatically decide the controlling parameters[13]. Basant K. Mohanty et al. proposed the design of 2-D FIR filter based on Memory footprint reduction. This method is not affected by the implementation of inner-products but it is not applicable to all the systems[2].

Nithish Kumar et al. proposed the implementation of area and power efficient FIR filter based on modified MAC unit. Area and power reduction are achieved by this method but the processing capability is limited upto 32 bits (Ref. 14).

Abhijit Chandra et al. proposed the design of hardware efficient FIR Filter – a review of the state-of-the-art approaches. This method produces a high power and area consumption during implementation[3]. Oudjida et al. proposed radix-2^r arithmetic for multiplication by a constant. This technique achieves better compression ratio which yields less area and power consumption[15].

Oudjida et al. proposed multiple constant multiplication algorithm for high-speed and low-power design. The advantage of this method produces a shortest adder-depth in comparison with MCM algorithms. The disadvantage is that MCM algorithms can not compute with radix-2^r (Ref. 16).

Levent Aksoy et al. proposed exact and approximate algorithms for the filter design optimisation. This method achieves significant area delay and power dissipation. The limitation is to provide exact and approximate FDO algorithms[17].

Levent Aksoy et al. proposed search algorithm for the multiple constant multiplication problem – exact and approximate. The advantage of this method produces less computational resources for finding minimum solution. The disadvantage is that can not handle suboptimum solutions[18].

Rashmi patil et al.[19] proposed VLSI implementation of FIR filter for discrete wavelet transform. This method produces both power reduction, area or delay reduction of high level optimisation.

Sangram Patil et al.[20] proposed implementation of FIR filter using VLSI. The advantage is to enhance speed in response of FIR filter. The disadvantage of this method is less number of devices used in synthesis and simulation.

Xin Lou et al.[21] proposed novel structure for area-efficient implementation of FIR filters. The advantage of this method filter coefficients are grouped in symmetric impulse response of linear phase FIR filters. The disadvantage is to reduce performance of average area and power consumption.

Ye et al.[22] proposed design of low power multiplier less Linear-phase FIR filter. This technique provides better power savings of 19.6%.

EXPERIMENTAL

PROPOSED METHOD

Segmented FIR filter is proposed with Multiple Constant Multiplication (MCM) based on Radix-2^r and its block diagram is represented in Fig. 3. N bit input is applied for segmentation where the inputs are segmented as two N/2 bits to reduce the complexity of FIR filter. The segmented inputs are given to the Radix-2^r based MCM.

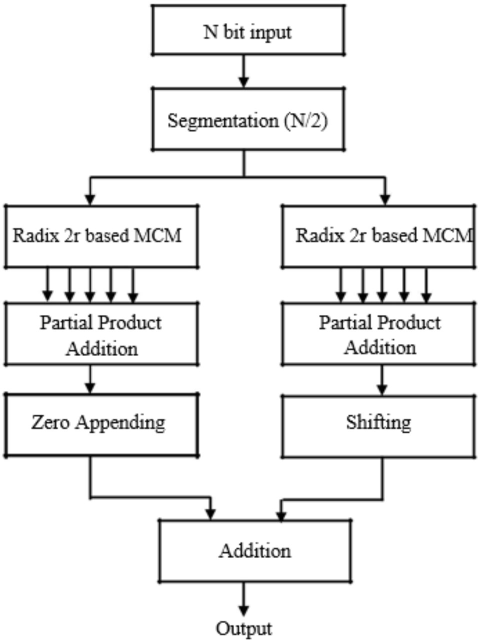

Fig. 3. Block diagram of segmented FIR filter

In this MCM block, the partial products are obtained by performing the multiplication of input signal with multiple coefficients and these coefficients are reused by sharing technique which reduces the utilisation of resources. Then it performs the addition of partial products. Appending of zeros and shifting are done in the result from the partial product addition block. Zero appended result is added with the shifted result to obtain the FIR filtered output.

RADIX-2^r BASED MCM

In this proposed technique, MCM is preferred over than Single constant multiplication (SCM), because it performs small additions which are separated by the delay elements leads to high speed architecture and it also shared the intermediate terms between the constants. The general structure of MCM is shown in Fig. 4.

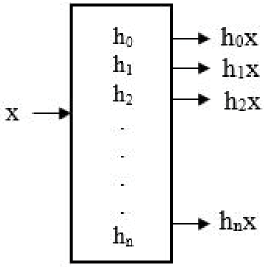

Fig. 4. General structure of MCM

The architecture of Variable size partitioning and Radix-2^r based MCM (VPRM) is depicted in Fig. 5. Variable size partitioning (VP) is preferred to overcome the limitations in Fixed size partitioning (FP) such as length of the partitioning parameter increased with the order of the filter, complexity of registers and large area occupation of adders. In VP approach an efficient partitioning approach is chosen as minimum size, optimum size and maximum size. If the bit size is less than 8-bit it is termed as minimum size partitioning, if the bit size is varied between 9 to 12-bit termed as optimal size partitioning otherwise called as maximum size partitioning. This partitioning approach reduces the complexity of adders and registers. It is mainly based on the sharing of common structures between the coefficients of filter.

Fig. 5. Architecture of VPRM

Radix-2^r is better than Cumulative Benefit Heuristic (Hcub) algorithm because Hcub increases the area for higher order filter. Radix 2^r arithmetic is exploited to minimise the number of additions used in MCM approach.

In Radix-2^r a nonnegative N-bit constant C is expressed as:

$$C = \sum_{j=0}^{(N+1)/(r-1)} (C_{rj-1} + 2^0 C_{rj} + 2^1 C_{rj+1} + 2^2 C_{rj+2} + \ldots + 2^{r-2} C_{rj+r-2} - 2^{r-1} C_{rj+r-1}) \times 2^{rj} \quad (1)$$

$$C = \sum_{j=0}^{(N+1)/(r-1)} Q_j \times 2^{rj}. \quad (2)$$

We assume that r is a divider of $N+1$. In equation (2), the two complement representation of C is split into $[(N + 1)/r]$ slices (Q_j), each of $r+1$-bit length (Ref. 16). Each pair of two contiguous slices has one overlapping bit. A digit-set DS(2^r) can be expressed as:

$$Q_j \in \mathrm{DS}(2^r) = \{-2^{r-1}, -2^{r-1} + 1, \ldots, -1, 0, 1, \ldots, 2^{r-1} - 1, 2^{r-1}\} \quad (3)$$

The sign of the Q_j term is given by the C_{rj+r-1} bit and $|Q_j| = 2^{kj \times mj}$, with $kj \in \{0, 1, 2, \ldots, r-1\}$ and $mj \in \mathrm{OM}(2^r) \cup \{0, 1\}$, where $\mathrm{OM}(2^r) = \{3, 5, 7, \ldots, 2^{r-1} - 1)$. OM($2^r$) is the set of odd positive digits in radix – 2^r recoding, with $|\mathrm{OM}(2^r)| = 2^{r-2} - 1$. Oudjida et al.[11,13] proved an upper-limit for adder depth and it is equal to $[\log 2[(N + 1)/r]] + r - 2$ (where $r = 2W((N + 1)^{1/2} \log 2)/\log 2$ and W is the Lambert function and [0] – the ceiling function. For MCM the value of r becomes $r = 2W((X(N + 1))^{1/2} \log 2)/\log 2$, where X is the number of constants[11].

The sharing of the common structure among the neighbouring filter coefficients are done with the help of Radix-2^r and it is shown in Fig. 6. For example, if the coefficients are considered as odd coefficient set {1, 3, 5, 7, …, 27, 29, 31} the sharing is as follows:

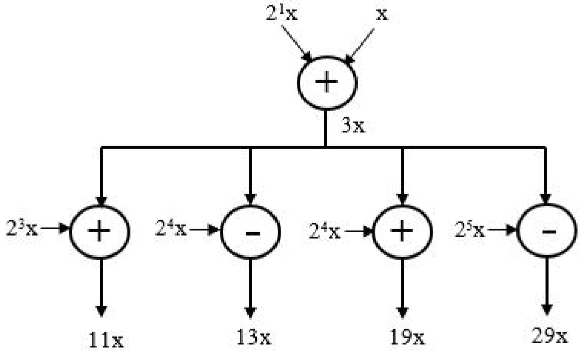

Fig. 6. Common sub sharing with 3×

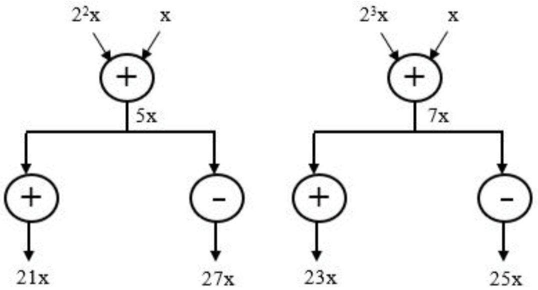

Fig. 7. Common sub sharing with 5× and 7×

The products 11x, 13x, 19x and 29x are obtained by common sub sharing approach with 3x and it is shown in Fig. 6. Similarly, Fig. 7 shows the products 21x, 27x and 23x, 25x by using common sub sharing approach with 5x and 7x.

Example for 16-bit input
Input = (1010 0101 1110 0110)2
= (42470)10
Segmented output S1 = (1010 0101)2
= (165)10
Segmented output S2 = (1110 0110)2
= (230)10
Let coefficients C1 = 3, C2 = 5, C3 = 7
MCM output PP1 = S1×C1
= (0001 1110 1111)2
= (495)10
PP2 = S1×C2
= (0011 0011 1001)2
= (825)10
PP3 = S1×C3
= (0100 1000 0011)2
= (1155)10
PPA1 = (1001 1010 1011)2 = (2475)10
PPA2 = (1101 0111 1010)2 = (3450)10
Appending zeros AZ = {PPA1, 8'b0}
Shifted PPA2 SP = {8'b0, PPA2}
FIR output = AZ + SP
= (1001 1011 1000 0111 1010)2
= (637050)10

RESULTS AND DISCUSSION

The Segmented FIR filter based on VPRM is synthesised and simulated using Xilinx ISE 14.2. It is synthesised in Kintex 7 device with package 7k70tfbg676. This architecture is coded in Verilog HDL and the proposed Segmented FIR filter performances are evaluated in terms of area, power consumption and delay.

Table 1. Area analysis of segmented FIR filter

Techniques	Number of slice registers	Number of slice LUTs
FIR filter	157	543
FIR with inner product cell (IPC)	135	578
FIR with IPC and pipelined CSA	148	530
FIR with Radix-2^r MCM	120	539
Segmented FIR with Radix-2^r based MCM	109	438

Table 1 shows that the analysis of area in terms of Number of slice registers and slice LUTs. From the comparison results, it is cleared that the proposed segmented FIR filter reduces the number of slice registers by 30.57, 19.25, 26.35, and 9.16% and slice LUTs by 19.33, 24.22, 17.35, and 18.73% when compared with previous FIR filter designs such as FIR filter, FIR IPC, FIR IPC with pipelined CSA and FIR with Radix-2^r based MCM.

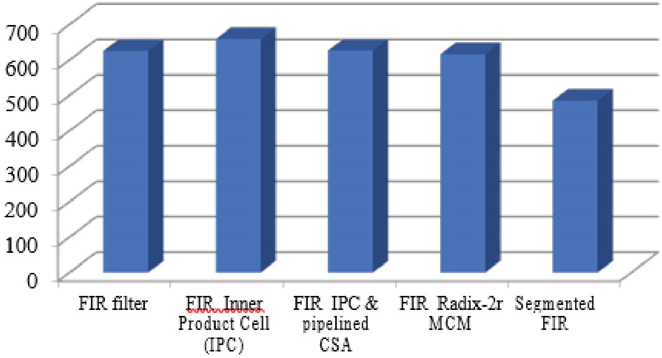

Fig. 8. Comparison chart of LUT Flip-flop utilisation

LUT flip-flop utilisation of various FIR filter designs is depicted in Fig. 8 and shows that the proposed segmented FIR filter reduces the number of LUT Flip-flop pairs by 22.4, 26.4, 22.5 and 21.26% when compared with previous FIR filter designs such as FIR filter, FIR IPC, FIR IPC with pipelined CSA and FIR with Radix-2^r based MCM.

Table 2. Power and delay analysis of segmented FIR filter

Techniques	Power (mW)	Delay (ns)
FIR filter	79	10.47
FIR with inner product cell (IPC)	69	10.25
FIR with IPC and pipelined CSA	76	10.19
FIR with Radix-2^r MCM	65	3.816
Segmented FIR with Radix-2^r based MCM	46	3.732

The performances are analysed in terms of delay, power consumption and it is shown in Table 2. When compared with FIR filter, FIR IPC, FIR IPC with pipelined CSA and FIR with Radix-2^r based MCM, the proposed Segmented FIR filter reduces the power consumption and delay by 41.77, 33.33, 39.47, and 29.23% and 64.35, 63.59, 63.37, and 8.4%, respectively.

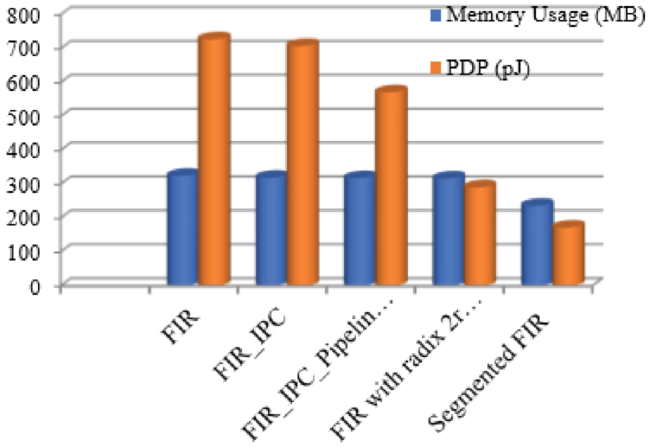

Fig. 9. Memory usage and energy consumption of various FIR filter design

FIR filter design using different techniques are evaluated in terms of memory usage and energy consumption and it is depicted in Fig. 9. The proposed segmented FIR filter reduces the memory usage by 27.2, 25.96, 25.66, and 34.09% and energy consumption by 76.39, 75.74, 69.94, and 40.82% when compared with previous FIR filter designs such as FIR filter, FIR IPC, FIR IPC with pipelined CSA and FIR with Radix-2^r based MCM.

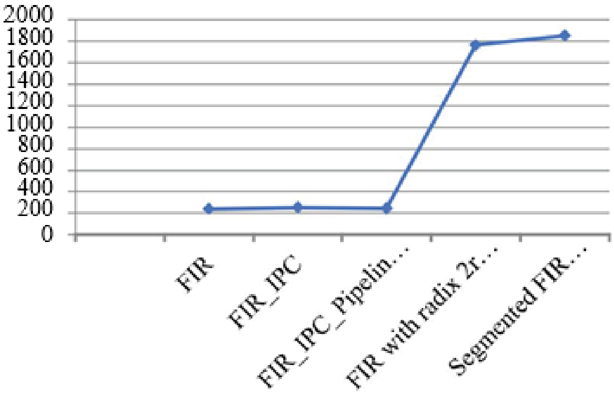

Fig. 10. Frequency of various FIR filter designs

Frequency of various FIR filter designs is compared and it is given in Fig. 10. From this, it is clear that the proposed segmented FIR filter has maximum frequency as 1853.24 MHz.

CONCLUSIONS

Radix-2^r is one of the best MCM approaches that achieved the better results in area, power, delay and complexity. The proposed segmented FIR filter is designed with Radix-2^r based MCM and the coefficients are segmented based on variable size partitioning parameter to reduce the complexity of the design. The common sub sharing technique is used in MCM based Radix-2r for an efficient resource utilisation. The proposed segmented FIR filter reduces the power consumption and delay by 41.77, 33.33, 39.47, and 29.23% and 64.35, 63.59, 63.37, and 8.4%, respectively when compared with FIR filter, FIR IPC, FIR IPC with pipelined CSA and FIR with Radix-2^r based MCM.

REFERENCES

1. APOORVA AGGARWAL, TARUN KUMAR RAWAT, DHARMENDRA KUMAR UPADHYAY: Design of Optimal Digital FIR Filters Using Evolutionary and Swarm Optimization Techniques. International Journal of Electronics and Communications (AEU), **70,** 373 (2016).
2. BASANT K. MOHANTY, PRAMOD K. MEHER, SOMAYA Al-MAADEED, ABBES AMIRA: Memory Footprint Reduction for Power-Efficient Realization of 2-D Finite Impulse Response Filters. IEEE T Circuits Syst, **61**, 120 (2014).
3. ABHIJIT CHANDRA, SUDIPTA CHATTOPADHYAY: Design of Hardware Efficient FIR Filter – a Review of the State-of-the-Art Approaches. International journal of Engineering Science and Technology, **19**, 212 (2016).
4. AIMIN JIANG, HON KEUNG KWAN, YANPING ZHU: Peak-Error-constrained Sparse FIR Filter Design Using Iterative SOCP. IEEE T Signal Proces, **60**, 4035 (2012).

5. JUDHISTHIR DASH, BIVAS DAM, RAJAKISHORE SWAIN: Optimal Design of Linear Phase Multi-Band Stop Filters using Improved Cuckoo Search Particle Swarm Optimization. J Appl Soft Comput, **52**, 435 (2017).
6. ARAVIND ILLA, NISHA HARIDAS, ELIZABETH ELIAS: Design of Multiplier-less FIR filters with Simultaneously Variable Bandwidth and Fractional Delay. International Journal of Engineering Science and Technology, **19**, 1160 (2016).
7. YIN LIU, KESHAB K PARHI: Linear-phase Lattice FIR Digital Filter Architectures Using Stochastic Logic. International Journal of Signal Processing Systems, **90**, 791 (2017).
8. A. S. ASIF AHMAD: VLSI Architectures for Givens Rotation based RLS Lattice Ladder FIR Filter Algorithms Using Circular Buffer Technique. In: Proceedings of the International Conference on Advances in Electronics, Computers and Communications(ICAECC), 2014.
9. ATUL KUMAR DWIVEDI, SUBHOJIT GHOSH, NARENDRA D. LONDHE: Low Power FIR Filter Design Using Modified Multi-objective Artificial Bee Colony Algorithm. Science Direct Engineering Applications of Artificial Intelligence, **55**, 58 (2016).
10. AIMIN JIANG, HON KEUNG KWAN, YANPING ZHU: Efficient Design of Sparse FIR Filters with Optimized Filter Length. In: Proceedings of the IEEE International Symposium on Circuits and Systems, 2014, p. 966.
11. RAJIB KAR, DURBADAL MANDAL, SANGEETA MONDAL, SAKTI PRASAD GHOSHAL: Craziness Based Particle Swarm Optimization Algorithm for FIR Band Stop Filter Design. International Journal of Swarm and Evolutionary Computation, **7**, 58 (2012).
12. JIAJUN LIANG, HON KEUNG KWAN: FIR Filter Design Using Multi Objective Cuckoo Search Algorithm. In: Proceedings of the IEEE Canadian conference on Electrical and Computer Engineering (CCECE), 2017.
13. VASUNDHARA, DURBADAL MANDAL, RAJIB KAR, SAKTI PRASAD GHOSHAL: Digital FIR Filter Design Using Fitness Based Hybrid Adaptive Differential Evolution with Particle Swarm Optimization. International Journal of Natural Computing, **13**, 55(2014).
14. V. NITHISH KUMAR, KOTESWARA RAO, G. LAKSHMINARAYANAN: Design of Area and Power Efficient Digital FIR Filter Using Modified MAC unit. In: Proceedings of the IEEE 2nd International Conference on Electronics and Communication System (ICESCS), 2015, p. 884 (2015).
15. A. K OUDJIDA, N. CHAI ILET: Radix-2^r Arithmetic for Multiplication by a Constant. IEEE T Circuits Syst – II, **61**, 349 (2014).
16. A. K OUDJIDA, AHMED LIACHA, MOHAMMED BAKIRI, NICOLAS CHAILLET: Multiple Constant Multiplication Algorithm for High-speed and Low-power Design. IEEE T Circuits Syst II, **63,** 176 (2016).
17. LEVENT AKSOY, PAULO FLORES: Exact and Approximate Algorithms for the Filter Design Optimization. IEEE Transaction on Signal Processing, **63**, 142 (2015).
18. LEVENT AKSOY, E. GUNES, P. FLORES: Search Algorithm for the Multiple Constant Multiplication Problem – Exact and Approximate. International Journal on Microprocessors Microsystems, **34**, 151 (2010).
19. RASHMI PATIL, M.T KOLTE: VLSI Implementation of FIR Filter for Discrete Wavelet Transform. International Journal of Advanced Research in Electrical, Electronics and Instrumentation Engineering, **4**, 81 (2015).
20. SANGRAM PATIL, PRITHVIRAJ PATIL, INDRAJIT PATIL, SACHIN JADHAV: Implementation of FIR Filter Using VLSI. Journal of Information, Knowledge and Research in Electronics and Communication Engineering, **4**, 1497 (2017).
21. XIN LOU, PRAMOD KUMAR MEHER, YAJUN YU, WENBIN YE: Novel Structure for Area-efficient Implementation of FIR Filters. IEEE T Circuits Syst II, **64**, 1212 (2017).
22. W. B. YE, X. LOU, Y. J.YU: Design of Low Power Multiplier Less Linear- Phase FIR Filter. IEEE Access, **5**, 23466 (2017).

Received 8 April 2019
Revised 17 April 2019

Oxidation Communications 42, No 2, 249–271 (2019)

Renewable energy sources – wind energy

MATRIX CONVERTER FOR GRID CONNECTED PERMANENT MAGNET SYNCHRONOUS GENERATOR

N. PRAKASH[a]*, C. SIVAN RAJ[b]

[a]*Department of Electrical and Electronics Engineering, Kumaraguru College of Technology, Coimbatore, India*
E-mail: *nprakash.eee22@gmail.com*
[b]*Department of Electrical and Electronics Engineering, Kathir College of Engineering, Coimbatore, Tamilnadu, India*
E-mail: *reachsivanraj@gmail.com*

ABSTRACT

Out of all renewable energy sources, wind energy seems to be prominent and quite promising for electric power generation. Wind energy conversion system (WECS) has been found to be economic, compared to the cost of fossil fuels which are rising at a much faster rate. Therefore, the research of WECS has regained importance, as they are particularly suitable for wind power plants. This thesis presents the modelling and simulation of variable speed wind turbine driven Permanent magnet synchronous generator (PMSG) connected to grid through Matrix converter (MC). MC is used to convert three phase Alternating current (AC) variable frequency variable rotor voltages into constant frequency AC voltage. Modelling of PMSG is done using its dynamic equations and then MC is integrated for the direct conversion to constant frequency, variable voltage output. The simulation of a 1hp PMSG-based Grid Connected Wind Energy Conversion System (GCWECS) is carried out using MATLAB/SIMULINK. Thus by using the single stage conversion the harmonics produced in the WECS is considerably reduced. By proper switching of MC, the output frequency of the PMSG in grid side is 50 Hz and the voltage is constant even the input is variable frequencies.

Keywords. WECS, matrix converter, PMSG, GCWECS.

AIMS AND BACKGROUND

Power Electronic Converters (PECs) play two important roles in modern variable-speed wind energy conversion systems: interfacing the wind turbine to the electrical utility grid and controlling the wind turbine. A static frequency changer can satisfy

---

* For correspondence.

the requirements of a variable-speed wind turbine. The two main structures that are suitable for this application are: DC-link AC/DC/AC converter and Matrix Converter (MC) (Refs 1–12). The most common power electronic configuration for PMSG-based variable-speed WECS is an AC/DC/AC converter with a large DC-link capacitor.

Matrix converter has drawn the attention of many researchers over the past two decades owing to various advantages such as absence of bulky DC-link energy storage devices and absence of electrolytic capacitors over the three-stage AC-DC-DC-AC converters irrespective of the type of load. The input power factor of the matrix converts can be fully controlled by proper modulation[1]. The matrix converters are more rugged than the three-stage converters, as there is no DC-link capacitor. The matrix converter has efficiency higher than the conventional three stage converter and is highly controllable for output voltage and frequency[13–22].

The individual control of output voltage, input power factor and output power factor are easily achievable. Figure 1 shows the general structure of the WECS using PMSG fed matrix converter. The MC provides direct AC/AC conversion and is considered an emerging alternative to the conventional two-stage AC/DC/AC converter topology.

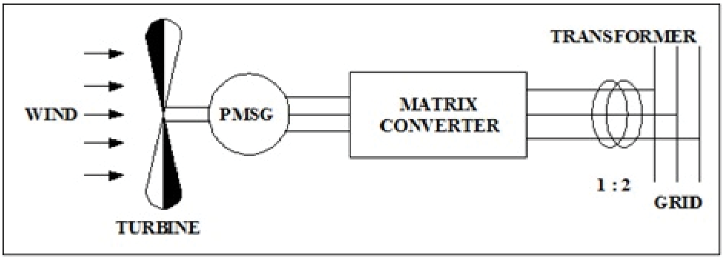

Fig. 1. General structure of PMSG based matrix converter

EXPERIMENTAL

MATRIX CONVERTER

The matrix converter is the force-commutated version of the cyclo-converters have been studied[1], which overcomes the disadvantage of the conventional cyclo-converter such as the limitations in the frequency conversion; rich output voltage harmonics and increased number of switches.

The matrix converters can be classified as direct and indirect type matrix converters. Figure 2 shows the direct or the Conventional Matrix Converter (CMC) that is an array of 3 × 3 bidirectional switches. The indirect or the sparse matrix converter is a cascade of the controlled rectifier and inverter topologies without a DC-link in between.

Both the topologies directly interconnect two independent multi-phase voltage systems at different frequencies. In this research, the CMC topology is chosen and is analysed for its performance for changes in its topology and with different Pulse Width Modulation (PWM) techniques.

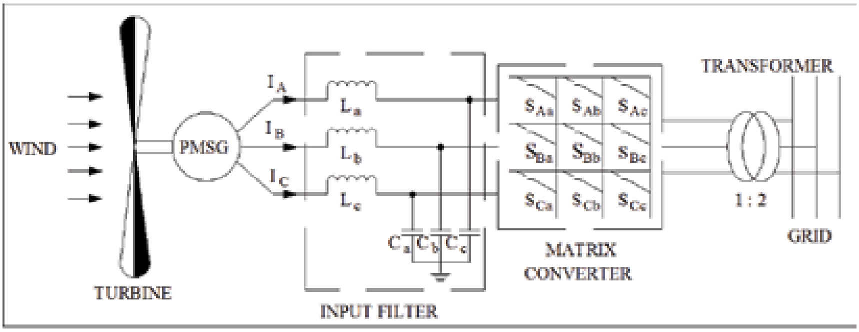

Fig. 2. Structure of matrix converter

The matrix converter is connected to a stiff voltage source at the input and a stiff current source at the output. These externally connected voltage and current sources impose constraints on the switching of the matrix converter. At any instant, the voltage source should not be short-circuited and the current source should not be open circuited. Equation (1) gives the switching function of the switch S_{ij} in Fig. 2:

$$S_{ij}(t) = 1,\ S_{ij} = \text{closed};\ S_{ij}(t) = 0,\ S_{ij} = \text{open}, \tag{1}$$

where $i = (\mathrm{A, B, C})$ and $j = (\mathrm{a, b, c})$.

Equation (1) gives the constraints, namely, the inputs are not short-circuited and the outputs are not open-circuited.

$$d_{\mathrm{A}j} + d_{\mathrm{B}j} + d_{\mathrm{C}j} = 1 \tag{2}$$

where d_{ij} is the duty-cycle of the switch S_{ij}.

Equation (2), being less than one, indicates an open-circuit of the current source and equation (2), being greater than one, indicates a short circuit of the voltage source. Therefore, equations (3) and (4) represent the switching function T of the matrix converter for the output voltages and the input currents.

$$V_{\mathrm{out}} = T\,V_{\mathrm{in}}$$

$$\begin{bmatrix} V_{\mathrm{a}} \\ V_{\mathrm{b}} \\ V_{\mathrm{c}} \end{bmatrix} = \begin{bmatrix} S_{\mathrm{Aa}} & S_{\mathrm{Ab}} & S_{\mathrm{Ac}} \\ S_{\mathrm{Ba}} & S_{\mathrm{Bb}} & S_{\mathrm{Bc}} \\ S_{\mathrm{Ca}} & S_{\mathrm{Cb}} & S_{\mathrm{Cc}} \end{bmatrix} \begin{bmatrix} V_{\mathrm{A}} \\ V_{\mathrm{B}} \\ V_{\mathrm{C}} \end{bmatrix}, \tag{3}$$

where

$$V_{\mathrm{out}} = \begin{bmatrix} V_{\mathrm{a}} \\ V_{\mathrm{b}} \\ V_{\mathrm{c}} \end{bmatrix};\ T = \begin{bmatrix} S_{\mathrm{Aa}} & S_{\mathrm{Ab}} & S_{\mathrm{Ac}} \\ S_{\mathrm{Ba}} & S_{\mathrm{Bb}} & S_{\mathrm{Bc}} \\ S_{\mathrm{Ca}} & S_{\mathrm{Cb}} & S_{\mathrm{Cc}} \end{bmatrix};\ V_{\mathrm{in}} = \begin{bmatrix} V_{\mathrm{A}} \\ V_{\mathrm{B}} \\ V_{\mathrm{C}} \end{bmatrix}.$$

$$I_{\mathrm{in}} = T^{T} I_{\mathrm{out}}$$

$$\begin{bmatrix} I_{\mathrm{A}} \\ I_{\mathrm{B}} \\ I_{\mathrm{C}} \end{bmatrix} = \begin{bmatrix} S_{\mathrm{Aa}} & S_{\mathrm{Ab}} & S_{\mathrm{Ac}} \\ S_{\mathrm{Ba}} & S_{\mathrm{Bb}} & S_{\mathrm{Bc}} \\ S_{\mathrm{Ca}} & S_{\mathrm{Cb}} & S_{\mathrm{Cc}} \end{bmatrix} \begin{bmatrix} I_{\mathrm{a}} \\ I_{\mathrm{b}} \\ I_{\mathrm{c}} \end{bmatrix}, \tag{4}$$

$$I_{\mathrm{in}} = \begin{bmatrix} I_{\mathrm{A}} \\ I_{\mathrm{B}} \\ I_{\mathrm{C}} \end{bmatrix}; \; T^{T} = \begin{bmatrix} S_{\mathrm{Aa}} & S_{\mathrm{Ab}} & S_{\mathrm{Ac}} \\ S_{\mathrm{Ba}} & S_{\mathrm{Bb}} & S_{\mathrm{Bc}} \\ S_{\mathrm{Ca}} & S_{\mathrm{Cb}} & S_{\mathrm{Cc}} \end{bmatrix}; \; I_{\mathrm{out}} = \begin{bmatrix} I_{\mathrm{a}} \\ I_{\mathrm{b}} \\ I_{\mathrm{c}} \end{bmatrix} V_{\mathrm{A}}.$$

where V_{A}, V_{B}, V_{C} and V_{a}, V_{b}, V_{c} are the input and the output phase voltages, respectively, and I_{A}, I_{B}, I_{C} and I_{a}, I_{b}, I_{c} – the input and the output currents, respectively.

SPACE VECTOR PULSE WIDTH MODULATION

The first version of the SVM technique focused on only output sinusoidal voltage generation by applying the SVM technique to output stage. Later, Huber presented the full version of SVM using the space vector techniques in the input stage as well as the output stage, which can simultaneously achieve sinusoidal input and output currents. This algorithm has given a significant impact by enabling the SVM used in the conventional PWM-VSI to be applied to the matrix converter.

While the Venturini method is inherently less flexible because of its mathematical approach, the SVM algorithm allows the matrix converter to use a variety of control methods. A very elegant and powerful solution currently in use is to apply space-vector modulation (SVM) in MCs (Refs 2 and 3). For proper operation of Matrix Converter, only one switch in each output phase must be conducting. This leads to twenty seven possible switching combinations for the Matrix Converter. In a three-phase to three-phase Matrix Converter there are twenty seven possible switching states. The output voltage states are categorised in three groups. Group III is not used. Combination of Group I and Group II zero vectors are preferred depending on desired magnitude and frequency of output voltage.

The space vector algorithm is based on the representation of the three phase input current and three phase output line voltages on the space vector plane. In matrix converters, each output phase is connected to each input phase depending on the state of the switches. For safe switching in the matrix converter:

- Input phases should never be short-circuited;
- Owing to the presence of inductive load.

The load currents should not be interrupted at any switching time. There are 27 different switching combinations for connecting output phases to input phases if the above two rules are provided. These switching combinations can be analysed in three groups. Each output phase is directly connected to three input phases in turns with six switching combinations in the first group. In this case, the phase angle of output voltage vector depends on the phase angle of the input voltage vector. Similar condition is also valid for current vectors.

For the space vector modulation technique, these switching states are not used in the matrix converter since the phase angle of both vectors cannot be controlled independently. There are 18 switching combinations in the second group in which the active voltage vector is formed at variable amplitude and frequency.

Amplitude of the output voltages depends on the selected input line voltages. In this case, the phase angle of the output voltage space vector does not depend on the phase angle of the input voltage space vector. Similar condition is also valid for current vectors. The last group with 3 switching combinations consists of zero vectors. In this case, all of the output phases are connected to the same input phase.

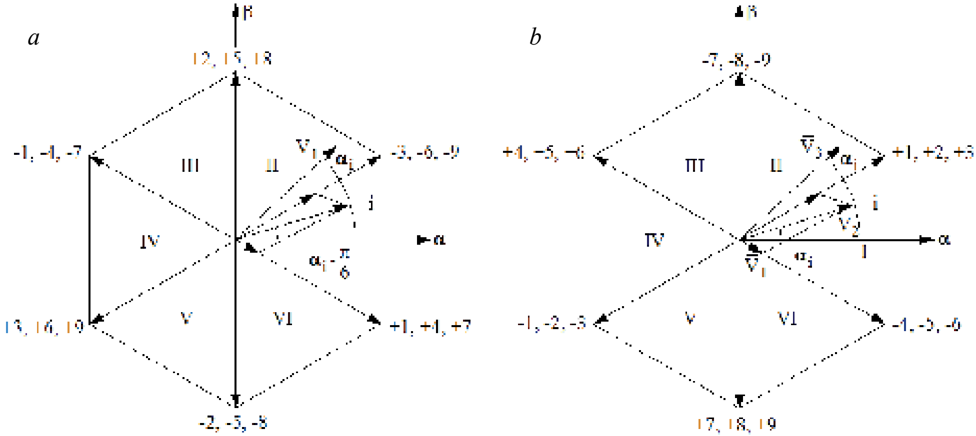

Fig. 3. Space vector representations: input currents – *a*, and output line voltages – *b*

Output line voltage and input current space vectors are used in the application of the space vector control technique for the matrix converter. Figure 3 shows the representation of the input current and output line voltage space vectors ($|\vec{V}_1|$ and $|\vec{V}_0|$ represent instantaneous input and output voltage vectors, respectively, α_i and α_0 represent the phase angels of input and output voltages, respectively). In order to determine the switches that will conduct, it should be decided that α_i and α_0 are in which sectors of input current and output line voltages shown in Fig. 3. There are 36 sectors based on the position of α_i and α_0.

The switching combinations for turning on are determined according to the specified vector. Duty period of each switch is determined by considering the common switching combinations of both vectors. Duty period of the switches for each switching combinations should be calculated to obtain the desired voltage amplitude and frequency at the output of matrix converter. Equation (5) gives the switching times for being both α_i and α_0 in sector I.

Solution Interval for equation (1) is $0 \le \alpha_i \le \pi/3$, $\pi/6 \le \alpha_0 \le \pi/6$ and this algorithm gives a maximum voltage transfer ratio between the input and output voltages of 86.6%.

Sum of the switching times in equation (5) must not exceed the switching period. Otherwise, the switches will turn on at overshoot mode. Sum of the switching times must ensure the condition given in equation (6).

$$\delta_1^+ = 2/3^{1/2}\, T_s q \sin(\alpha_0 + \pi/6) \sin(\pi/3 - \alpha_i)$$

$$\delta_3^- = 2/3^{1/2}\, T_s q \sin(\alpha_0 + \pi/6) \sin(\alpha_i) \tag{5}$$

$$\delta_4^- = 2/3^{1/2}\, T_s q \sin(\pi/6 - \alpha_0) \sin(\pi/3 - \alpha_i)$$

$$\delta_6^+ = 2/3^{1/2}\, T_s q \sin(\pi/6 - \alpha_0) \sin(\alpha_i) \tag{6}$$

$$\delta_1^+ + \delta_3^- + \delta_4^- + \delta_6^+ \le T_s,$$

where T_s is the switching period. Switching order in the space vector control algorithm can be obtained by considering the rules given below.

- 1 and 4 switching order must have two same letters in same position.
- 2 and 3 switching order must only change one letter according to 1 and 4 switching order, respectively.

SIMULATION RESULTS

Simulations of the proposed control strategy for a PMSG based wind power generation system were carried out, using MATLAB/SIMULINK. Discrete models were used with a simulation time step of 1.5 s. The PMSG is rated at 1 kW and the stator line voltage is 400 V. During simulations, a sampling frequency of 10 kHz was used for the proposed control strategy. A high-frequency AC filter is connected to the stator side to absorb the switching harmonics generated by the converters.

Figure 4 shows the SIMULINK model of matrix converter with PMSG and the PMSG with MC have been analysed for various frequencies generated by the generator. The various frequencies in account are recorded as 10, 25, 50 and 56.4 Hz.

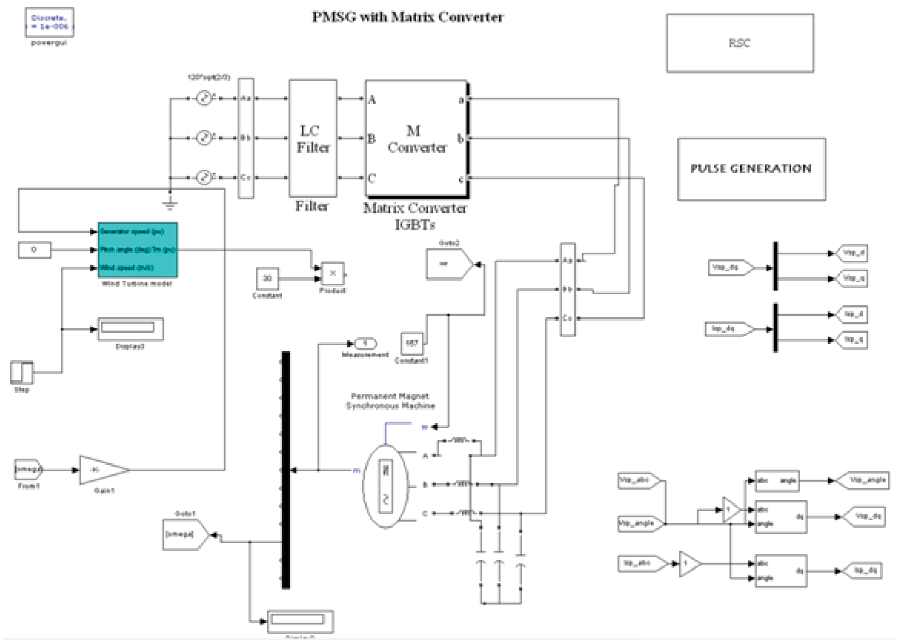

Fig. 4. SIMULINK modelling of matrix converter with PMSG

Simulation result for 10 Hz generated frequency. Figures 5, 6, 7 and 8 show the generator phase voltage, generator current, and line voltage after matrix converter and grid side current for frequency10 Hz, respectively.

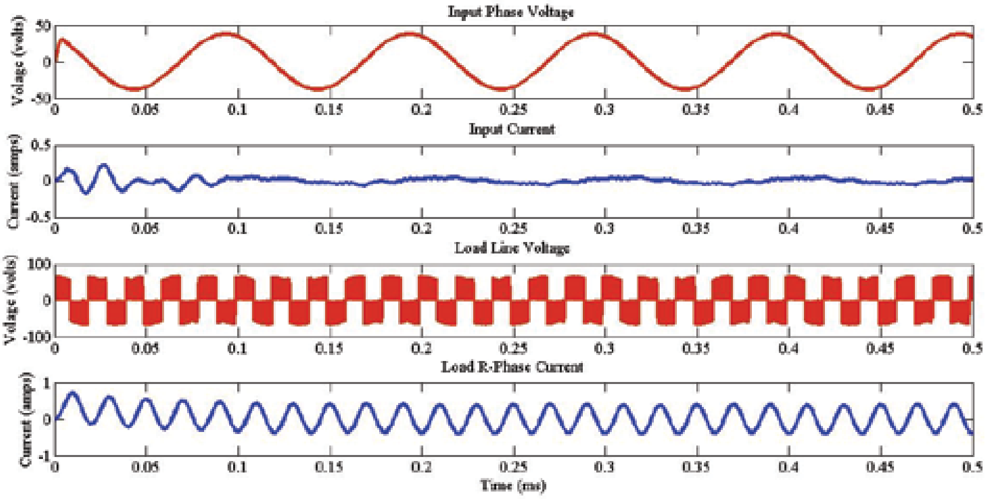

Fig. 5. Generator phase voltage, generator current, and line voltage after matrix converter, grid side current

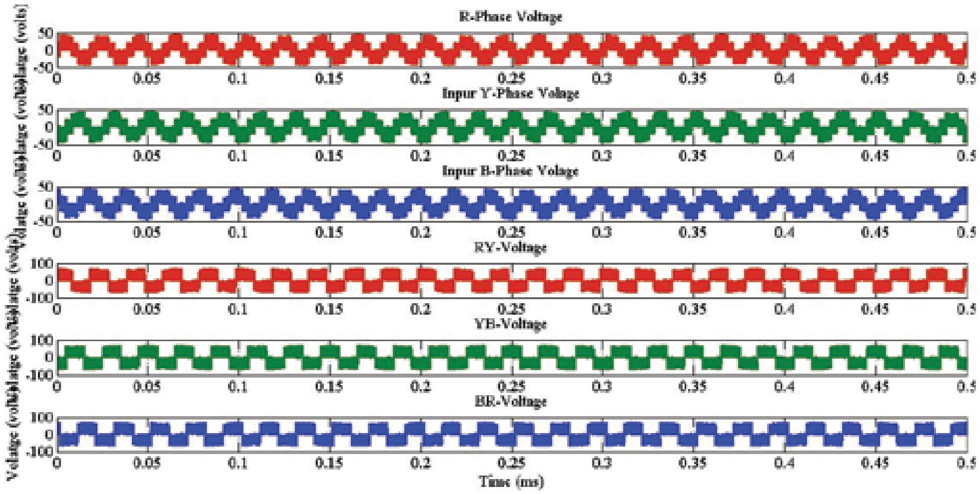

Fig. 6. Phase voltage and line voltage of three phases after the converter

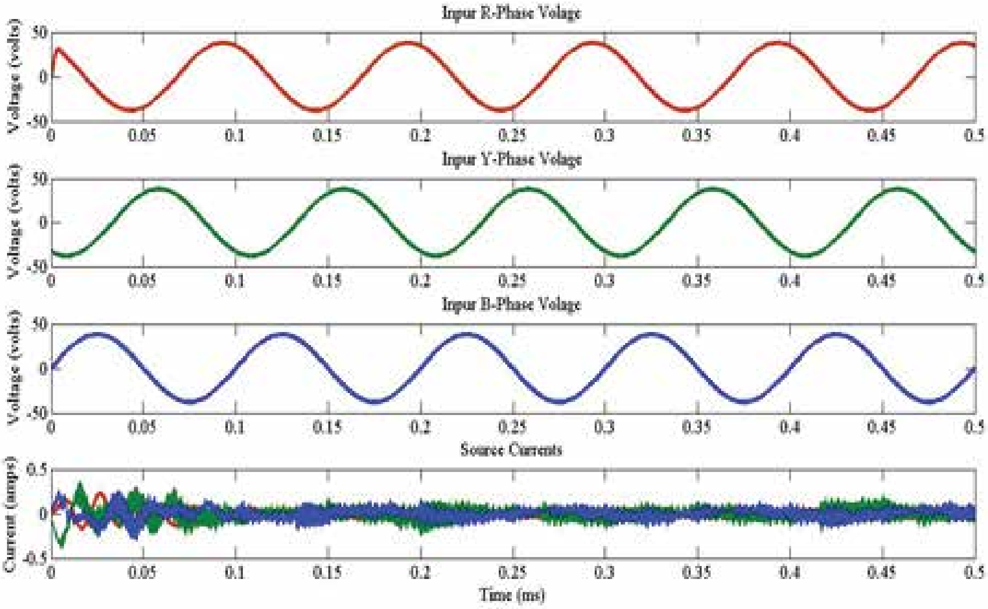

Fig. 7. Phase voltage and source current of generator

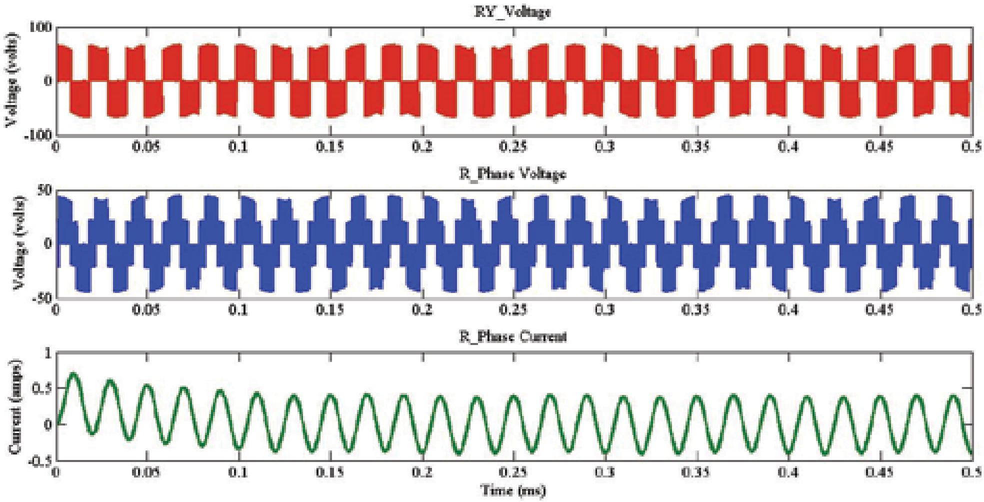

Fig. 8. Line voltage, phase voltage and phase current

Simulation result for 25 Hz generated frequency. The 25 Hz frequency waveforms are listed below. Generator phase voltage, current and line voltage is shown in Fig. 9 and three phase voltage and current after the converter is shown in Fig. 10.

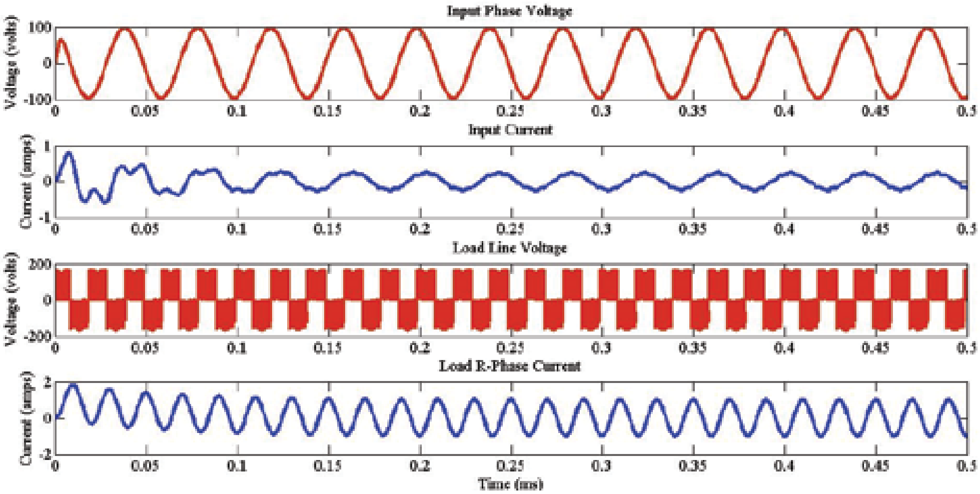

Fig. 9. Generator phase voltage, generator current, and line voltage after matrix converter, grid side current

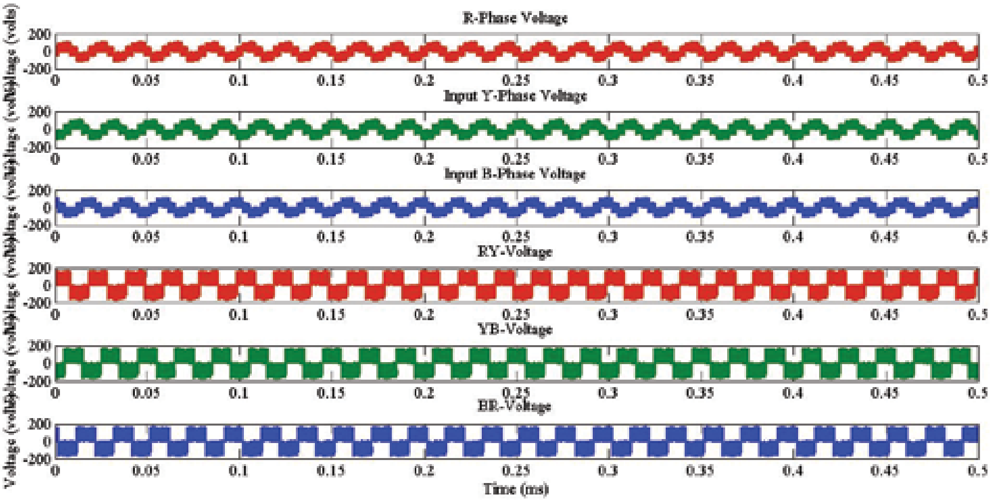

Fig. 10. Phase voltage and line voltage of three phases after the converter

Line voltage, phase voltage and phase current waveform is shown in Fig. 11 and the phase voltage, source current of the generator is shown in Fig. 12.

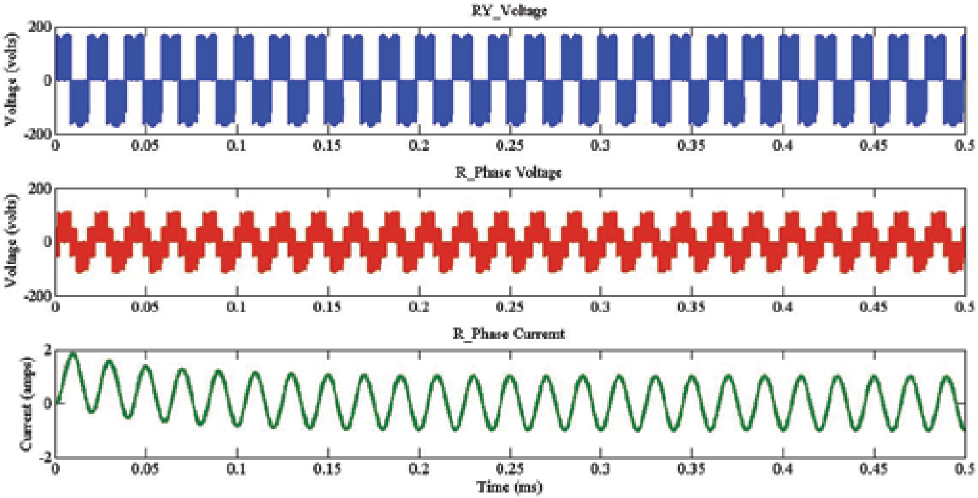

Fig. 11. Line voltage, phase voltage and phase current

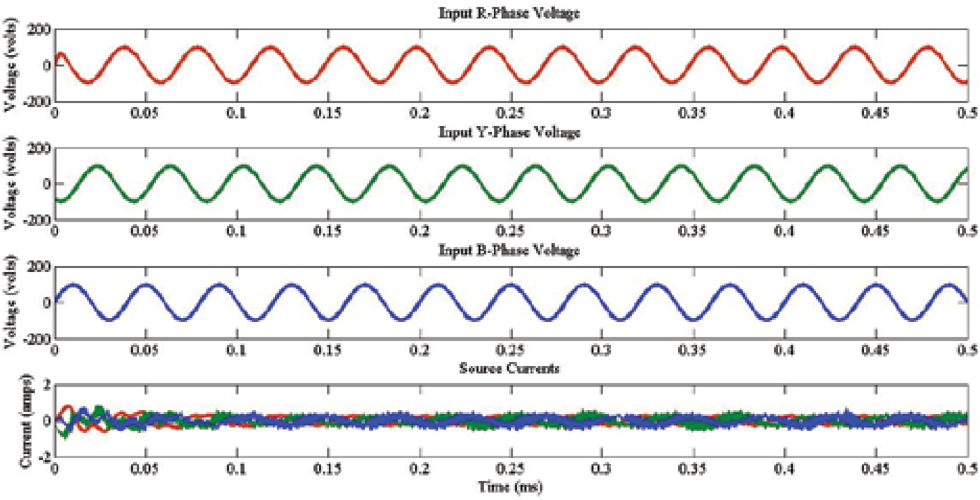

Fig. 12. Phase voltage and source current of generator

Simulation result for 50 Hz generated frequency. The 50 Hz frequency waveforms are listed below. Generator phase voltage, current and line voltage are shown in Fig. 13 and three phase voltage and current after the converter is shown in Fig. 14.

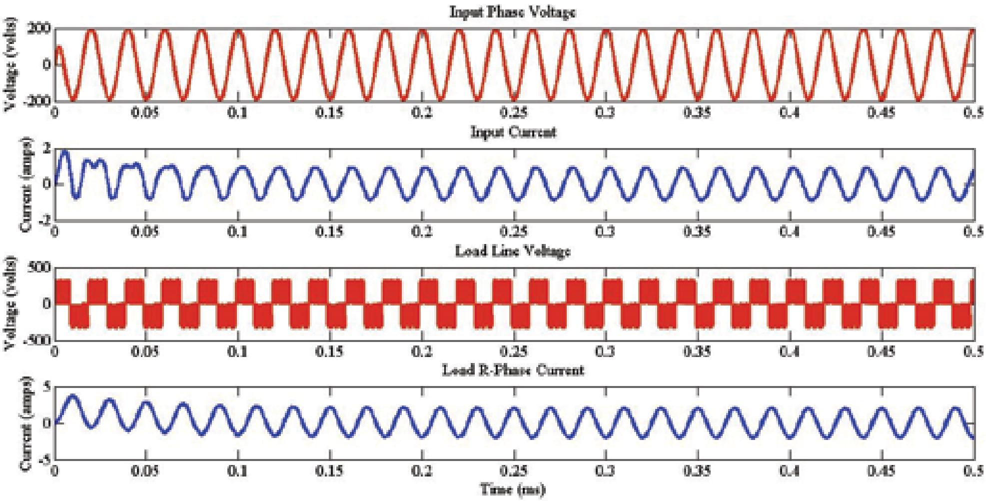

Fig. 13. Generator phase voltage, generator current, and line voltage after matrix converter, grid side current

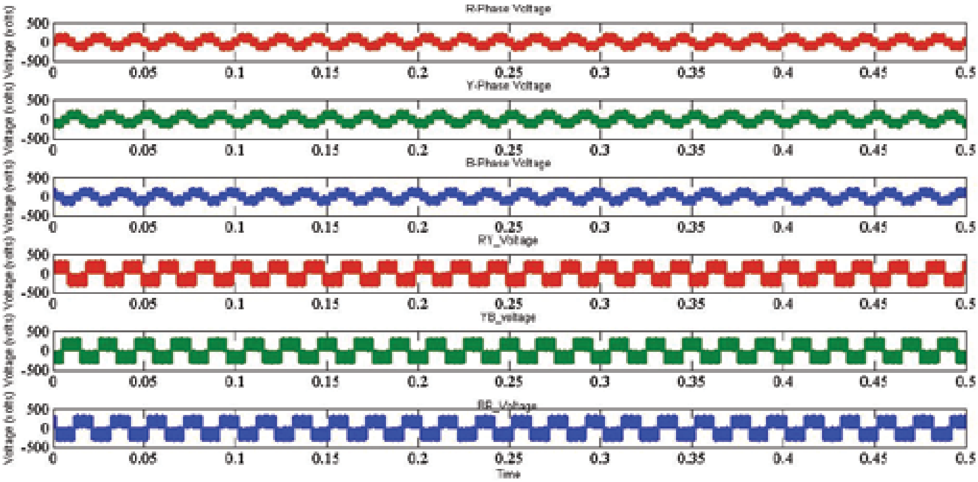

Fig. 14. Phase voltage and line voltage of three phases after the converter

Line voltage, phase voltage and phase current waveforms are shown in Fig. 15 and the phase voltage and source current of the generator are shown in Fig. 16.

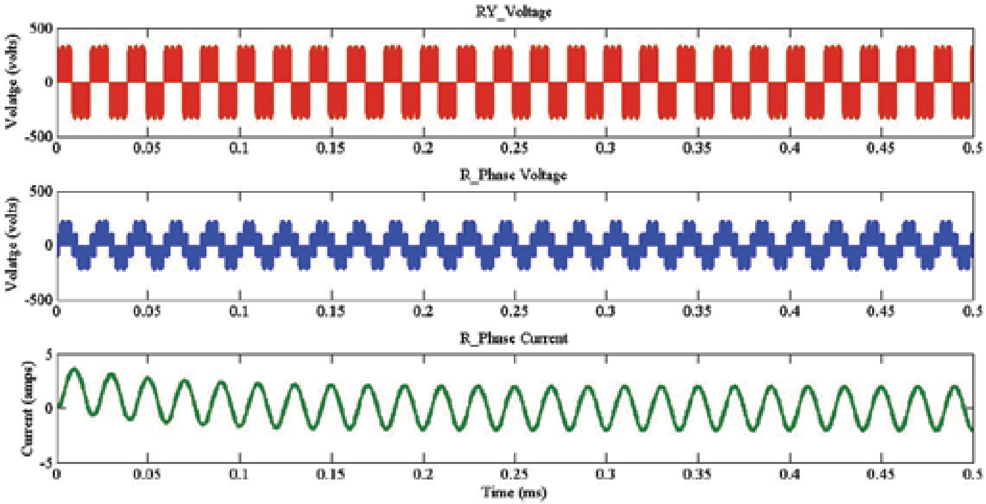

Fig. 15. Line voltage, phase voltage and phase current

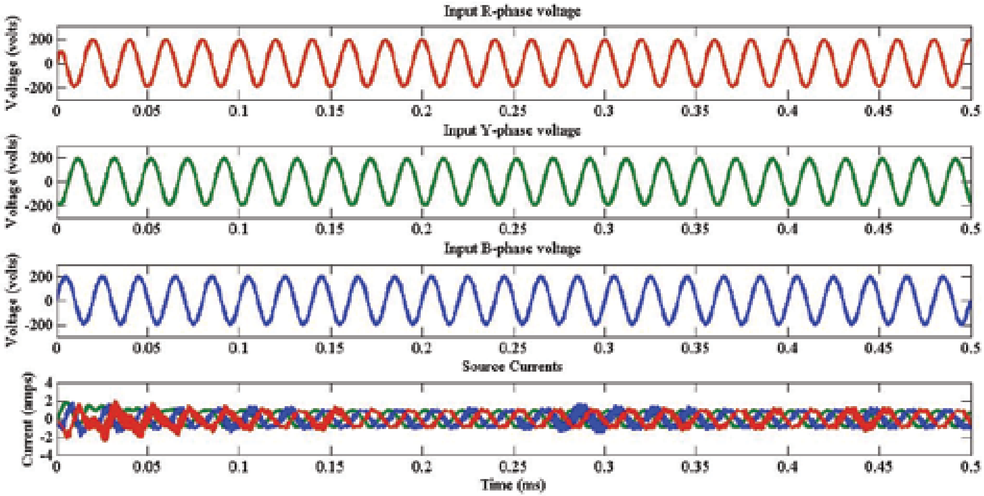
Input R-phase voltage

Input Y-phase voltage

Input B-phase voltage

Source Currents

Fig. 16. Phase voltage and source current of generator

Simulation result for 56.4 Hz generated frequency. The 56.4 Hz frequency waveforms are listed below. Generator phase voltage, current and line voltage are shown in Fig. 17 and three phase voltage and current after the converter are shown in Fig. 18.

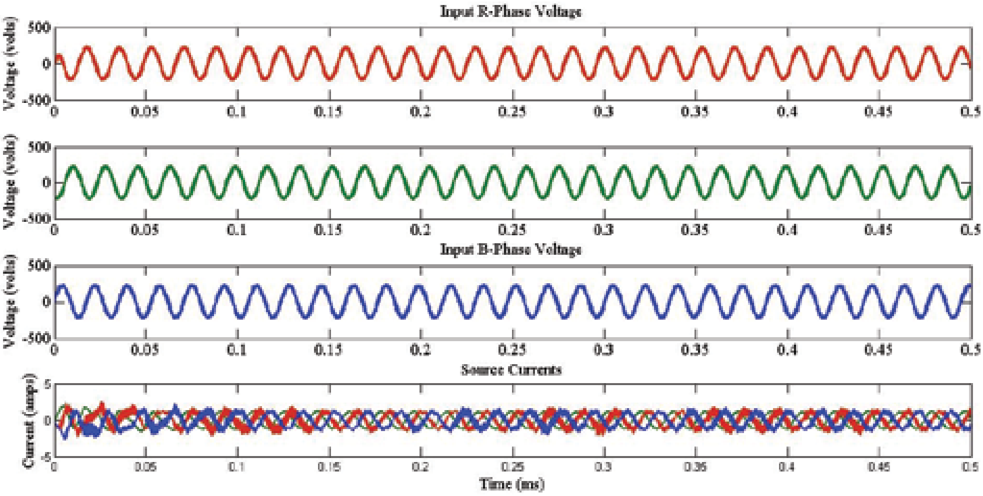
Input R-Phase Voltage

Input B-Phase Voltage

Source Currents

Fig. 17. Phase voltage and source current of generator

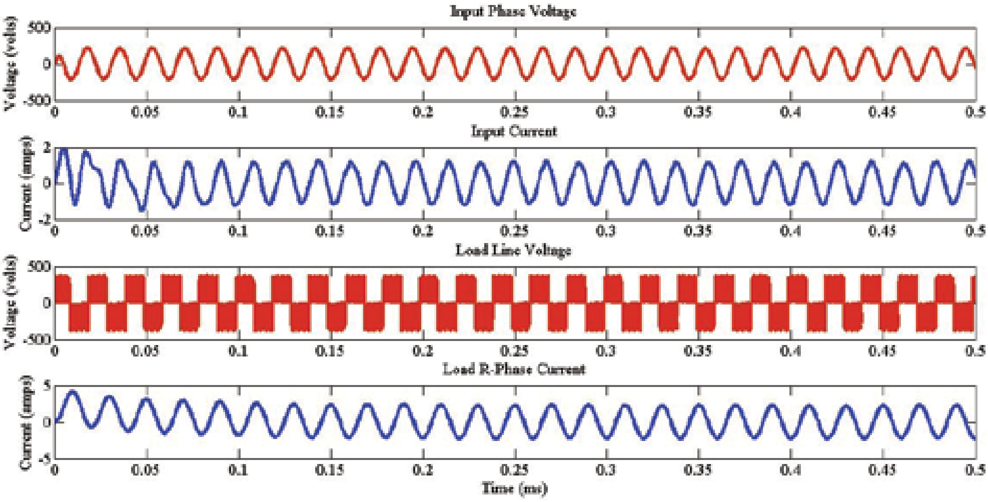

Fig. 18. Generator phase voltage, generator current, and line voltage after matrix converter, grid side current

Line voltage, phase voltage and phase current waveforms are shown in Fig. 19 and the phase voltage and source current of the generator are shown in Fig. 20.

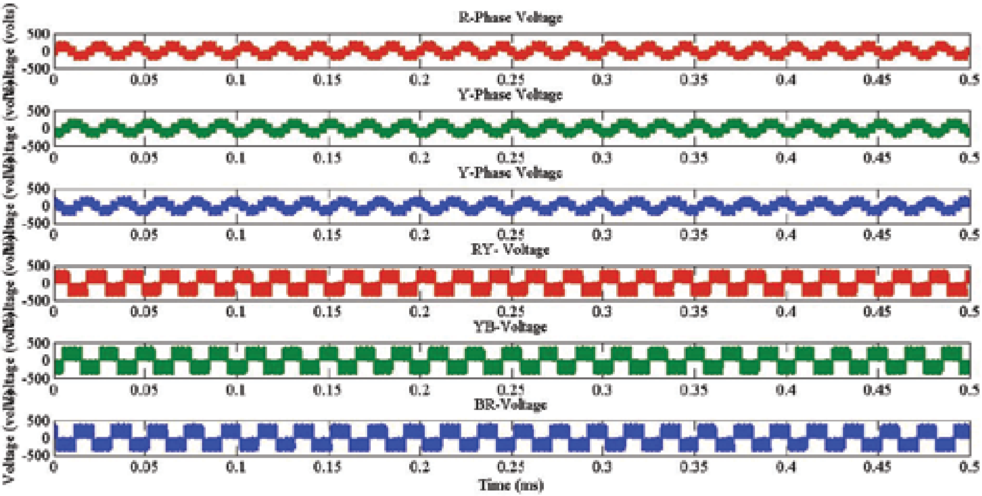

Fig. 19. Phase voltage and line voltage of three phases after the converter

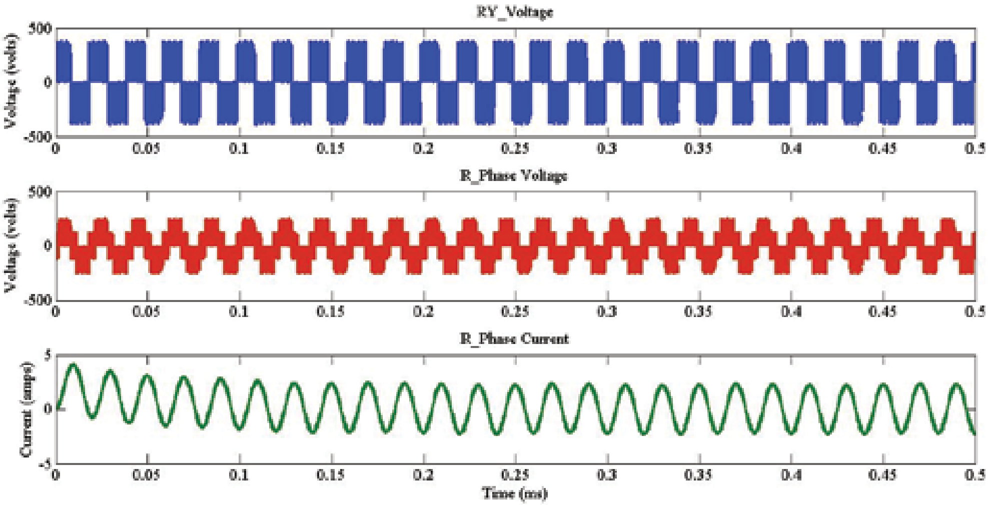

Fig. 20. Line voltage, phase voltage and phase current

DESCRIPTION OF EXPERIMENTAL WORK-BENCH

The performance of MC with PMSG is validated using the hardware setup. The specification of hardware components used to implement the test rig of MC is tabulated in Table 1.

Table 1. Components specification of experimental test rig

Name of the component	Specification
Permanent magnet synchronous generator	1 kW, 220V AC, 1000 rpm
Grid – coupling transformer	transformation ratio 1:2
DC Machine	1 hp, 1450 rpm, 4 pole, 220 V
3-phase controlled IGBT matrix converter	AC/DC, 1200 V, 25 A
Power quality analyser	Yokogawa WT 1800
FPGA – controller	SPARTAN-6
Switching frequency	20 kHz

Figure 21 shows the three phase voltage and current before LC filter at a frequency of 70 Hz. This voltage is peak to peak of 280 V, that is equal to 194 V rms. Figures 22 to 25 show the voltage and current for different frequencies 31, 25, 56, and 50 Hz, respectively.

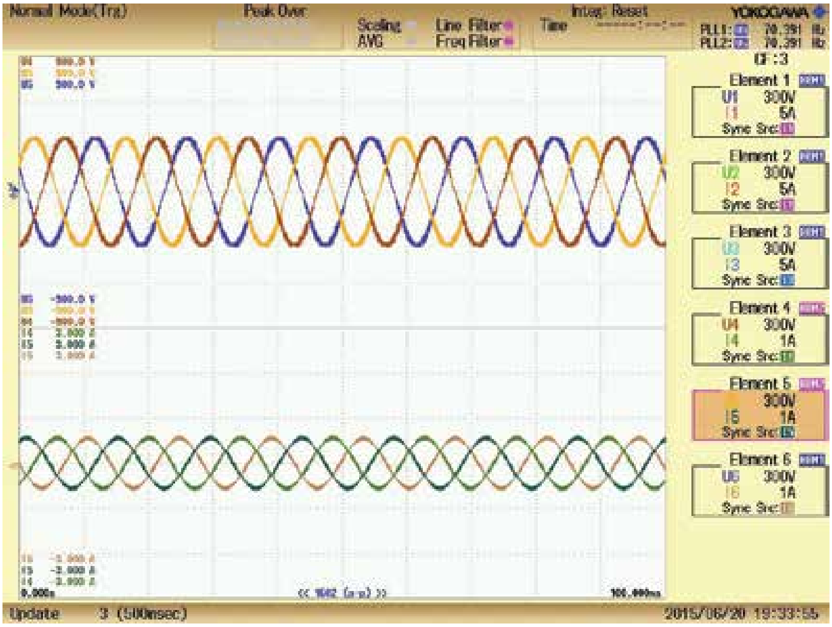

Fig. 21. Three phase voltage and current before LC filter (*f* = 70 Hz)

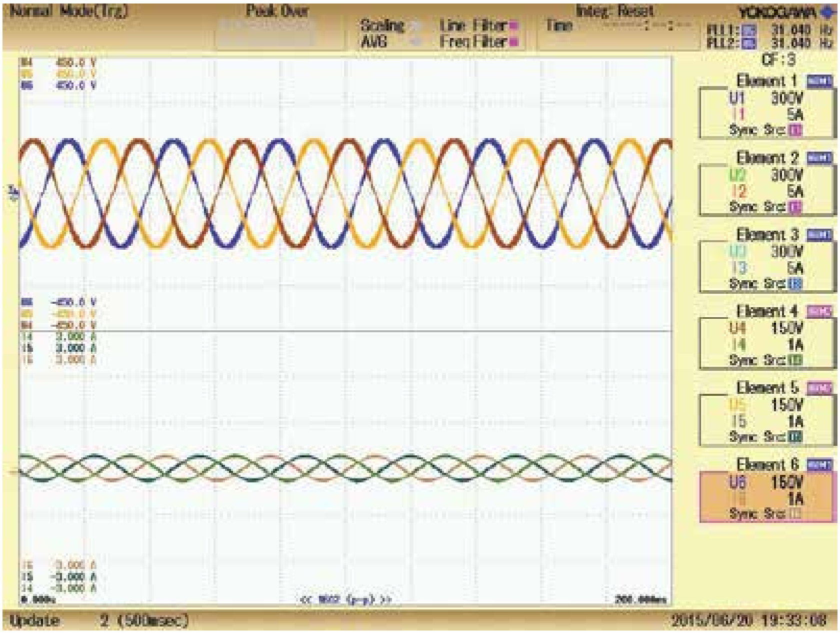

Fig. 22. Three phase voltage and current before LC filter (*f* = 31 Hz)

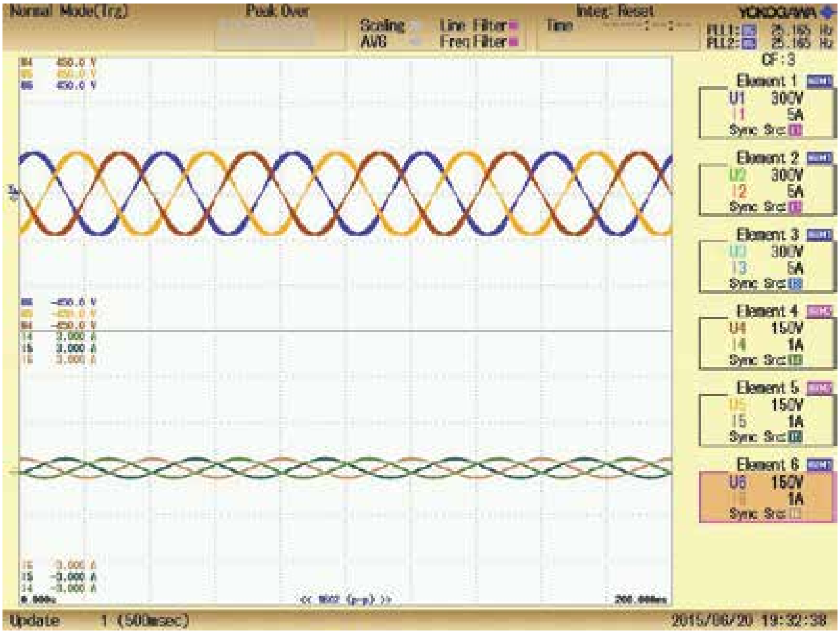

Fig. 23. Three phase voltage and current before LC filter (*f* = 25 Hz)

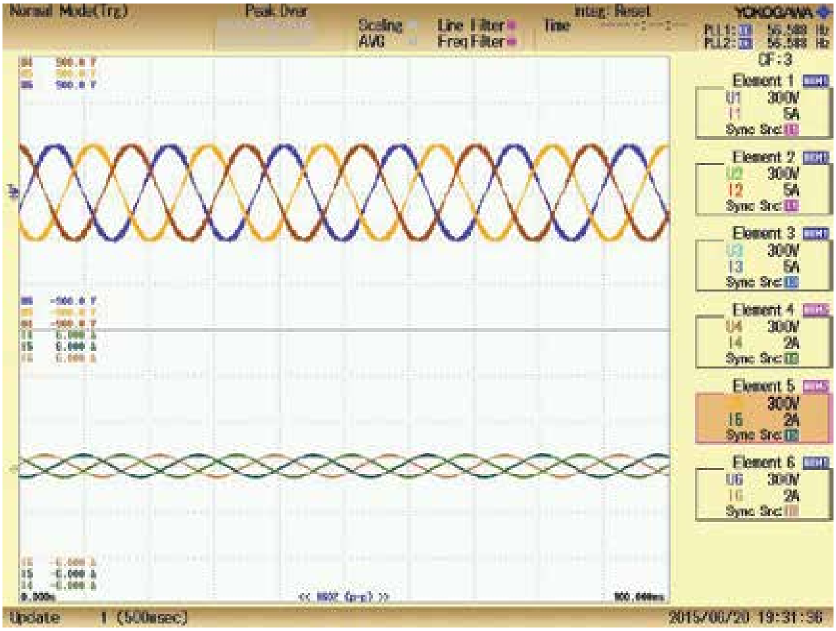

Fig. 24. Three phase voltage and current before LC filter (*f* = 56 Hz)

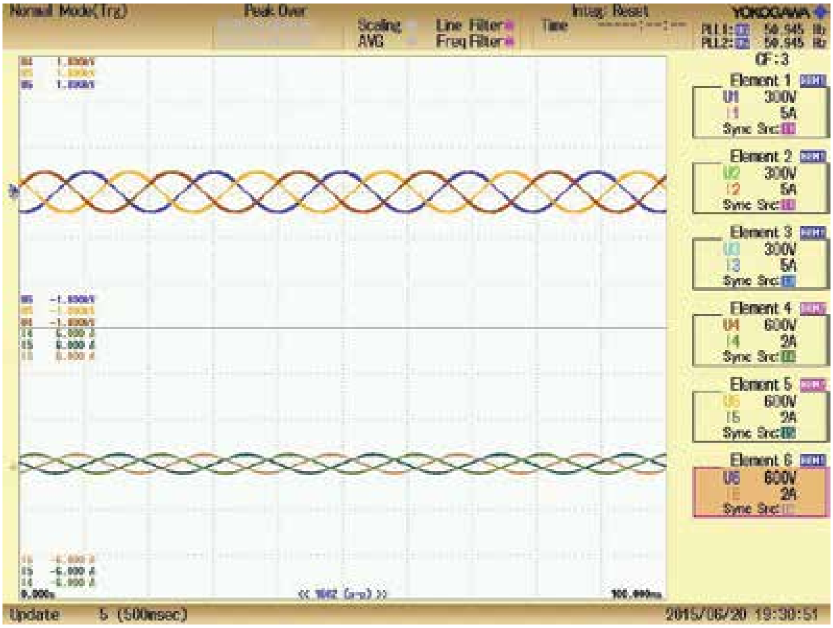

Fig. 25. Three phase voltage and current before LC filter (*f* = 50 Hz)

Figures 26 to 29 show the one phase voltage of matrix converter output before LC filter for 25, 50, 50.4, and 56 Hz, respectively.

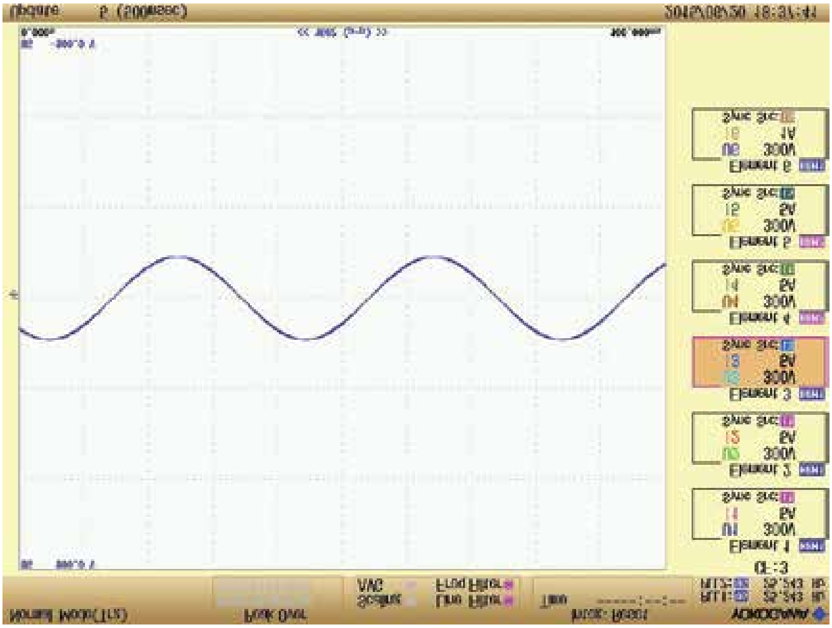

Fig. 26. One phase voltage of matrix converter output before LC filter (*f* = 25 Hz)

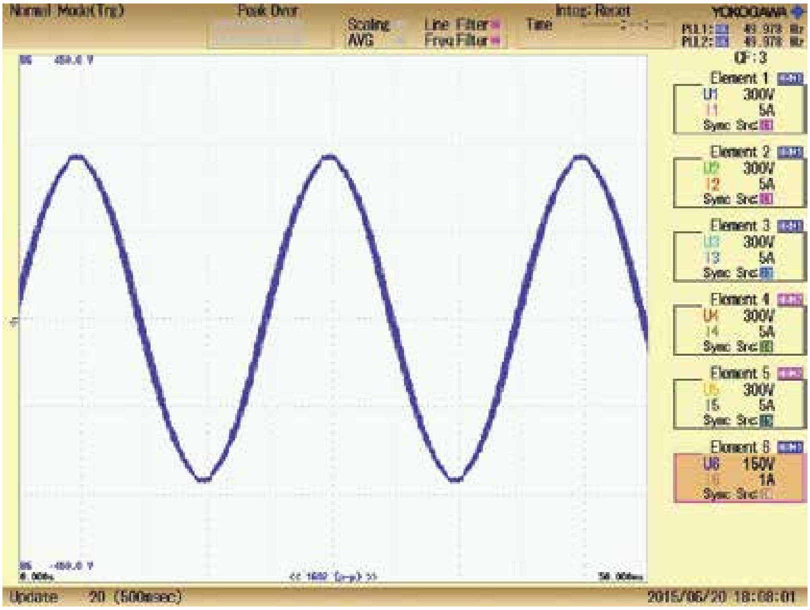

Fig. 27. One phase voltage of matrix converter output before LC filter ($f = 50$ Hz)

Fig. 28. One phase voltage of matrix converter output before LC filter ($f = 50.4$ Hz)

Fig. 29. One phase voltage of matrix converter output before LC filter (*f* = 56 Hz)

Figures 30 and 31 show THD of source current and THD of grid current, respectively. They are measured as 3.8 and 2.3%, respectively.

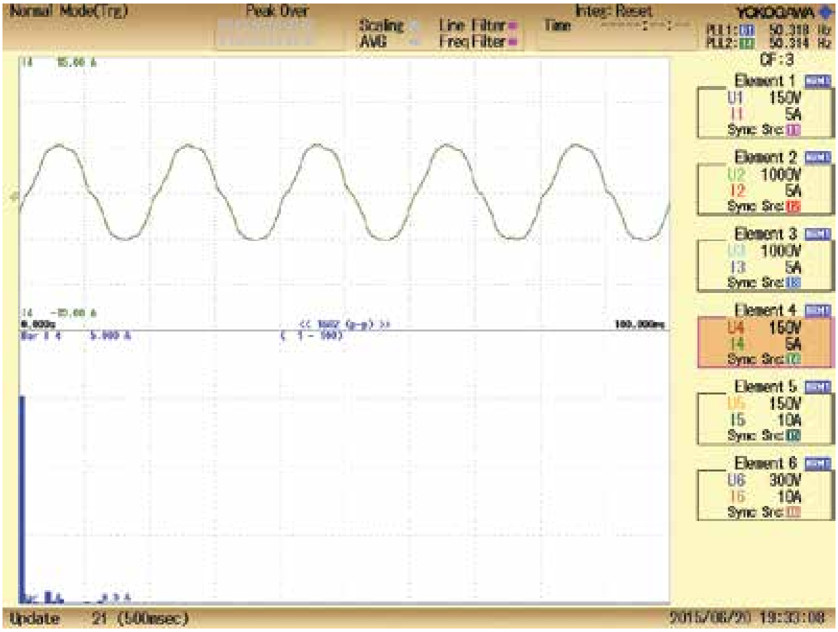

Fig. 30. THD of source current (3.8%)

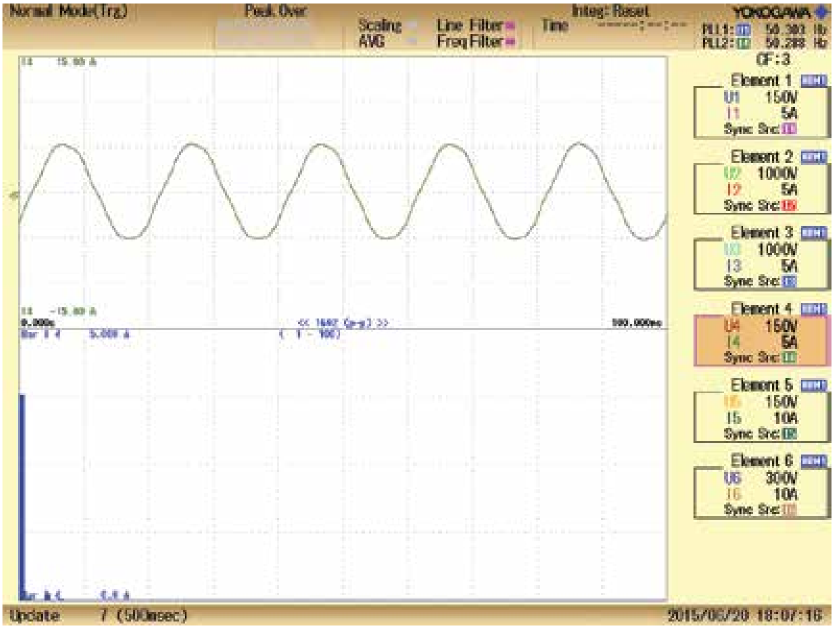

Fig. 31. THD of grid current (2.3%)

CONCLUSIONS

The modelling of PMSG is done in Simulink and for variable speed it produces variable frequency variable voltage output. This thesis presents mathematical model of matrix converter and interfacing with PMSG is done using MATLAB/Simulink. For variable frequency input source voltage generated by PMSG, the matrix converter is able to produce constant frequency output that can be integrated with the grid. The simulation of a 1 hp PMSG based GCWECS is carried out using MATLAB/SIMULINK. Owing to the single stage conversion, the harmonics produced in the WECS is less and it is recorded as 3.8% at source side and 2.3% at grid side. Owing to proper switching of MC, the output frequency of the voltage is 50 Hz even the input is variable.

REFERENCES

1. P. H. DEVINANT, T. LAVERNE, J. HUREAU: Experimental Study of Wind-Turbine Air Foil Aerodynamics in High Turbulence. J Wind Eng Ind Aerod, **90**, 689 (2002).
2. S. M. DEHGHAN, M. MOHAMADIAN, A. Y. VARJANI: A New Variable Speed Wind Energy Conversion System Using Permanent-Magnet Synchronous Generator and z-Source Inverter. IEEE T Energy Conver, **24** (3), 714 (2009).
3. Y. HIGUCHI, N. YAMAMURA, M. ISHIDA, T. HORI: An Improvement of Performance for Small-scaled Wind Power Generating System with Permanent Magnet Type Synchronous Generator. In: Proceeding of 26th IEEE IECON, Vol. 2, 2000, 1037–1043.

4. HUA YE, JUAN SU, SONGHUAI DU: Simulation and Analysis of PMSG-based Wind Energy Conversion System Using Different Converter Models. Scientific Research Engineering, **5**, 96 (2013).
5. N. LACHGUER, M. T. LAMCHICH: Control Strategy of Permanent Magnet Synchronous Generator for Standalone Wind Power Generation System. In: Proceedings of the Conference: Electrical Machines and Power Electronics and 2011 Electromotion Joint Conference (ACEMP), 2011 International Aegean Conference, Vol. 8 (10), 2011, 392–397.
6. H. LI, Z. CHEN: Overview of Different Wind Generator Systems and Their Comparisons. Renewable Power Generation, IET, **2** (2), 123 (2008).
7. A. K. MANAULLAH SHARMA, H. AHUJA, A. SINGH: Performance Comparison of DFIG and SCIG Based Wind Energy Conversion Systems. Computational Intelligence on Power, Energy and Controls with Their Impact on Humanity (CIPECH), Innovative Applications, **28** (29), 285 (2014).
8. S. MANIVANNAN, S. VEERAKUMAR, P. KARUPPUSAMY, A. NANDHAKUMAR: Performance Analysis of Three Phase Voltage Source Inverter Fed Induction Motor Drive with Possible Switching Sequence Execution in SVPWM. International Journal of Advanced Research in Electrical, Electronics and Instrumentation Engineering, **3** (6), 10081 (2014).
9. S. MORIMOTO, T. NAKAMURA, Y. TAKEDA: Power Maximization Control of Variable Speed Wind Generation System Using Permanent Magnet Synchronous Generator. IEEJ Trans Power Energy, **123-B** (12), 1573 (2003).
10. K. PRECHANON: Mathematical Model of the PMSG Based on Wind Energy Conversion System International Research Journal of Innovative Engineering, **1** (3), 14 (2015).
11. J. RODRIGUEZ, M. RIVERA, J. W. KOLAR, P. W. WHEELER: A Review of Control and Modulation Methods for Matrix Converters. IEEE Trans Ind Electron, **59** (1), 58 (2012)
12. N. SATHISH, S. ELANGO: Analysis of Matrix Converter with Various Inputs Using Power Simulation. International Journal of Innovative Research in Science, Engineering and Technology, **3** (Special Issue 2), 168 (2014).
13. SHARON D. RONALD, A. SHEELA, S. JOSEPHIN MARY: Three Phase to Three Phase Direct Matrix Converter Using SPWM Technique. International Journal of Soft Computing and Engineering (IJSCE), **3** (2), 297 (2013).
14. SHILPA MISHRA, S. CHATTERJI, S. L. SHIMI, SANDEEP SHUKLA: Modeling and Control of Standalone PMSG WECS for Grid Compatibility at Varying Wind Speeds. International Journal of Engineering Trends and Technology (IJETT), **17** (10), 495 (2014).
15. T. TAFTICHT, K. AGBOSSOU, A. CHERITI, M. L. DOUMBIA: Output Power Maximization of a Permanent Magnet Synchronous Generator Based Standalone Wind Turbine. In: Proceedings of IEEE ISIE, Montreal, QC, Canada, 2412–2416, 2006.
16. K. TAN, S. ISLAM: Optimum Control Strategies in Energy Conversion of PMSG Wind Turbine System without Mechanical Sensors. IEEE Trans Energy Conversion, **19** (2), 392 (2004); THOMAS FRIEDLI, JOHANAN W. KALOR: Milestone in Matrix of Converter Research. IEEE Journal of Industry Application, **1** (1), 2 (2012).
17. S. THANGAPRAKASH, A. KRISHNAN: Comparative Evaluation of Modified Pulse Width Modulation Schemes Of Z-Source Inverter for Various Applications and Demands. International Journal of Engineering, Science and Technology, **2** (1), 103 (2010).
18. P. TRIPURA, Y. S. KISHORE BABU, Y. R. TAGORE: Space Vector Pulse Width Modulation Schemes for Two-level Voltage Source Inverter. ACEEE International Journal on Control System and Instrumentation, **02** (03), 34 (2011).
19. N. R. TUMMURU, M. K. MISHRA, S. SRINIVAS: Synchronization of Variable Speed PMSG Based Wind Energy Conversion System to the Grid with Power Quality Improvement Features. In: Proceedings of the IEEE International Conference on Power Electronics, Drives and Energy Systems (PEDES 2012), Bengaluru, India, Vol. 1, 2012, 1–6.

20. D. M. VILATHGAMUWA, WANG XIAOYU, C. J. GAJANAYAKE: Z-source Converter Based Grid-Interface for Variable-speed Permanent Magnet Wind Turbine Generators. In: Proceedings of the Power Electronics Specialists Conference, PESC, IEEE, Vol. 15, 2008, 4545–4550.
21. YULONG LI, NAM-SUP CHOI, BYUNG-MOON HAN, KYOUNG MIN KIM, BUHM LEE, JUN-HYUB PARK: Direct Duty Ratio Pulse Width Modulation Method for Matrix Converters. International Journal of Control, Automation, and Systems, **6** (5), 660 (2008).
22. S. TSENG ZHANG, K. VILATHGAMUWA, D. NGUYEN: Design of a Robust Grid Interface System for PMSG-based Wind Turbine Generators. IEEE Transactions on Industrial Electronics, **58** (1), 316 (2010).

Received 7 May 2019
Revised 29 May 2019

INSTRUCTION FOR AUTHORS

The Editorial Board announces that from 01.07.2016 introduces an obligatory fee of 150 Euros per one research article in the International Journal *Oxidation Communications* for authors, whose Institutions, to which they belong, have no subscription to the Journal for the corresponding year. The introduction of this payment is imposed by the financial difficulties of the Editorial Board enforced by the financial crisis. The authors can publish their manuscripts as rapid publication 9 months after the receipt of positive referees comments, the revised version and confirmation of the fee payment of 250 Euros. The articles intended to be published as rapid publication should follow the requirements for contribution length as pointed below. Authors from Universities and Organisations, which have a subscription or sponsorship to the Journal publish their papers free of charge. The authors receive a hard copy of the Journal issue containing their published article free of charge. Some figures, according to authors decision, can be published coloured in order to make them more understandable to the reader. The additional payment is 75 Euro per printed page.

The authors are kindly requested to send a declaration on copyright transfer simultaneously with the manuscript submission to the Editorial Board of *Oxidation Communications*.

All authors must agree to be so listed and must have seen and approved the manuscript, its contents, and its submission to *Oxidation Communications*. Submission of a paper that has not been approved by all authors will not be forwarded for evaluation and publication. Any changes in authorship must be approved in writing by all the original authors.

Manuscripts should present original results not previously published and not considered for publication elsewhere. Authors declare this in the notification letter. Only relevant experimental data that are discussed in the manuscript should be described. Authors are encouraged to present the experimental data in the form of tables. The duplication of experimental data in tables and figures should be avoided.

MANUSCRIPTS TYPE

The language of the manuscripts is exclusively English. The manuscripts must be typed using Times New Roman font size 12, 1.5 space and margins of 2.5 cm on all sides.

Short communications – up to 4 printed pages, including text, all illustrative materials (tables, figures, etc.) and references (not more than one printed page).

Research articles – up to 8–10 printed pages, including main text, tables, figures, schemes and references (not more than two printed pages).

Reviews – up to 15 printed pages, including main text, tables, figures, schemes and references (not more than four printed pages).

The Editorial Board will strictly follow the requirement for contribution length in view of the restricted volume of each book. Depending on the exceeding length are introduced extra page charges (up to 100 Euro).

Receipt of a contribution for consideration will be acknowledged immediately by the Editorial Office. The acknowledgements will indicate the paper reference number assigned to the contribution. Authors are particularly asked to quote this number on all subsequent correspondence.

ORGANISATION

The title page should include the title, authors and their affiliations, complete address of the author to whom correspondence should be sent and an Abstract.

Abstract – should not exceed 200 words and should give the subjects and conclusions of the article and all results of general interest. References, compound numbers and abbreviations should be avoided. A maximum of five keywords should follow the Abstract.

Aims and Background – should include brief and clear remarks outlining the specific purpose of the work and a short summary of the background material including numbered references.

Experimental – should be sufficiently detailed (but concise) to guarantee reproducibility.

Results and Discussion – should indicate the logic used for the interpretation of data without lengthy speculations. Authors submitting material on purely theoretical problems or on a new experimental technique might unite the sections Experimental, Results and Discussion into one section under the heading Discussion. Authors should avoid doubling of results in the form of tables and figures.

Conclusions – short summary of the main achievements of the research.

References – should be typed at the end of the manuscript and numbered in the order as first cited in the text as superscript Arabic numerals. In the list of references the original papers should be given with their titles. Abbreviations of journal titles should follow the style used in ISI Journal Title Abbreviations. Sequence and punctuation of references should be:

1. E. SZABÓ, G. L. ZÜGNER, M. FARKAS, I. SZILÁGYI, S. DÓBÉ: Direct Kinetic Study of the OH-radical Initiated Oxidation of Pivalaldehyde, $(CH_3)_3CC(O)H$, in the Gas Phase. Oxid Commun, **35** (3), 538 (2012).
2. M. B. NEIMAN, D. GAL: The Kinetic Isotope Method. Akademiai Kiado, Budapest, 1971.
3. J. A. HOWARD: In: Advances in Free Radical Chemistry. Vol. 4 (Ed. G. H. Williams). Lagos Press, London, 1972, 49–69.
4. C. HANSCH (Ed.): Comprehensive Drug Design. Pergamon Press, New York, 1990, p. 19.

In preparing the list of References attention must be drawn to the following points:

(a) Only the initials of first and middle names should be given.
(b) In case of more than 5 authors, use of ‘et al.’ is recommended.

Tables – each bearing a brief title and numbered in Arabic numerals. The tables should be placed in the text as first cited.

Figures and captions – should be numbered consecutively with captions and must be placed at their first mentioning in the text.

Particular attention is drawn to the use of SI Units, IUPAC nomenclature for compounds and standard methods of literature citation.

ELECTRONIC SUBMISSION OF MANUSCRIPTS

Manuscripts should be submitted in electronic form. Submission not in electronic form may face a delay in publication. All text (including the title page, abstract, keywords, all sections of the manuscript, figure captions, and references) and tabular material should be in one file. The manuscript must be prepared using MS Word 6.0 and above. Manuscripts in PDF format are not accepted.

Chemical equations must be supplied using equation editor. Tables must be created using table format feature.

Graphics, i.e. figures, schemes, etc. must be placed at their first mentioning in the text. Structures and schemes may be supplied in ChemWindow format and other graphics in Microsoft Excel or Microsoft PowerPoint format.

SUBMISSION OF MANUSCRIPTS

Manuscripts should be sent to the following address:
Prof. Dr. Slavi K. Ivanov
SciBulCom Ltd., P. O. Box 249, 7 Nezabravka Str., 1113 Sofia, Bulgaria
Phone/Fax: +359 2 872 42 65, +359 2 978 72 12
E-mail: scibulcom2@abv.bg

All manuscripts are subject to critical review and the names of referees will not be disclosed to the authors. The manuscript sent back to the author for revision should be returned within 2 months by e-mail. Otherwise it will be considered withdrawn. Revised manuscripts are generally sent back to the original referees for comments, unless (in case of minor revisions) the editors accept them without seeking further opinions. Proofs should be corrected and returned as soon as possible.